QUANTUM TRANSPORT IN NANODEVICES

By

Brandon Girard Cook

Dissertation

Submitted to the Faculty of the

Graduate School of Vanderbilt University

in partial fulfillment of the requirements

for the degree of

DOCTOR OF PHILOSOPHY

in

Physics

December, 2012

Nashville, Tennessee

Approved:

Professor Kalman Varga

Professor Sokrates Pantelides

Professor David Ernst

Professor Kirill Bolotin

Professor Yaqiong Xu

TABLE OF CONTENTS

LIST OF TABLES

LIST OF FIGURES

CHAPTER I

INTRODUCTION

1.1 Nanoscience

Nanoscience is the study of matter on the atomic and molecular scale, where relevant dimensions are on the order of 1-100 nanometers and quantum mechanical effects are important. The invention of the scanning tunneling microscope (STM) in 1981 marked the practical start of the modern field; for which the Nobel prize in Physics was awarded to Binnig and Roher of IBM in 1986. This instrument allowed the manipulation and imaging of matter with atomic precision. Since, the scope of the field has expanded considerably. Nanotechnology has the potential to impact a broad range of fields including medicine, biology, electronics, materials and energy.

The electronic, magnetic, optical and structural properties of materials on the nanoscale are accessible experimentally. Measurements of these properties reveal the quantum nature of nanoscale matter. However, the interpretation of those experiments requires careful analysis and in many cases extensive numerical simulation. For example the standard classical description of electron transport in conductors is described by Ohm's law; current is proportional to the potential difference across a device, $I = V/R$. Conductance in this description is the inverse of resistance, $G = 1/R = \sigma A/l$, where σ is the conductivity, A is the cross sectional area and l is the length of the channel. Experiments have revealed that this picture no longer holds on the nanoscale. Conductance could be quantized as a function of electron

energy, applied magnetic field or other parameter[1–3].

1.2 Role of computation

Simulation is a valuable tool for not only understanding complex phenomena but for predicting new directions for experimental investigation. Due to the complicated quantum mechanical nature of matter at the nanoscale simple model systems fall short of providing the required precision in practical cases. The many-body equations of quantum mechanics are unsolvable analytically except in very few special cases. Numerical solution is then the way to calculate properties of systems without introducing free parameters. Even numerical solution of the Schrödinger equation is a difficult problem, with solutions only possible in small and simple systems. However, approximations to lower the computational cost at the expense of accuracy are possible.

Density functional theory has emerged as a standard tool in describing the electronic structure of materials[4–6]. Instead of working with the full many-body wavefunction, a function of 3N coordinates, the electron density, with only 3 coordinates, is the central quantity. Formally, density functional theory is exact. Density functional methods, depending on the basis set, scale as $O(N \log N)$ or even $O(N)$, where N is the number of electrons. Compared to Hartree-Fock which is $O(N^4)$ to $O(N^3)$, or perturbation theory methods which can be as high as $O(N^7)$ density functional calculations are cheap. Low computational cost combined with recent advances in describing exchange and correlation effects have lead to the widespread adoption. In the standard formulation it is best suited for the description of isolated systems such

as molecules and clusters or fully periodic systems such as solid crystals.

The case of a device, or scattering, region connected to semi-infinite electrodes is not well described in the standard approach. In the past decade the extension of density functional methods to systems with open boundary conditions has been actively developed[7–9]. A common approach used in many works is based on non-equilibrium Green's functions combined with a density functional theory Hamiltonian[7]. Calculations using the established methods, but applied to new systems, help to explain existing experiments and highlight possible new directions. However, computational study of some systems with existing frameworks is not possible without additional development of computational methods. These factors drive to development of methods and formalism needed to calculate the electron transport properties of nanoscale systems.

1.3 Overview

The focus of this thesis is the simulation of electron transport properties in nanoscale devices. Work related to this dissertation has resulted in four peer reviewed journal articles[10–13] and ten proceedings. The outline is as follows:

Chapter II introduces the necessary formalism. Here the foundations of density functional theory, basis sets, quantum scattering theory and complex absorbing potentials are described. The extension of the complex absorbing potential transport framework to the general case of N electrodes is a key development presented in this chapter.

Chapter III discusses computational aspects in detail. The parallelization strategy

for a density functional theory code with an atomic orbital basis set is presented. Also discussed are the implementation of a caching algorithm for memory efficient calculations, solution of self consistent problems and efficient application of finite difference operators. Finally, the convergence of transport properties is discussed with a CO molecule adsorbed onto a mono-atomic gold wire as an example.

Chapter IV presents calculations related to nanowires. Transmission spectra for mono-atomic gold chains, silicon nanowires and graphene nanoribbons with kinks and related defects are shown. It is found that kink defects generally cause large drops in conductance due to quantum interference effects. The conductance properties of elongated gold nanowires are also studied, with geometries produced by accurate molecular dynamics simulations. Polytetrahedral structures formed during elongation are found to cause non-integer values in conductance traces.

Chapter V presents transport calculations for multi-terminal devices. A tight-binding model is solved analytically to show the accuracy of the formalism developed in Chapter II. Simulations of model systems with 8 terminals highlight some of the quantum interference effects present in multi-terminal systems. Finally, more realistic examples of a four terminal graphene cross junction and six terminal carbon nanotube junction are simulated with a density functional theory Hamiltonian.

Chapter VI describes electronic devices which incorporate graphene. Graphene is widely touted as an ideal electrode material, and some groups have considered all-carbon devices by combining graphene and carbon nanotubes. In this chapter the Schottky barrier in a graphene-carbon nanotube junction is calculated and the potential of creating functional devices is discussed. Silicon is an important material

in modern electronics, yet the interaction between graphene and silicon surfaces is not well studied. In this chapter the interaction between graphene nanoribbons and silicon with vacancy defects is examined. Since graphene does not possess a band gap other two-dimensional materials have been proposed to combine with graphene to form devices. Molybdenum disulphide is a two-dimensional material with a band gap. The interaction of graphene and MoS_2 is explored in this chapter.

CHAPTER II

FORMALISM

In this chapter I present elements of density functional theory (DFT) and electron scattering theory. A primary development of this work is the extension of the complex adsorbing potential electron transport framework to the general case of N-terminal devices[10].

The chapter begins with a description of the fundamental theorems and equations of DFT in section 2.1. Exchange and correlation effects are also addressed in this section. Then, the representation of the density functional Hamiltonian with atomic orbital, real-space grid and plane-wave basis sets is outlined in section 2.2. Next, Section 2.3 presents the formalism for quantum transport calculations. In this section the relevant equations of multichannel scattering theory are presented. With the required background established a description of quantum transport calculations in the complex adsorbing potential frameworks is given. In these sections I describe the form of the complex potentials, the calculation of the density matrix and transmission coefficients.

2.1 Density functional Hamiltonian

Density functional theory (DFT) is a formally exact method to solve the quantum many-body problem. Remarkably, ground-state properties can be found without directly working with the many-body wavefunction; instead one works with the

ground-state electron density. This allows computationally efficient implementation — a driving factor in the method's wide adoption. In this section I review the foundations of DFT; covering the Hohenberg-Kohn theorem, the Kohn-Sham equations, pseudopotentials and exchange-correlation functionals. This is not intended to be a comprehensive overview as excellent review articles[4] and books[5,6] are available.

The Hohenberg-Kohn (HK) theorem provides the basis for DFT:[14]

Hohenberg-Kohn theorem. *For N electrons interacting in a static-external potential, $V(\boldsymbol{r})$, the electronic density of the ground-state $n_0(\boldsymbol{r})$ minimizes the functional*

$$E[n(\boldsymbol{r})] = F[n(\boldsymbol{r})] + \int V(\boldsymbol{r})\, n(\boldsymbol{r})\, d\boldsymbol{r}. \tag{2.1}$$

The proof the of theorem is simple and can be found in most solid-state physics textbooks[15].

Kohn and Sham separated the functional, $F[n(\boldsymbol{r})]$ into three parts

$$E[n(\boldsymbol{r})] = T_s[n(\boldsymbol{r})] + \frac{1}{2}\int\int \frac{n(\boldsymbol{r})\, n(\boldsymbol{r'})}{|\boldsymbol{r} - \boldsymbol{r'}|} d\boldsymbol{r} d\boldsymbol{r'} + E_{XC}[n(\boldsymbol{r})]. \tag{2.2}$$

The first term, $T_s[n(\boldsymbol{r})]$, is the kinetic energy of a non-interacting electron gas, the second term is the Hartree (electrostatic) energy and the final term is the exchange and correlation energy. The point of the separation is that the first two terms can be easily dealt with while the final term contains the complicated many-body effects. The exact form of the exchange and correlation term is unknown and approximations must be made to use the theory in practice. Subsection 2.1.1 discusses the exchange-

correlation functional in more detail.

With the constraint that the number of electrons in the system is fixed, enforced via a Lagrange multiplier, and the separation introduced by Kohn and Sham the Schrödinger equation for non-interacting particles can be obtained,

$$\left[-\frac{1}{2}\nabla^2 + V_{KS}\left(\boldsymbol{r}\right)\right]\psi_i\left(\boldsymbol{r}\right) = \epsilon_i\psi_i\left(\boldsymbol{r}\right). \tag{2.3}$$

The previous equation provides a route to practical calculations using density functional theory and is known as the Kohn-Sham equation. Here the electron density is defined as

$$n\left(\boldsymbol{r}\right) = \sum_{i=1}^{N}\left|\psi_i\left(\boldsymbol{r}\right)\right|^2. \tag{2.4}$$

It is important to note that the potential in Equation 2.3 depends on the density and therefore should be solved self-consistently with Equation 2.4. Details of the self-consistent solution procedure are given later in subsection 3.1.

Coulomb potentials pose several computational difficulties. Since wave functions must be orthogonal and many states near atomic cores are highly localized, those states must be rapidly oscillating to maintain orthogonality. For an accurate all-electron picture those oscillations must be captured by the basis used to represent the wave-function. This corresponds to a high planewave cutoff or very fine real-space grid spacings; implying large numbers of planewave coefficients or grid points which must be computed and stored. The pseudopotential method involves replacing the Coulomb potential and core electrons with an effective potential. The basis of the ap-

proximation is the observation that core electrons are typically not chemically active. That is, the energy contribution from core electrons remains constant if the atoms are isolated or part of a molecule or solid. Pseudopotentials can take various forms and extended discussion of the subject can be found in review articles[16]. The generation of useful pseudopotentials is the subject of significant literature[17–20]. While details differ, a common feature is that beyond a certain cutoff radius the pseudopotential and wavefunction match the full all-electron potential and wavefunction. In general, increasing the cutoff radius reduces the cost of the calculation and reduces the accuracy.

2.1.1 Exchange and correlation

A major issue in the practical application of DFT is that the exact form of the exchange and correlation functional is only known for simple cases such as the free electron gas. Vast literature exists on the development of accurate functionals (see Reference[21] and those within), a topic of past and current research. A comprehensive survey of functionals is beyond the scope of this thesis. Here I present the conceptually simple, but surprisingly accurate, local density approximation and end with some comments about more complex functionals.

The local density approximation (LDA) is derived from a homogeneous electron gas model and the functional is defined as

$$E_{XC}^{LDA}[n(\boldsymbol{r})] = \int n(\boldsymbol{r})\, \varepsilon_{XC}(n(\boldsymbol{r}))\, d\boldsymbol{r} \tag{2.5}$$

and the associated potential is

$$V_{XC}^{LDA}(\boldsymbol{r}) = \varepsilon_{XC}(n(\boldsymbol{r})) + n(\boldsymbol{r})\frac{d\varepsilon_{XC}}{dn(\boldsymbol{r})}. \tag{2.6}$$

This functional depends only on the density at each point and is therefore fully local.

The exchange part of the energy density is known analytically and the correlation part is known in the high and low density limits. Values between the limits are known from accurate Quantum Monte Carlo simulations[22]. The results of the accurate simulations are interpolated for use in calculations. A number of parameterizations exist; such as Perdew-Zunger (PZ)[23]. The PZ parameterization is given by

$$\begin{aligned} E_{XC}[n(\boldsymbol{r})] &= \int \varepsilon_{XC}[n(\boldsymbol{r})]n(\boldsymbol{r})\,d\boldsymbol{r} \\ &\approx \int \left[\varepsilon_X(n(\boldsymbol{r})) + \varepsilon_C(n(\boldsymbol{r}))\right] n(\boldsymbol{r})\,d\boldsymbol{r} \end{aligned} \tag{2.7}$$

where

$$\varepsilon_X(n(\boldsymbol{r})) = -\left(\frac{81}{64\pi}\right)^{1/3} n(\boldsymbol{r})^{1/3} \tag{2.8}$$

and

$$\varepsilon_C(n(\boldsymbol{r})) = \begin{cases} -0.1423(1 + 1.0529\sqrt{r_s} + 0.3334r_s)^{-1} & \text{if } r_s \geq 1, \\ -0.048 + 0.031\ln r_s - 0.0117r_s + 0.002r_s\ln r_s & \text{if } r_s < 1 \end{cases}. \tag{2.9}$$

Here the Wigner-Seitz radius is defined as

$$r_s = \left(\frac{4\pi n(\boldsymbol{r})}{3}\right)^{-1/3}. \tag{2.10}$$

Beyond the local density approximation there are many available functionals which include additional non-local information[24–38]. There is a progression in terms of the trade-off between information included and computational cost, with fully local and and fully non-local representing the opposing ends of the spectrum[21]. Generalized gradient (GGA) functionals include dependencies on the density and the gradient of the density[24–31]. An extended discussion of GGA functionals can be found in Reference[39]. More expensive are those functionals which depend on higher order derivatives of the density known as meta-GGA (mGGA)[32–34]. Modern developments include the addition of some percentage of Hartree-Fock exchange known as hybrid functionals[35,36]. Another area of current research is the inclusion of van der Waals interactions in functionals[37,38] because local and semi-local functionals are unable to correctly describe the asymptotic behavior of dispersion correlations. A review of the performance of many of the most popular functionals can be found in Reference[21].

2.2 Basis function representation of Hamiltonian

In order to solve the Kohn-Sham equations the wavefunctions must be expanded in terms of some basis functions. The most common forms of basis functions are planewaves, real-space grids and local atom centered functions. Less common, but still in use are, wavelets and Lagrange functions. Basis sets differ in accuracy, computational efficiency and what type of geometry is best described by them. For example planewaves are suited for periodic systems and are accurate as they form a complete set with a single parameter controlling the accuracy. This section highlights three common basis sets: numerical atomic orbitals, real-space grids and planewaves.

2.2.1 Atomic orbitals

Atomic orbitals are a common choice for basis set in electronic structure calculations. Their localized nature makes them especially suited to efficient calculations. However, the accuracy is more difficult to control than in the case of planewaves or real-space grids, where the cutoff energy or grid spacing controls the accuracy.

A wavefunction expanding in terms of atomic orbitals is

$$\Phi\left(\boldsymbol{r}\right)=\sum_{i=1}^{N_{atom}}\sum_{k_i=1}^{n_i}\sum_{l_i=0}^{l_i^{max}}\sum_{m_i=-l_i}^{l_i}c_{ik_il_im_i}\phi_{k_il_im_i}\left(\boldsymbol{r}-\boldsymbol{R_i}\right) \tag{2.11}$$

where N_{atom} is the number of atoms in the system, n_i is the number of orbitals for each atom, l_i^{max} is the maximum orbital momentum for a given atom and $\boldsymbol{R}_i$ is the position of atom i. The basis functions are defined by a radial and angular part,

$$\phi_{lm}\left(\boldsymbol{r}\right)=\varphi_l(r)Y_{lm}(\hat{\boldsymbol{r}}), \tag{2.12}$$

where Y_{lm} is a spherical harmonic. Radial functions are either represented with numerical tables or expanded in terms of other basis functions. Numerical tables allow flexibility in the choice of radial function shape and are generally cheap as only a few thousand stored values are needed to achieve acceptable accuracy in interpolation. Generally the interpolation does not depend on the number of stored only values. When these functions are further expanded in terms of basis functions, Gaussian functions are a common choice. Depending on the choice of basis function type integrals, such as the overlap of the ϕ_i, can be written analytically. In the case of

a Gaussian expansion the elements are expressed in terms of associated Laguerre polynomials. The Kohn-Sham equations in the atomic orbital basis representation are written as the general eigenvalue problem

$$HC = ESC, \tag{2.13}$$

where the Hamiltonian matrix elements are

$$H_{ij} = \langle \phi_i(\boldsymbol{r} - \boldsymbol{R_i}) | H | \phi_j(\boldsymbol{r} - \boldsymbol{R_j}) \rangle. \tag{2.14}$$

Here the indices i, j are combined indices of k, l, m. The overlap matrix is defined as

$$S_{ij} = \langle \phi_i(\boldsymbol{r} - \boldsymbol{R_i}) | \phi_j(\boldsymbol{r} - \boldsymbol{R_j}) \rangle \tag{2.15}$$

and the variational coefficients are

$$C^T = (c_1, c_2, \ldots, c_N)\,, \tag{2.16}$$

where $c_j = c_{ik_il_im_i}$ with j as a combined index. The dimension of the basis set is N.

2.2.2 Real-space grids

In the real-space approach the density, wavefunctions and potential are directly represented on a discrete set of points in real-space. With a uniform spacing, h, the

coordinates of each point are

$$\boldsymbol{r}(i,j,k) = (ih, jh, kh) \tag{2.17}$$

where $i = 1, \ldots, N_x$; $j = 1, \ldots, N_y$; and $k = 1, \ldots, N_z$. Then all integrations needed are simply

$$\int_\Omega f(\boldsymbol{r})\, d\boldsymbol{r} \approx h^3 \sum_{ijk} f(\boldsymbol{r}(i,j,k)). \tag{2.18}$$

In this representation the dimension of the Hamiltonian is large — the total number of grid points. However, the local part of the Hamiltonian is diagonal in this representation. The non-local parts of the Hamiltonian, coming from the pseudopotential, exchange-correlation potential, or kinetic energy, are localized in the neighborhood of atoms and are very sparse. The kinetic operator acting on the wavefunction is expanded in terms of a finite-difference

$$\begin{aligned} \nabla^2 \psi(\boldsymbol{r}(i,j,k)) = & \sum_{n=-N_D}^{N_D} C_n \psi(i+n, j, k) \\ & + \sum_{n=-N_D}^{N_D} C_n \psi(i, j+n, k) \\ & + \sum_{n=-N_D}^{N_D} C_n \psi(i, j, k+n) \end{aligned} \tag{2.19}$$

where C_n are finite difference coefficients and N_D is the order of finite difference stencil. Sufficient accuracy is normally reached with a value of $N_D = 4$. The operation of

a local potential on a wavefunction in the real-space approach is just a multiplication,

$$V^{local}\left(\boldsymbol{r}\right)\psi\left(\boldsymbol{r}\right)=V^{local}(i,j,k)\psi(i,j,k) \tag{2.20}$$

The non-local part of the pseudopotential is also sparse because it is zero beyond a set radius from each atom. This restricts the range of points one must integrate over to those within that radius:

$$\begin{aligned}\int_{\Omega}V^{nonlocal}(\boldsymbol{r},\boldsymbol{r'})\psi\left(\boldsymbol{r'}\right)d\boldsymbol{r'}&=\sum_{lm}\frac{\langle v_{lm}^{a}|\langle v_{lm}^{a}|\psi\rangle}{\langle\psi_{lm}^{ps,a}|v_{l}^{a}|\psi_{lm}^{ps,a}\rangle}\\&=\sum_{i'j'k'}V_{ijk,i'j'k'}^{NL}\psi(i'j'k'),\end{aligned} \tag{2.21}$$

where the prime indices only run over grid points that are within the non-local pseudopotential radius of the atoms. Finally, the action of the Hamiltonian on the wavefunction can be written

$$\begin{aligned}H_{KS}\psi(\boldsymbol{r}(i,j,k))=&\sum_{n=-N_D}^{N_D}C_n\left[\psi(i+n,j,k)+\psi(i,j+n,k)+\psi(i,j,k+n)\right]\\&+V^{\text{local}}(i,j,k)\psi(i,j,k)+\sum_{i'j'k'}V_{ijk,i'j'k'}^{NL}\psi(i'j'k').\end{aligned} \tag{2.22}$$

Direct diagonalization of the Hamiltonian is impractical due to the large dimension, but since the action of the Hamiltonian on the wavefunctions is known, a conjugate gradient scheme (or other iterative method) can be used to obtain the wavefunctions.

2.2.3 Planewaves

Planewaves are one of the most commonly used basis sets in solid state physics due to their suitability in the description of periodic systems, such as bulk crystals, and the simplicity of implementation. In a periodic system the potential obeys

$$v(R) = V(\boldsymbol{r} + \boldsymbol{R}), \tag{2.23}$$

where $\boldsymbol{R} = n_1\boldsymbol{a}_1 + n_2\boldsymbol{a}_2 + n_3\boldsymbol{a}_3$. Here, n_i are integers and $\boldsymbol{a}_i$ are lattice vectors of the crystal. With the Bloch theorem the wavefunction of a periodic system can be written as a product of periodic function and a planewave

$$\Psi_{i,\boldsymbol{k}}(\boldsymbol{r}) = e^{i\boldsymbol{k}\cdot\boldsymbol{r}} u_{i,\boldsymbol{k}}(\boldsymbol{r}) \tag{2.24}$$

where $u_{i,\boldsymbol{k}}(\boldsymbol{r})$ is a periodic function and $\boldsymbol{k}$ is the crystal momentum. Expanding $u_{i,\boldsymbol{k}}(\boldsymbol{r})$ in terms of planewaves

$$u_{i,\boldsymbol{k}}(\boldsymbol{r}) = \sum_{\boldsymbol{G}} c_{i,\boldsymbol{G}+\boldsymbol{k}} e^{i\boldsymbol{r}\cdot\boldsymbol{G}} \tag{2.25}$$

The accuracy of the expansion can be expressed by a cutoff energy

$$E_{cut} = |\boldsymbol{G} + \boldsymbol{k}|^2 . \tag{2.26}$$

Only planewaves with $E < E_{cut}$ will be used in the calculations. The density associated with a single eigenfunction is

$$\begin{aligned} n_{i\boldsymbol{k}}(\boldsymbol{r}) &= \left| u_{i,\boldsymbol{k}}(\boldsymbol{r}) \right|^2 \\ &= \sum_{\boldsymbol{G}\boldsymbol{G}'} c^*_{i,}\boldsymbol{G}+\boldsymbol{k} c_{i,}\boldsymbol{G}'+\boldsymbol{k} e^{i\boldsymbol{r}\cdot(}\boldsymbol{G}-\boldsymbol{G}'). \end{aligned} \tag{2.27}$$

The total density can be constructed by integrating over the first Brillouin zone:

$$n(\boldsymbol{r}) = \frac{1}{\Omega}\sum_i \int_{BZ} d\boldsymbol{k} f_{i\boldsymbol{k}} n_{i\boldsymbol{k}}(\boldsymbol{r}), \tag{2.28}$$

where $f_{i\boldsymbol{k}}$ is an occupation number. In calculations a finite mesh is used and the integral is replaced by a sum. Reasonable accuracy is obtained with this replacement due to the smooth nature of the wavefunction in reciprocal space. The kinetic energy is diagonal in the planewave representation

$$\langle \boldsymbol{G}+\boldsymbol{k}|T|\boldsymbol{G}'+\boldsymbol{k}\rangle = |\boldsymbol{G}+\boldsymbol{k}|^2 \delta_{\boldsymbol{G}\boldsymbol{G}'}, \tag{2.29}$$

where $|\boldsymbol{G}+\boldsymbol{k}\rangle = e^{i}\boldsymbol{G}+\boldsymbol{k}\cdot\boldsymbol{r}$. The local potential elements are

$$\langle \boldsymbol{G}+\boldsymbol{k}|V|\boldsymbol{G}'+\boldsymbol{k}\rangle = V(\boldsymbol{G}-\boldsymbol{G}') \tag{2.30}$$

and the non-local potential elements are

$$\langle \boldsymbol{G}+\boldsymbol{k}|W|\boldsymbol{G}'+\boldsymbol{k}\rangle = W(\boldsymbol{G}+\boldsymbol{k},\boldsymbol{G}'+\boldsymbol{k}). \tag{2.31}$$

The Hamiltonian is then

$$\sum_{\boldsymbol{G'}} H_{\boldsymbol{G},\boldsymbol{G'}} c_{\boldsymbol{G'}} + \boldsymbol{k} = E_{n,\boldsymbol{k}} c_{\boldsymbol{G}} + \boldsymbol{k}, \tag{2.32}$$

where

$$\begin{aligned} H_{\boldsymbol{G},\boldsymbol{G'}} &= \langle G|H|G'\rangle \\ &= \langle G|T+V+W|G'\rangle \\ &= |\boldsymbol{G}+\boldsymbol{k}|^2 + V(\boldsymbol{G}-\boldsymbol{G'}) + W(\boldsymbol{G}+\boldsymbol{k},\boldsymbol{G'}+\boldsymbol{k}). \end{aligned} \tag{2.33}$$

Some additional steps are required before practical calculations with pseudopotentials can be carried out. The details depend on the approach, but essentially the long range divergence in the $\boldsymbol{G}=0$ term for Coulomb potentials is canceled by adding Gaussian compensation charges.

2.3 Quantum transport calculations

Calculation of transport properties of nanoscale devices with a density functional based framework has become commonplace since the early 2000s when the first works appeared. Early efforts calculated the properties of devices with two electrodes contacted to a scattering region with a combination of non-equilibrium Green's functions and a density functional theory Hamiltonian (NEGF+DFT)[7,40] or by using the Lippmann-Schwinger equation directly[41,42]. Since then frameworks based on other methods have appeared[43], but the NEGF+DFT framework has remained the standard. Several excellent books are available which cover the established quantum

transport formalisms[44–47]. One such alternative method is based on complex potentials[48,49]. In this section I describe the extension of the complex absorbing potential (CAP) framework to the general case of devices with N electrodes. Compared to the NEGF+DFT framework, the multi-terminal CAP method is easier to implement and computationally advantageous[10]. The difficulty of working in the NEGF+DFT framework with more than 2 electrodes is evident with only few works appearing with just 3 or 4 terminals. The section is outlined as follows:

Subsection 2.3.1 describes the structure of a multi-terminal Hamiltonian with a localized basis set. Subsection 2.3.2 presents basic necessary elements of multi-channel scattering theory. Subsection 2.3.3 shows the calculation of transmission coefficients and subsection 2.3.4 shows details of complex absorbing potential calculations.

2.3.1 Structure of Hamiltonian

The structure of a multi-terminal device is shown in Figure 2.1. In this work localized basis functions are used to represent the Hamiltonian of the system. Various localized basis function sets have been tested in transport calculations, including localized atomic orbitals[7,50–59] and box basis functions[60]. The Hamiltonian and overlap matrices are sparse because localized basis functions only overlap with each other in a given region. For transport calculations the system is divided into lead and scattering regions. Basis functions associated with each lead are restricted from interacting with other leads. That is, there is no overlap between the sets of basis functions of different leads. However, there is an overlap between lead and scattering region basis functions.

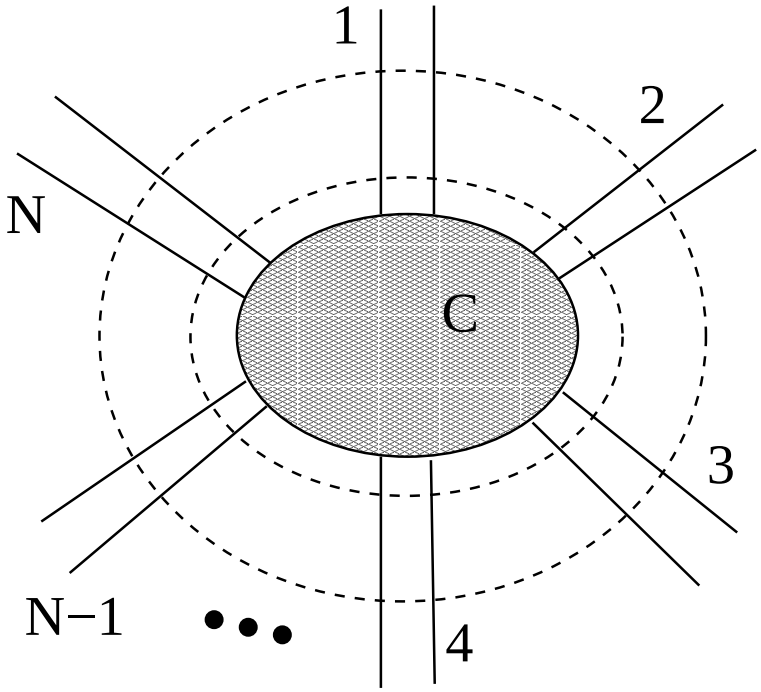

Figure 2.1: N-terminal junction. The CAP is added between the two dashed lines and the shaded area represents the central scattering region.

The leads consist of periodically repeated cells. The size of the cells is chosen such that the basis functions only connect the neighboring cells and the Hamiltonian matrix of lead a has a block-tridiagonal structure:

$$H_a = \begin{pmatrix} h_a^{00} & h_a^{10+} & 0 & 0 \\ h_a^{10} & h_a^{00} & h_a^{10+} & 0 \\ 0 & h_a^{10} & h_a^{00} & \dots \\ 0 & 0 & \dots & \dots \end{pmatrix}. \tag{2.34}$$

The overlap matrix of lead a is

$$S_a = \begin{pmatrix} s_a^{00} & s_a^{10+} & 0 & 0 \\ s_a^{10} & s_a^{00} & s_a^{10+} & 0 \\ 0 & s_a^{10} & s_a^{00} & \dots \\ 0 & 0 & \dots & \dots \end{pmatrix}. \tag{2.35}$$

Denoting the Hamiltonian matrices coupling lead a and the central region by τ_a and the Hamiltonian of the central region by H_C, the Hamiltonian of the N terminal system takes the form

$$\boldsymbol{H} = \begin{pmatrix} H_1 & 0 & \dots & 0 & 0 & \tau_1^+ \\ 0 & H_2 & \dots & 0 & 0 & \tau_2^+ \\ \vdots & \vdots & \ddots & \vdots & \vdots & \vdots \\ 0 & 0 & \dots & H_{N-1} & 0 & \tau_{N-1}^+ \\ 0 & 0 & \dots & 0 & H_N & \tau_N^+ \\ \tau_1 & \tau_2 & \dots & \tau_{N-1} & \tau_N & H_C \end{pmatrix}. \tag{2.36}$$

In the following sections (2.3.3 and 2.3.4) bold fonts indicate that the quantity has dimensions of the full system.

2.3.2 Elements of scattering theory

In this subsection some elements of formal multichannel scattering theory are reviewed. For more details refer to Reference[61]. These equations will be used in the

following description of transport properties in multi-terminal devices given (especially Subsection 2.3.3).

The Lippmann-Schwinger equation is used to arrive at the transition probability of an incoming state in lead b to an outgoing state in lead a. A wavefunction in channel a is an eigenfunction of the channel Hamiltonian

$$H_a\phi_a = E_a\phi_a \tag{2.37}$$

These channel wavefunctions form a complete orthonormal set of states

$$\sum_\alpha |\phi_{a\alpha}\rangle\langle\phi_{a\alpha}| = 1. \tag{2.38}$$

The Green's function for channel a is given by

$$G_a(E_a + i\epsilon) = \frac{1}{E_a + i\epsilon - H_a}. \tag{2.39}$$

The scattering wavefunction $\psi_a^\pm$ corresponding to the incoming or outgoing wave function from a satisfies

$$H\psi_a^\pm = E_a\psi_a^\pm. \tag{2.40}$$

Combining these two equations produces the Lippmann-Schwinger equation for ψ_a^+

$$\psi_a^+ = (1 + G(E_a + i\epsilon)V_a)\,\phi_a \tag{2.41}$$

where + stands for an incoming wave boundary condition and

$$V_a = H - H_a. \tag{2.42}$$

Similarly, an outgoing solution in channel b is given by

$$\psi_b^- = (1 + G(E_b - i\epsilon)V_b)\phi_b. \tag{2.43}$$

The transition matrix between a and b is defined by

$$\mathcal{T}_{ba}^+ \phi_a = V_b \psi_a^+ = \left(V_b + V_b G(E_a + i\epsilon)V_a\right)\phi_a. \tag{2.44}$$

The transition probability from an incoming state in b to an outgoing state in a is given by

$$S_{ab}^2 = |\langle \boldsymbol{\psi}_b^- | \boldsymbol{\psi}_a^+ \rangle|^2. \tag{2.45}$$

Interchanging ψ_a^+ and ψ_b^-, the matrix element S_{ab} is calculated from

$$S_{ab} = \delta_{ab} - 2\pi i \delta(E_a - E_b)\langle \phi_b | \mathcal{T}_{ab} | \phi_a \rangle. \tag{2.46}$$

2.3.3 Transmission coefficient in multi-terminal systems

In this subsection the transmission coefficient between lead a and lead b of a multi-terminal system is calculated. A general expression is derived and a useful simplification for use in calculations is shown. The structure of the Hamiltonian is

outlined in subsection 2.3.1. As mentioned previously, bold fonts indicate that the quantity has dimensions of the full system.

The wavefunction of the system corresponding to the partition shown in Fig. 2.1 is

$$\mathbf{\Psi} = \begin{pmatrix} \psi_1 \\ \psi_2 \\ \vdots \\ \psi_{N-1} \\ \psi_N \\ \psi_C \end{pmatrix}. \tag{2.47}$$

The wavefunction of the isolated lead a ($a = 1, \ldots N$) is

$$\mathbf{\Phi}_a = \begin{pmatrix} 0 \\ \vdots \\ 0 \\ \phi_a \\ 0 \\ \vdots \\ 0 \end{pmatrix} \tag{2.48}$$

where ϕ_a is the eigenfunction of the Hamiltonian of lead a

$$H_a \phi_a = E_a \phi_a. \tag{2.49}$$

The wavefunction with incoming asymptotic form in lead a is

$$\boldsymbol{\Psi}_a^+ = (\mathbf{1} + \boldsymbol{G}(E_a + i\epsilon)\boldsymbol{V}_a)\,\boldsymbol{\Phi}_a, \tag{2.50}$$

where

$$\boldsymbol{G}(E + i\epsilon) = \frac{1}{E + i\epsilon - \boldsymbol{H}}, \tag{2.51}$$

and

$$\boldsymbol{V}_a = \begin{pmatrix} 0 & \dots & 0 & 0 & 0 & \dots & 0 & 0 \\ \vdots & \ddots & \vdots & \vdots & \vdots & \ddots & \vdots & \vdots \\ 0 & \dots & 0 & 0 & 0 & \dots & 0 & 0 \\ 0 & \dots & 0 & \tau_a & 0 & \dots & 0 & 0 \end{pmatrix}. \tag{2.52}$$

Similarly, the wavefunction with outgoing asymptotic form in lead b is given by

$$\boldsymbol{\Psi}_b^- = (\mathbf{1} + \boldsymbol{G}(E_b - i\epsilon)\boldsymbol{V}_b)\,\boldsymbol{\Phi}_b. \tag{2.53}$$

The transmission probability from lead b to lead a can be calculated from Eq. (2.45)

$$|\langle \boldsymbol{\Psi}_b^- | \boldsymbol{\Psi}_a^+ \rangle|^2 \tag{2.54}$$

which can be rewritten as (see subsection 2.3.2)

$$|\langle \boldsymbol{\Phi}_b | \boldsymbol{V}_b \left(1 + \boldsymbol{G}(E)\boldsymbol{V}_a\right) | \boldsymbol{\Phi}_a \rangle|^2 = |\langle \boldsymbol{\Phi}_b | \boldsymbol{V}_b \boldsymbol{G}(E) \boldsymbol{V}_a | \boldsymbol{\Phi}_a \rangle|^2 \tag{2.55}$$

where in writing the second equality the fact that V_b does not connect leads a and b,

$$\langle \mathbf{\Phi}_b | \boldsymbol{V}_b | \mathbf{\Phi}_a \rangle = 0, \tag{2.56}$$

is used. To calculate the transmission from lead b to lead a all lead wave functions must be summed over. The Γ matrix associated with a lead a is

$$\mathbf{\Gamma}_a = \boldsymbol{V}_a^+ \left(\sum_\alpha |\mathbf{\Phi}_a^\alpha\rangle\langle\mathbf{\Phi}_a^\alpha| \right) \boldsymbol{V}_a, \tag{2.57}$$

and $|\boldsymbol{k}\rangle$ stands for a complete set of states formed by superposing all lead bases. With these definitions the transmission can be written

$$\begin{aligned}
T_{ab}(E) &= \sum_{\alpha\beta} |\langle \mathbf{\Phi}_b^\beta | \boldsymbol{V}_b \boldsymbol{G}(E) \boldsymbol{V}_a | \mathbf{\Phi}_a^\alpha \rangle|^2 \\
&= \sum_{\alpha\beta} \langle \mathbf{\Phi}_b^\beta | \boldsymbol{V}_b \boldsymbol{G}(E) \boldsymbol{V}_a | \mathbf{\Phi}_a^\alpha \rangle \langle \mathbf{\Phi}_a^\alpha | \boldsymbol{V}_a^+ \boldsymbol{G}(E)^+ \boldsymbol{V}_b | \mathbf{\Phi}_b^\beta \rangle \\
&= \sum_{\beta} \langle \mathbf{\Phi}_b^\beta | \boldsymbol{V}_b \boldsymbol{G}(E) \mathbf{\Gamma}_a \boldsymbol{G}(E)^+ \boldsymbol{V}_b^+ | \mathbf{\Phi}_b^\beta \rangle \\
&= \sum_{\beta} \sum_{k} \langle \mathbf{\Phi}_b^\beta | \boldsymbol{V}_b | \boldsymbol{k} \rangle \langle \boldsymbol{k} | \boldsymbol{G}(E) \mathbf{\Gamma}_a \boldsymbol{G}(E)^+ \boldsymbol{V}_b^+ | \mathbf{\Phi}_b^\beta \rangle \\
&= \sum_{k} \langle \boldsymbol{k} | \boldsymbol{G}(E) \mathbf{\Gamma}_a \boldsymbol{G}^+(E) \mathbf{\Gamma}_b | \boldsymbol{k} \rangle \\
&= \mathrm{Tr}\left[\boldsymbol{G}(E) \mathbf{\Gamma}_a \boldsymbol{G}(E)^+ \mathbf{\Gamma}_b \right].
\end{aligned} \tag{2.58}$$

In Eq. (2.58) the transmission coefficient is expressed by the Green's function of the whole system and by the $\mathbf{\Gamma}$ matrices. While the Hamiltonian of the system is a sparse block structured matrix, the Green's function matrix is not sparse. The sparse structure of the $\mathbf{\Gamma}$ matrix, however, allows for the simplification of the transmission

coefficient.

To calculate the Green's function matrix $\boldsymbol{G}$ one has to invert

$$E\boldsymbol{S}-\boldsymbol{H} = \begin{pmatrix} ES_1 - H_1 & 0 & \dots & 0 & 0 & \tau_1^+ \\ 0 & ES_2 - H_2 & \dots & 0 & 0 & \tau_2^+ \\ \vdots & \vdots & \ddots & \vdots & \vdots & \vdots \\ 0 & 0 & \dots & ES_{N-1} - H_{N-1} & 0 & \tau_{N-1}^+ \\ 0 & 0 & \dots & 0 & ES_N - H_N & \tau_N^+ \\ \tau_1 & \tau_2 & \dots & \tau_{N-1} & \tau_N & ES_C - H_C \end{pmatrix}. \tag{2.59}$$

By defining

$$\tau = \begin{pmatrix} \tau_1 & \tau_2 & \dots & \tau_{N-1} & \tau_N \end{pmatrix}, \tag{2.60}$$

and the block diagonal matrix

$$ES_L-H_L = \begin{pmatrix} ES_1 - H_1 & 0 & \dots & 0 & 0 \\ 0 & ES_2 - H_2 & \dots & 0 & 0 \\ \vdots & \vdots & \ddots & \vdots & \vdots \\ 0 & 0 & \dots & ES_{N-1} - H_{N-1} & 0 \\ 0 & 0 & \dots & 0 & ES_N - H_N \end{pmatrix}, \tag{2.61}$$

$E\boldsymbol{S} - \boldsymbol{H}$ can be rewritten in the following block form

$$E\boldsymbol{S} - \boldsymbol{H} = \begin{pmatrix} ES_L - H_L & \tau^+ \\ \tau & ES_C - H_C \end{pmatrix}. \tag{2.62}$$

The inverse of this matrix can be calculated by partitioning[62]

$$\begin{aligned}\boldsymbol{G}(E) &= (E\boldsymbol{S} - \boldsymbol{H})^{-1} \\ &= \begin{pmatrix} G_L(E) - G_L(E)\tau^+ G_C(E)\tau G_L(E) & -G_L(E)\tau^+ G_C(E) \\ -G_C(E)\tau G_L(E) & G_C(E) \end{pmatrix}.\end{aligned} \tag{2.63}$$

In the above equation the Green's function of the center is

$$G_C(E) = (ES_C - H_C - \tau G_L(E)\tau^+)^{-1}, \tag{2.64}$$

and the Green's function of the leads is

$$G_L(E) = (ES_L - H_L)^{-1} = \begin{pmatrix} g_1 & 0 & \dots & 0 & 0 \\ 0 & g_2 & \dots & 0 & 0 \\ \vdots & \vdots & \ddots & \vdots & \vdots \\ 0 & 0 & \dots & g_{N-1} & 0 \\ 0 & 0 & \dots & 0 & g_N \end{pmatrix}, \tag{2.65}$$

where the $g_i(E)$ matrices are the Green's functions of the individual lead units,

$$g_i(E) = (ES_i - H_i)^{-1}. \tag{2.66}$$

Using the Green's functions of the leads, the G_C matrix can also be simplified to

$$G_C(E) = (ES_C - H_C - \sum_{i=1}^{N} \Sigma_i(E))^{-1}, \tag{2.67}$$

where

$$\Sigma_i(E) = \tau_i g_i(E) \tau_i^+. \tag{2.68}$$

With these results the expression of the transmission coefficient in Eq. (2.58)

$$T_{ab}(E) = \sum_{\alpha\beta} |\langle \mathbf{\Phi}_b^\beta | \boldsymbol{V}_b \boldsymbol{G}(E) \boldsymbol{V}_a | \mathbf{\Phi}_a^\alpha \rangle|^2 \tag{2.69}$$

can be rewritten by using the equation

$$\langle \mathbf{\Phi}_b^\beta | \boldsymbol{V}_b \boldsymbol{G}(E) \boldsymbol{V}_a | \mathbf{\Phi}_a^\alpha \rangle = \langle \phi_b^\beta | \tau_b^+ G_C(E) \tau_a | \phi_a^\alpha \rangle \tag{2.70}$$

which can be easily derived using Eqs. (2.63), (2.48) and (2.52). Repeating the derivation in (2.58) with (2.70) results in a simplified expression for the transmission coefficient

$$\begin{aligned}
T_{ab}(E) &= \sum_{\alpha\beta} |\langle \phi_b^\beta | \tau_b^+ G_C(E) \tau_a | \phi_a^\alpha \rangle|^2 \\
&= \sum_{\alpha\beta} \langle \phi_b^\beta | \tau_b G_C(E) \tau_a | \phi_a^\alpha \rangle \langle \phi_a^\alpha | \tau_a^+ G_C(E)^+ \tau_b | \phi_b^\beta \rangle \\
&= \sum_{\beta} \langle \phi_b^\beta | \tau_b G_C(E) \Gamma_a G_C(E)^+ \tau_b^+ | \phi_b^\beta \rangle \\
&= \sum_{\beta} \sum_{\beta'} \langle \phi_b^\beta | \tau_b | \beta' \rangle \langle \beta' | G_C(E) \Gamma_a G_C(E)^+ \tau_b^+ | \phi_b^\beta \rangle \\
&= \sum_{\beta'} \langle \beta' | G_C(E) \Gamma_a G_C(E)^+ \Gamma_b | \beta' \rangle \\
&= \mathrm{Tr} \left[G_C(E) \Gamma_a G_C(E)^+ \Gamma_b \right].
\end{aligned} \tag{2.71}$$

Here

$$\begin{aligned}\Gamma_a &= \tau_a^+ \left(\sum_\alpha |\phi_a^\alpha\rangle\langle\phi_a^\alpha| \right) \tau_a \\ &= \tau_a^+ \left(g_a(E) - g_a(E)^+ \right) \tau_a \\ &= i \left(\Sigma_a(E) - \Sigma_a(E)^+ \right),\end{aligned} \tag{2.72}$$

and G_C is the Green's function of the central region and Γ_a and Γ_b are the imaginary parts of the self-energies of leads a and b. This expression is the transmission coefficient used in two-terminal transport calculations[44,45]. In the present work a CAP is added to the Hamiltonian of the leads and both Eqs. (2.58) and (2.71) will be used in the calculations. The next section describes how the addition is done and how transport calculations are carried out in the CAP formalism.

2.3.4 Complex absorbing potentials

Absorbing boundary conditions using complex absorbing potentials (CAPs) were first introduced in time-dependent quantum mechanical calculations to avoid artificial reflections caused by the use of finite basis sets or grids[63]. These CAPs are located in the asymptotic region and annihilate the outgoing waves preventing the undesired reflections. CAPs are extensively used in quantum mechanical calculations of chemical reaction rates and in time-dependent wave packet calculations[64–70]. Complex potentials have also been used in transport calculations of devices with two terminals[71,72].

The complex potentials not only absorb the outgoing waves but can also produce

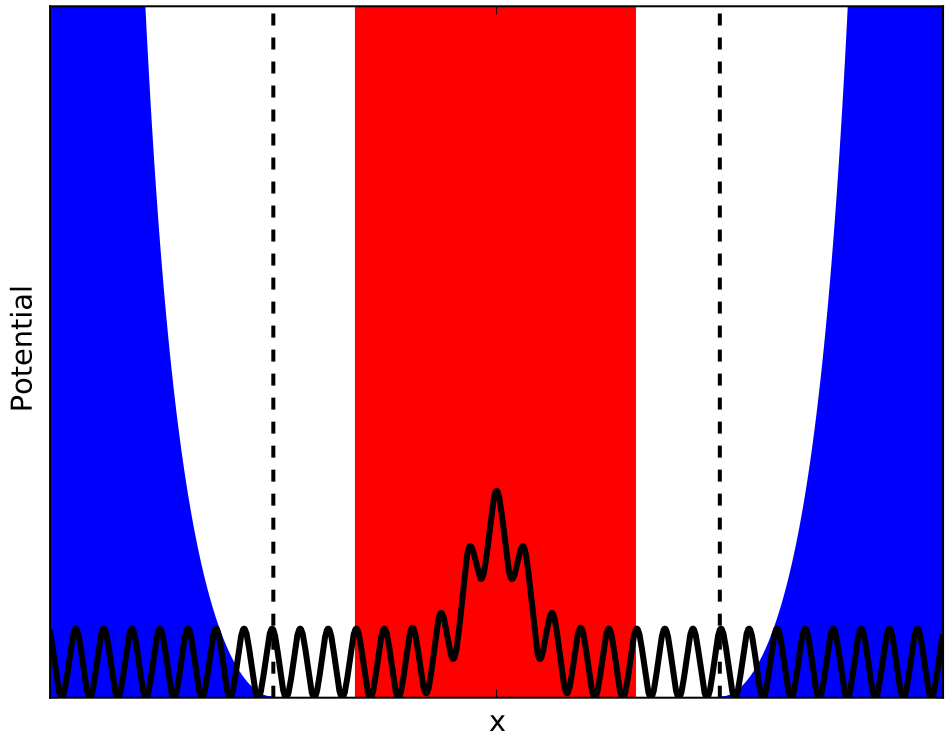

Figure 2.2: Schematic of a complex absorbing potential in one dimension. The scattering region is highlighted in red and the complex potential is highlighted in blue. The solid black curve is the real potential and the dashed black lines indicate the start the complex absorbing potential.

reflections. Therefore the construction and optimization of reflection-free CAPs is pursued by many research groups. Many different forms of pure imaginary potential have been investigated, including linear, power-law[65,67], polynomial[68] and other parameterized functional forms (a recent review is provided by Muga et al.[66]). Besides purely imaginary potentials, complex potentials have also been investigated[69]. In this work the CAP suggested by Manolopoulos[70] is used. This negative, imaginary CAP

is derived from a physically motivated differential equation and its form is

$$-iw(x) = -i\frac{\hbar^2}{2m}\left(\frac{2\pi}{\Delta x}\right)^2 f(y), \tag{2.73}$$

where x_1 is the start and x_2 is the end of the absorbing region (see Fig. 1), $\Delta x = x_2 - x_1$, c is a numerical constant, m is the electron's mass and

$$f(y) = \frac{4}{(c+y)^2} - \frac{4}{(c-y)^2} - 2, \quad y = \frac{c(x-x_1)}{\Delta x}. \tag{2.74}$$

This CAP goes to infinity at the end of the absorbing region and is therefore exactly transmission free. In the numerical implementation the range is extended by a small amount, typically 0.01 Å, beyond the boundary in order to prevent numerical instabilities associated with infinite numbers. The CAP contains only one parameter, the width of the absorbing region Δx. Its reflection properties are guaranteed to improve as this parameter is increased. A schematic of the CAP in one dimension is shown in Figure 2.2.

By adding the CAP (as defined in Eqs. (2.73)-(2.74)) to the Hamiltonian of lead j one obtains

$$H'_j = H_j + iW_j \tag{2.75}$$

where W_j contains the matrix elements of the complex potential on the left and the right. Note that in this section bold fonts indicate quantities which have dimensions of the full system. Assuming that the basis states only connect the neighboring cells in the lead, these matrices will have the same block tridiagonal structure as the leads'

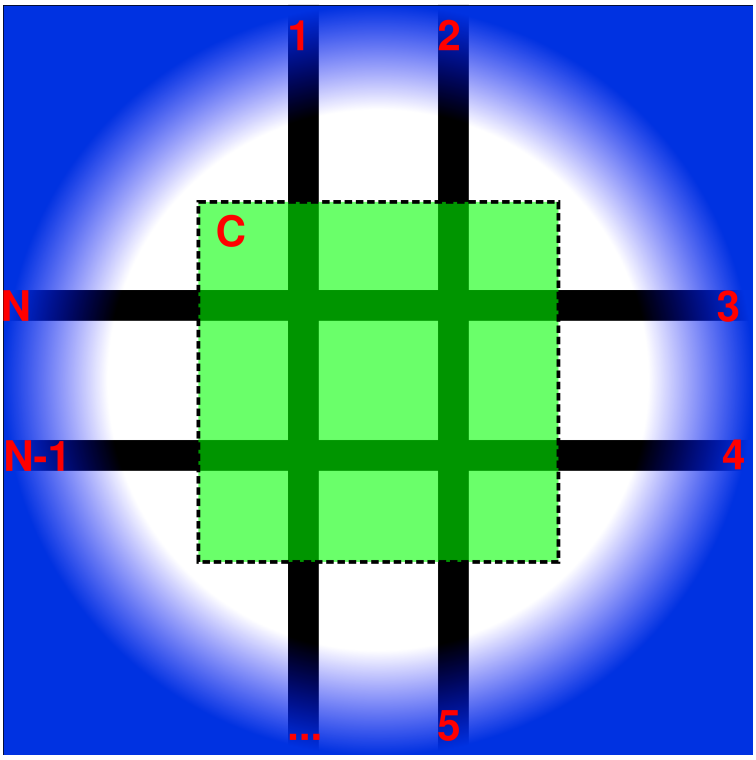

Figure 2.3: Complex absorbing potential in a crossbar device. The scattering region is highlighted in green and the CAP is in blue.

Hamiltonian but for the non-periodic CAP the matrices in the diagonals will not be identical:

$$W_j = \begin{pmatrix} w_j^{00} & w_j^{10+} & 0 & 0 \\ w_j^{10} & w_j^{11} & w_j^{21+} & 0 \\ 0 & w_j^{21} & w_j^{22} & \dots \\ 0 & 0 & \dots & \dots \end{pmatrix} \tag{2.76}$$

The addition of a CAP makes the Hamiltonian a finite dimensional matrix; beyond the range of the complex potential, the lead is effectively cut off. In the calculations the complex potential starts at least one lead cell away from the central region (see

Figures 2.1 and 2.3). With this choice, assuming that the basis functions in the leads only connect neighboring supercells, the τ_i coupling matrices will not have contributions from the complex potential. The Hamiltonian of the system is now

$$\boldsymbol{H}' = \begin{pmatrix} H_1 + iW_1 & 0 & \dots & 0 & 0 & \tau_1^+ \\ 0 & H_2 + iW_2 & \dots & 0 & 0 & \tau_2^+ \\ \vdots & \vdots & \ddots & \vdots & \vdots & \vdots \\ 0 & 0 & \dots & H_{N-1} + iW_{N-1} & 0 & \tau_{N-1}^+ \\ 0 & 0 & \dots & 0 & H_N + iW_N & \tau_N^+ \\ \tau_1 & \tau_2 & \dots & \tau_{N-1} & \tau_N & H_C \end{pmatrix}. \quad (2.77)$$

The addition of a CAP only modifies the wavefunctions and the Green's functions in the region where the CAP is nonzero[48]. In the central region the electron density and the transmission probability are the same as one would obtain using semi-infinite leads without the CAP. The accuracy of the CAP approach in two-terminal transport calculations has been demonstrated[48]. The transport coefficients calculated by the CAP approach are in excellent agreement with the results of conventional calculations using decimation or iteration[73,74] to calculate the Green's function of the leads.

In the CAP formalism, the transmission probability is calculated by using Eq. (2.58) or (2.71). In the first approach, Eq. (2.58) is rewritten. After the CAP is added to the Hamiltonian, the transmission coefficient is calculated using Eq. (2.58)

$$T_{ab}(E) = \mathrm{Tr}\left[\boldsymbol{G}'(E)\boldsymbol{\Gamma}'_a\boldsymbol{G}'(E)^+\boldsymbol{\Gamma}'_b\right]. \quad (2.78)$$

In this equation the prime indicates that the CAP is added. The Green's function with the CAP is defined by

$$\boldsymbol{G}'(E) = (E\boldsymbol{S} - \boldsymbol{H}')^{-1}, \tag{2.79}$$

where H' is defined in Eq. (2.77). In a manner corresponding to the partitioning of the Hamiltonian, the Green's function matrix is partitioned as

$$\boldsymbol{G}' = (E\boldsymbol{S} - \boldsymbol{H}')^{-1} = \begin{pmatrix} G'_{11} & G'_{12} & \dots & G'_{1N} & G'_{1C} \\ G'_{21} & G'_{22} & \dots & G'_{2N} & G'_{2C} \\ \vdots & \vdots & \ddots & \vdots & \vdots \\ G'_{N1} & G'_{N2} & \dots & G'_{NN} & G'_{NC} \\ G'_{C1} & G'_{C2} & \dots & G'_{CN} & G'_{C} \end{pmatrix}. \tag{2.80}$$

Using the results from the previous section, (2.71) and (2.73), the transmission is rewritten as

$$T_{ab}(E) = \mathrm{Tr}\left[G'_C(E)\Gamma'_a G'_C(E)^{+}\Gamma'_b\right] \tag{2.81}$$

$$= \mathrm{Tr}\left[G'_C(E)\tau_a^{+}(g'_a - g_a'^{+})\tau_a G'_C(E)\tau_b^{+}(g'_b - g_b'^{+})\tau_b\right]. \tag{2.82}$$

Using the identity

$$i\left(g'_a - g_a'^{+}\right) = ig'_a\left(\left(g_a'^{+}\right)^{-1} - g_a'^{-1}\right)g_a'^{+} = 2g'_a W_a g_a'^{+} \tag{2.83}$$

the transmission is

$$T_{ab}(E) = 4\mathrm{Tr}\left[G'_C(E)\tau_a g'_a W_a g'^{+}_a \tau_a G'_C(E)\tau_b g'_b W_b g'_b \tau_b\right]. \tag{2.84}$$

In this equation

$$G'_{ab} = g'_a \tau_a^{+} G'_C \tau_b g'_b. \tag{2.85}$$

Using this the transmission becomes

$$\begin{aligned} T_{ab}(E) &= 4\mathrm{Tr}\left[G'_{ab} W_a {G'_{ab}}^{+} W_b\right] \\ &= 4\mathrm{Tr}\left[\boldsymbol{G'}\boldsymbol{W}_a\boldsymbol{G}^{+}\boldsymbol{W}_b\right] \end{aligned} \tag{2.86}$$

where

$$\boldsymbol{W}_i = \begin{pmatrix} 0 & 0 & \dots & 0 & 0 \\ \vdots & \vdots & \ddots & \vdots & \vdots \\ 0 & 0 & \dots & 0 & 0 \\ 0 & 0 & W_i & 0 & 0 \\ 0 & 0 & \dots & 0 & 0 \\ \vdots & \vdots & \ddots & \vdots & \vdots \\ 0 & 0 & \dots & 0 & 0 \end{pmatrix} \tag{2.87}$$

.

To calculate the transmission coefficients at many energy points the inverse $\boldsymbol{G'} = (E\boldsymbol{I} - \boldsymbol{H'})^{-1}$ must be recalculated for each energy point. Alternatively, the eigenvalue

problem of the complex symmetric matrix $\boldsymbol{H}'$,

$$\boldsymbol{H}' C_k = \left(E_k - \frac{i}{2} \Delta_k \right) C_k \tag{2.88}$$

where E_k and Δ_k are the real and imaginary parts of the eigenvalues, can be solved. This allows use of the spectral decomposition of the Green's matrix

$$\boldsymbol{G}'(E) = \sum_k \frac{C_k C_k^T}{E - E_k + \frac{i}{2}\Delta_k}. \tag{2.89}$$

In this way only one diagonalization is needed and the Green's function is available for any energy at once. The dimension of the Hamiltonian is large, but it is a sparse matrix so efficient diagonalization algorithms can be used. Additionally, the expansion can be truncated by only including eigenfunctions with a real part of the energy below a preset maximum. Numerical tests show that high-lying states do not contribute to the spectral decomposition in the desired energy range around the Fermi energy. Note that if the size of the Hamiltonian matrix does not allow direct diagonalization then one can use recursive methods, for example, those based on damped Chebyshev polynomial expansions[75–77] or the Lanczos algorithm[78,79].

With the spectral representation, the transmission coefficient is rewritten in an explicitly energy dependent simple form

$$T_{ab}(E) = \sum_{ij} \frac{1}{E - E_i} \frac{1}{E - E_j^*} \boldsymbol{U}_{ij}^a \boldsymbol{U}_{ij}^b \tag{2.90}$$

where

$$\boldsymbol{U}_{ij}^{n} = \sum_{kl} C_{ki}(\mathbf{W}_n)_{kl} C_{lj}^{*}. \tag{2.91}$$

This form again shows that once the eigenvalue problem is solved, the transmission coefficient is available for any energy.

Alternatively, Eq. (2.71) can be used to calculate the transmission coefficient. In that case, the Green's function of each lead has to be calculated separately,

$$g_n'(E) = (ES_n - H_n')^{-1}. \tag{2.92}$$

Once the leads' Green's functions are available, the imaginary part of the leads' self energy can be calculated and Eq. (2.71) can be used.

In the zero bias (equilibrium) case, the electron density can be calculated in the conventional way using Eq. (2.89). In the non-equilibrium case, the density can be calculated as[45]

$$\rho(\mathbf{r}) = \sum_{\mu,\nu} \phi_{\mu}^{*}(\mathbf{r}) \mathrm{Re}\left[\boldsymbol{D}_{\mu\nu}\right] \phi_{\nu}(\mathbf{r}), \tag{2.93}$$

where ϕ_ν are basis functions and $\boldsymbol{D}$ is the density matrix defined by[45]

$$\begin{aligned}
\boldsymbol{D} &= \sum_{b} \frac{1}{2\pi} \int_{-\infty}^{+\infty} dE \boldsymbol{G}'(E) \boldsymbol{W}(E) \boldsymbol{G}'^{\dagger}(E) f(E-\mu_b) && (2.94)\\
&= -\frac{1}{\pi} \int_{-\infty}^{+\infty} dE \mathrm{Im}\left[\boldsymbol{G}'(E) f(E-\mu_a)\right] && (2.95)\\
&\quad + \frac{1}{2\pi} \sum_{b\neq a} \int_{-\infty}^{+\infty} dE \left[\boldsymbol{G}'(E) \boldsymbol{W}_b(E) \boldsymbol{G}'^{\dagger}(E)\right] \times \left[f(E-\mu_b) - f(E-\mu_a)\right].
\end{aligned}$$

Using the spectral representation (Eq. (2.89)) the density matrix can be rewritten as

$$\begin{aligned}\boldsymbol{D}_{\nu\mu} &= -\frac{1}{\pi}\int_{-\infty}^{+\infty} dE \mathrm{Im}\left[\sum_k \frac{C_{\nu k}C^*_{\mu k}}{E - E_k + \frac{i}{2}\Delta_k} f(E-\mu_a)\right] \\ &+ \frac{1}{2\pi}\sum_{b\neq a}\int_{-\infty}^{+\infty} dE \left[\sum_{ij}\frac{C_{\nu i}C^*_{\mu j}\boldsymbol{U}^b_{ij}}{(E - E_i + \frac{i}{2}\Delta_i)(E - E_j - \frac{i}{2}\Delta_j)}\right] \times [f(E-\mu_b) - f(E-\mu_a)] \\ &= \mathrm{Im}\left[\sum_k C_{\nu k}C^*_{\mu k}p^a_k\right] + \sum_{b\neq a}\sum_{ij} C_{\nu i}C^*_{\mu j}\boldsymbol{U}^b_{ij}q^{ab}_{ij}\end{aligned} \tag{2.96}$$

where

$$p^a_k = -\frac{1}{\pi}\int_{-\infty}^{+\infty} dE \frac{1}{E - E_k + \frac{i}{2}\Delta_k} f(E-\mu_a), \tag{2.97}$$

and

$$q^{ab}_{ij} = \frac{1}{2\pi}\sum_{b\neq a}\int_{-\infty}^{+\infty} dE \frac{f(E-\mu_b) - f(E-\mu_a)}{(E - E_i + \frac{i}{2}\Delta_i)(E - E_j - \frac{i}{2}\Delta_j)}. \tag{2.98}$$

CHAPTER III

COMPUTATION

Computational techniques take on a large role in quantum mechanical simulations due to the increased demands on computer resources such as memory and CPU power. This section presents details related to a number of computational issues including the numerical solution of self-consistent problems, parallelization of a density functional theory code with an atomic orbital basis set, convergence of computed transport properties, memory efficiency and implementation of finite difference operations.

3.1 Self-consistent solution

The Kohn-Sham equations, Eqs. (2.3), depend on the electron density and the electron density depends on the eigenfunctions of the Kohn-Sham equation through Eq. (2.4). This dependence requires a self-consistent solution. Solving a non-linear self-consistent eigenvalue problem is non-trivial and requires much computational effort. The steps of a typical self-consistent calculation are shown in Figure 3.1. First an initial guess is generated. Then the matrix elements of the Hamiltonian are calculated from the density. This step involves the solution of the Poisson equation to obtain the Hartree potential and the calculation of the exchange and correlation potential. These are the main parts of the density functional Hamiltonian which depend on the electronic density. There are various methods to calculate a new density from the Hamiltonian. As mentioned above, one possibility is to construct

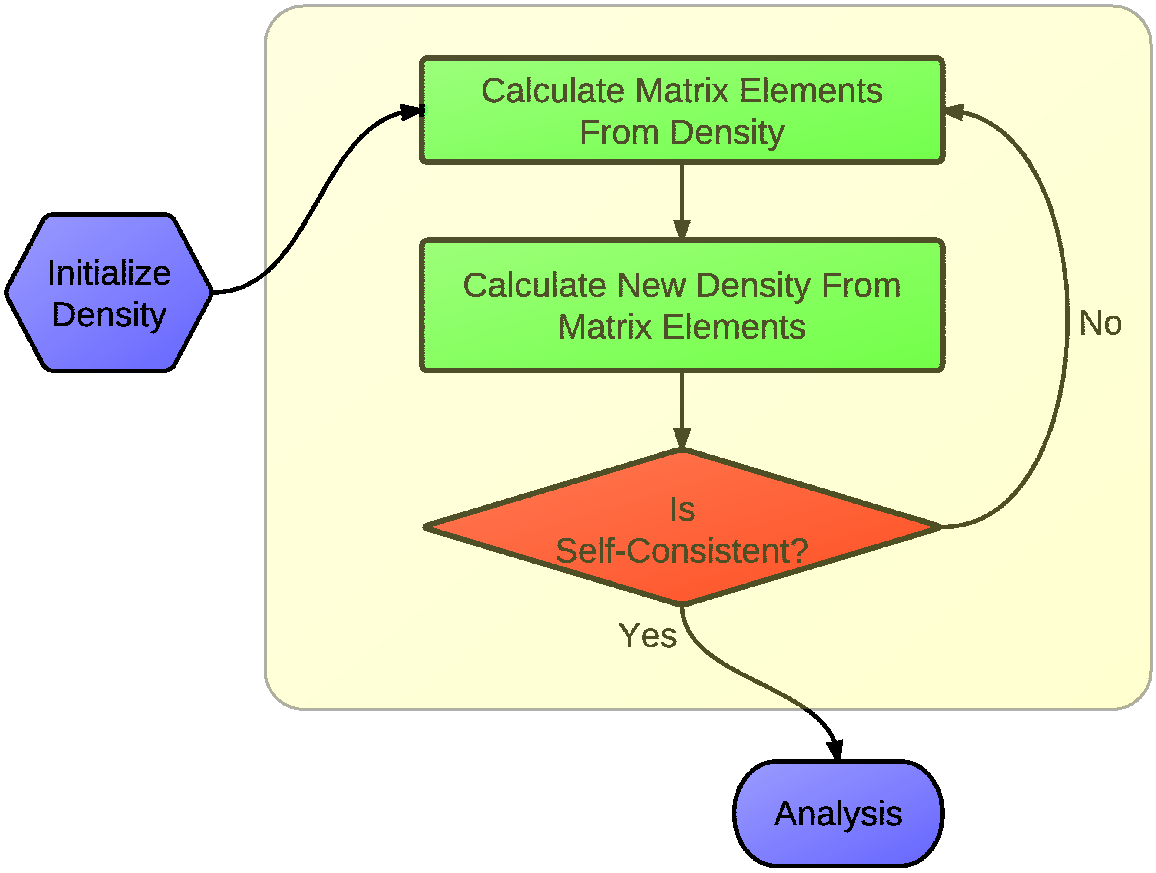

Figure 3.1: Self-consistent solution procedure

the new density through Eq. (2.4). In the case of a transport calculation the Green's function is calculated from the Hamiltonian and is then integrated over energy to obtain the new density. This new density is checked against the input density; if the two match then the loop exits and analysis of the data can be done. Otherwise, a new trial density is generated and the procedure is repeated.

An important detail is how the new trial densities are generated. Simply using the newly calculated density as the new trial density will not work due to the nonlinear nature of the problem. The most obvious scheme is to take a linear combination of

the input, $\boldsymbol{n}_{i-1}$, and output density, $\boldsymbol{n}_i$

$$\boldsymbol{n}_{i+1} = (1-\alpha)\boldsymbol{n}_{i-1} + \alpha\boldsymbol{n}_i. \tag{3.1}$$

Here α is a small parameter which is typically $0.001 - 0.1$ depending on the problem and completeness of the basis. While solution of the self-consistent problem is now possible, this approach is very inefficient. A simple improvement is to dynamically adjust α at each iteration. Further efficiency gains can be made with more advanced algorithms.

Pulay mixing, also known as DIIS (Direct inversion in the iterative subspace), is the standard approach used in many codes[80]. The method is essentially a least squares extrapolation to the density with minimal residual at each step. I have implemented both dynamically adjusted linear mixing and Pulay mixing in the group's DFT code. Figure 3.2 shows a comparison of the methods.

Here I provide details of the implementation and derivation of the Pulay scheme implemented in the code. Start with the assumption that the final self-consistent density, $\boldsymbol{n}$, can be approximated by a linear combination of previous guess vectors

$$\boldsymbol{n} = \sum_{i}^{m} c_i \boldsymbol{n}^i. \tag{3.2}$$

This assumption holds if the previous guess vectors, $\boldsymbol{n}^i$, are near enough to the solution, which is the case in typical calculations. The residual vector can also be

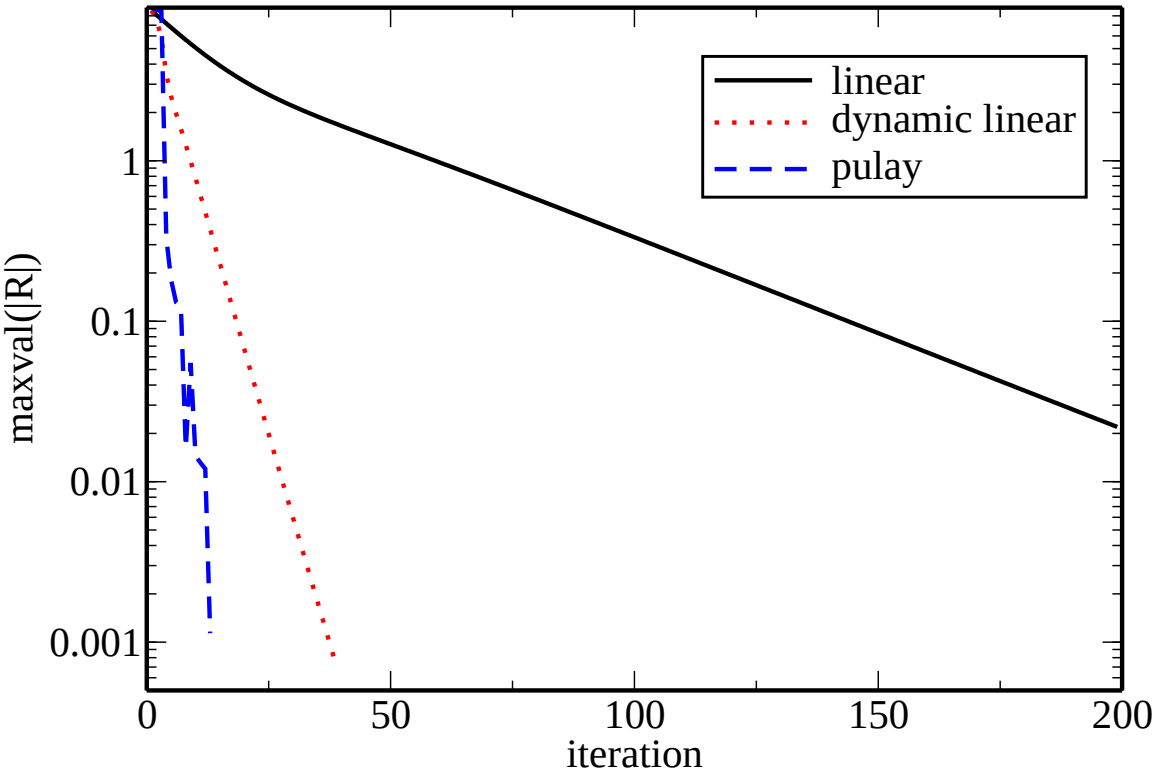

Figure 3.2: Comparison of density mixing methods for an NH_3 molecule. The maximum value of the residual of the density as a function of self-consistent iteration is shown.

written in this form,

$$\boldsymbol{r} = \sum_{i}^{m} c_i \boldsymbol{r}^i. \tag{3.3}$$

A correct solution will minimize the norm of the residual vector,

$$\langle \boldsymbol{r} | \boldsymbol{r} \rangle = \sum_{ij}^{m} c_i^* c_j \langle \boldsymbol{r}^i | \boldsymbol{r}^j \rangle \tag{3.4}$$

with the constraint that $\sum_i^m c_i = 1$. The equation to minimize is then

$$L = \boldsymbol{c}^\dagger \boldsymbol{S} \boldsymbol{c} - \lambda \left(1 - \sum_{i}^{m} c_i \right) \tag{3.5}$$

where λ is a Lagrange multiplier and $S_{ij} = \langle \boldsymbol{r}^i | \boldsymbol{r}^j \rangle$. Taking $\frac{\partial L}{\partial c_k} = 0$ the following linear equation is obtained

$$\begin{pmatrix} S_{11} & S_{12} & \dots & S_{1m} & -1 \\ S_{21} & S_{22} & \dots & S_{2m} & -1 \\ \dots & \dots & \dots & \dots & \dots \\ S_{m1} & S_{m2} & \dots & S_{mm} & -1 \\ -1 & -1 & \dots & -1 & 0 \end{pmatrix} \begin{pmatrix} c_1 \\ c_2 \\ \dots \\ c_m \\ \lambda \end{pmatrix} = \begin{pmatrix} 0 \\ 0 \\ \dots \\ 0 \\ -1 \end{pmatrix}. \tag{3.6}$$

This linear equation is easily solved to obtain the desired c_i which are then used to construct a density with minimal residual. In large systems long wavelength oscillations in the charge density can make convergence difficult to obtain. These oscillations can be damped by using a modified metric to compute the distance between trial

solutions, S_{ij} in Eq. (3.6). The metric is defined in terms of q, the wave vector

$$\langle a|b\rangle = \langle a|M|b\rangle, \tag{3.7}$$

where $M = \sum |q\rangle f(q)\langle q|$ and $f(q) = 1 - \frac{w}{q}$[81]. The parameter w determines the strength of the damping. This form of the metric is used in planewave calculations, with the idea that contributions from low wave vectors have greater effect that those from high wave vectors. In real space the metric is approximated by

$$f(R) = \begin{cases} 1 + w/8 & R = 0 \\ w/16 & R = 1 \\ w/32 & R = 2 \\ w/64 & R = 3 \end{cases} \tag{3.8}$$

where R = 0 is the on the grid point, R = 1 is the 1st nearest neighbor point, and so on. Tests show that use of this metric reduces the number of required self-consistent iterations in large systems.

3.2 Parallel implementation

Often when calculating the properties of systems with large simulation cells and many atoms, the required walltime and memory will be too great. A parallel implementation can reduce the wait for results or increase the available memory by distributing the calculation across a number of processors. I have developed parallel DFT and NEGF codes using a combination of OpenMP, for use on shared memory

systems, and MPI for communications between nodes.

The density functional theory code is parallelized at a high level over atomic orbitals. A subset of orbitals that overlap is assigned to each node. Figure 3.3a shows the non-zero matrix elements in the calculation with each color representing a different node. The localized nature of the orbitals makes this distribution suited to calculating matrix elements and the density. However, this distribution is not efficient for the solution of eigenvalue problems. An algorithm converts this parallel representation to a two-dimensional block cyclic representation for use with the parallel linear algebra library ScaLAPACK[82]. Figure 3.3b shows the distribution of non-zero matrix elements in the two-dimensional block cyclic case. The scaling of the approach is shown in Figure 3.4. The poor scaling of the diagonalization routine is the limiting factor of the straight forward approach. More sophisticated diagonalization methods such as RMM-DISS or subspace diagonalization are more suited to parallel computation and are under consideration. Alternatively, the diagonalization can be avoided entirely by calculating the Green's function from the Hamiltonian and integrating over energy to obtain the new density. In this approach every energy point is independent, making parallelization trivial.

3.3 Convergence of transport properties

Calculations of transport properties with the NEGF formalism are expensive compared to standard ground state calculations. The main performance bottleneck is the calculation of the Green's function because it requires the inversion of the resolvent Hamiltonian. Small sets of atomic orbitals (AO) are often used to minimize the

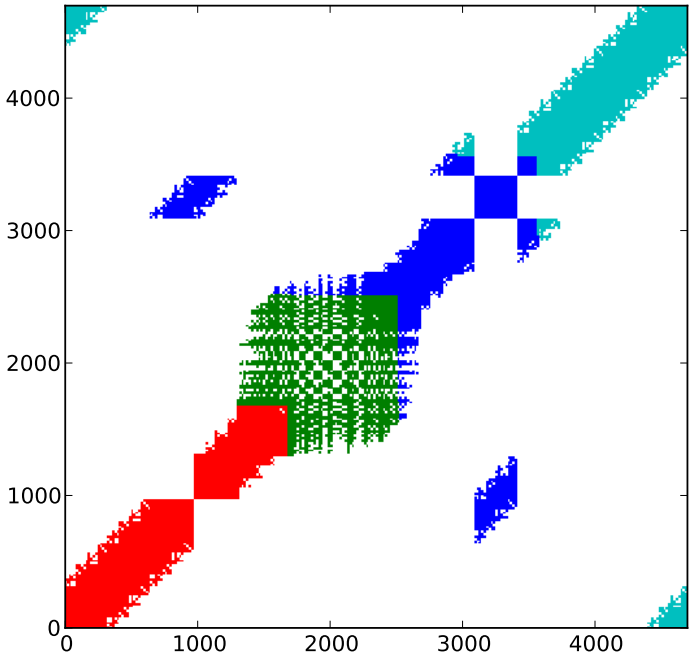

(a) Orbital pair distribution

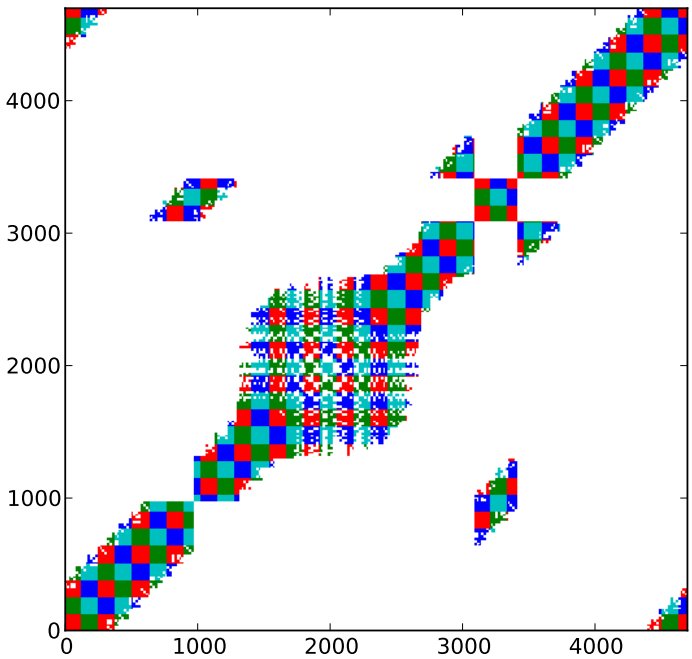

(b) Two-dimensional block cyclic distribution

Figure 3.3: Distributions of matrix elements used in parallel calculations. Each color represents a different processor

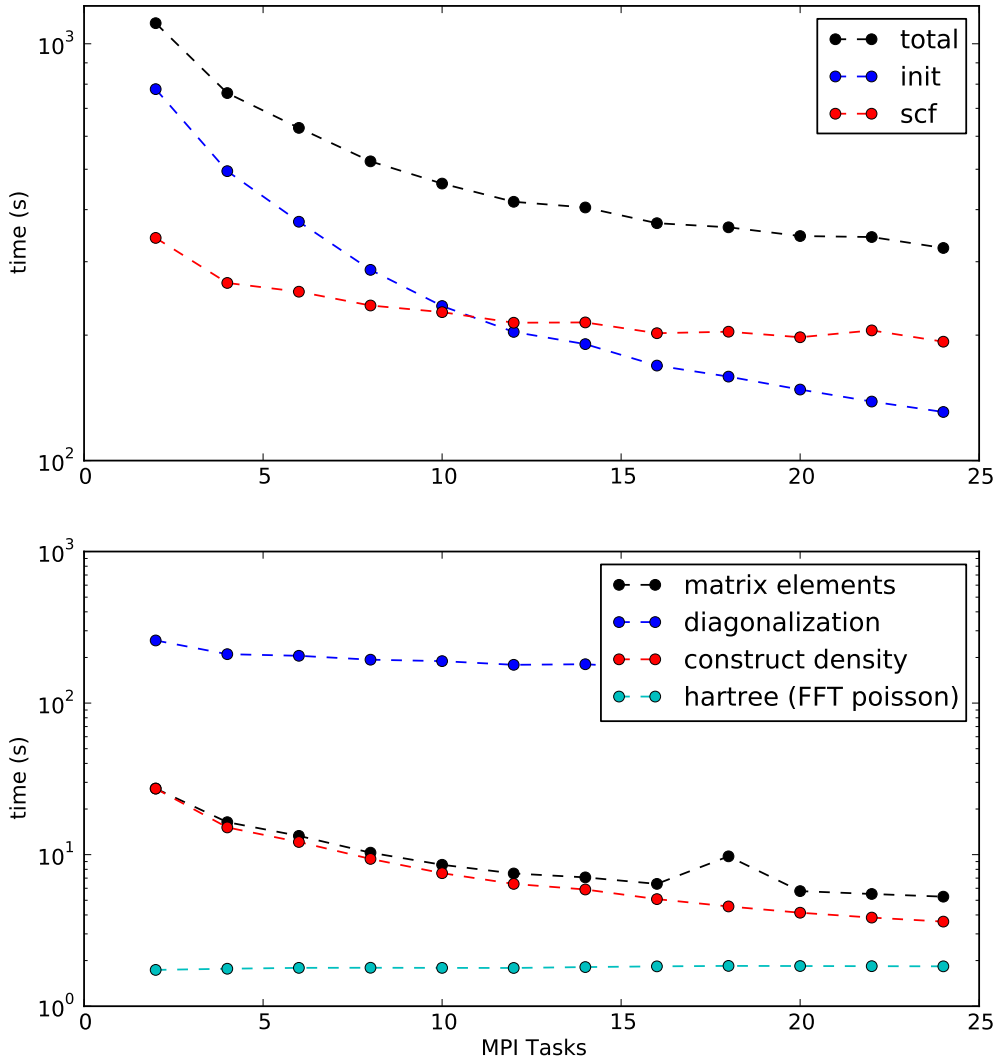

Figure 3.4: Parallel scaling of a calculation of tetraphenyl-porphyrin molecule contacted to two Au nanowires. There are 260 atoms in the simulation box and 4680 orbitals with a double zeta basis set. The calculation was done on 1 node of the Hopper machine at NERSC with two twelve-core AMD 'MagnyCours' 2.1-GHz processors.

dimension of the Hamiltonian. This approach has been very successful due to its simplicity. However, there are a number of problems. It is known that large numbers of AOs are needed to obtain converged transport properties[60]. Often 27 AOs per atom are needed. As a result, accurate calculations for large systems are often prohibitively expensive.

In this subsection the convergence of the transmission coefficient is investigated. The calculation is performed with a large atom-centered basis set. Before the Green's function is calculated the system is divided into boxes. In each box, the Hamiltonian is diagonalized and the eigenstates are ordered by energy. From each box the N lowest energy states are used as a new basis for the system, upon which the full Hamiltonian of the system is now projected. By arranging the boxes such that their dividing walls are orthogonal to the transport direction, the desired tridiagonal form for the Hamiltonian is retained. This allows the reuse of computation routines designed for use with the AO basis and the accuracy of large atomic orbital basis sets without the full cost of inverting the Hamiltonian.

3.3.1 Example: Au chain with adsorbed CO

As a simple example a CO molecule adsorbed onto a mono-atomic gold chain is used. The transmission coefficient calculated with different sized atomic orbital basis sets is shown in Figure 3.5. In this case 27 basis functions per atom were required to converge the transmission curve. This corresponds to an expensive calculation for even modest systems with fewer than 100 atoms. In Figure 3.5 the transmission coefficient was computed with the method described above. Initial calculation was

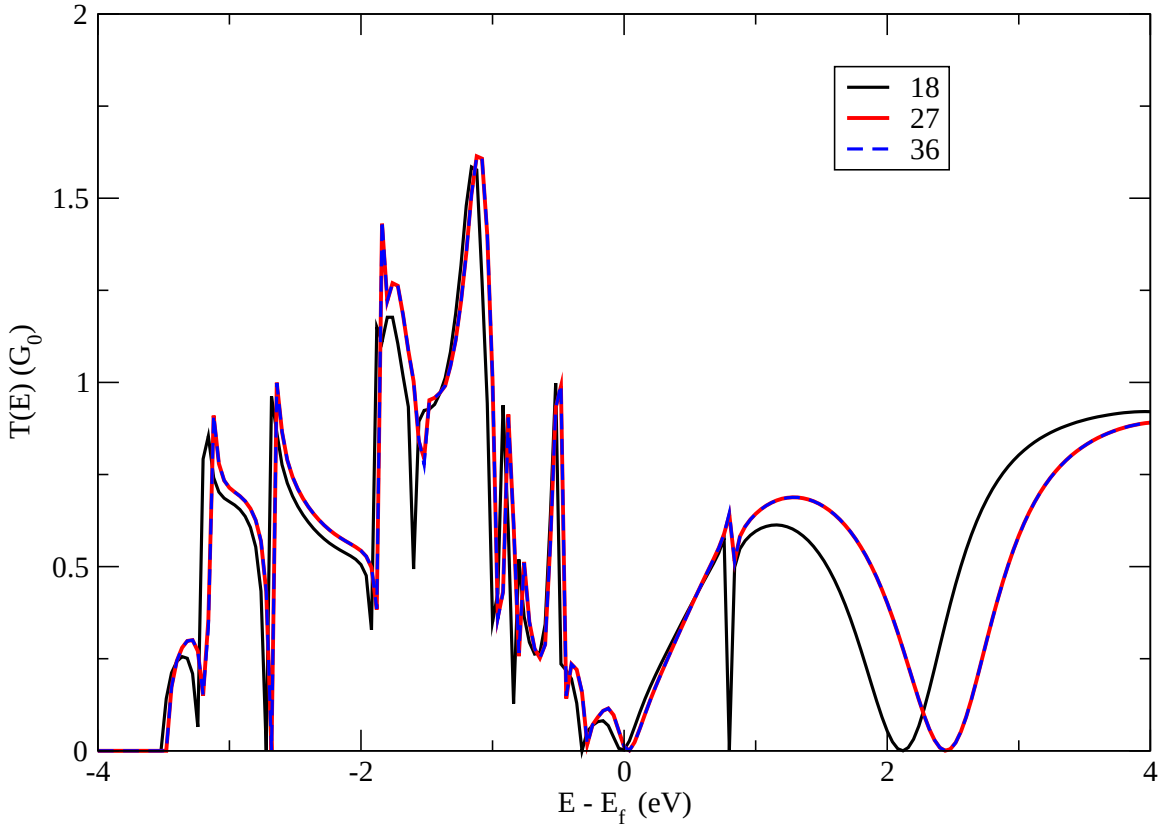

Figure 3.5: Transmission coefficient as a function of energy for a Au chain with an adsorbed CO molecule. For each curve the self-consistent ground state and transmission is calculated with the basis set indicated. A basis set of 27 or more AOs per atom is needed to obtain a converged transmission curve.

done with 36 atomic orbitals per atom. The legend indicates the number of states per atom that were kept in the calculation. This is proportional to the dimension of the Hamiltonian and Green's function. The accuracy of the full 36 state-per-atom calculation was achieved with 18 states per atom using the box basis method.

3.4 Memory efficiency

A common situation is that more memory is required than is currently available. If after distributing the problem across several CPUs more memory is still needed,

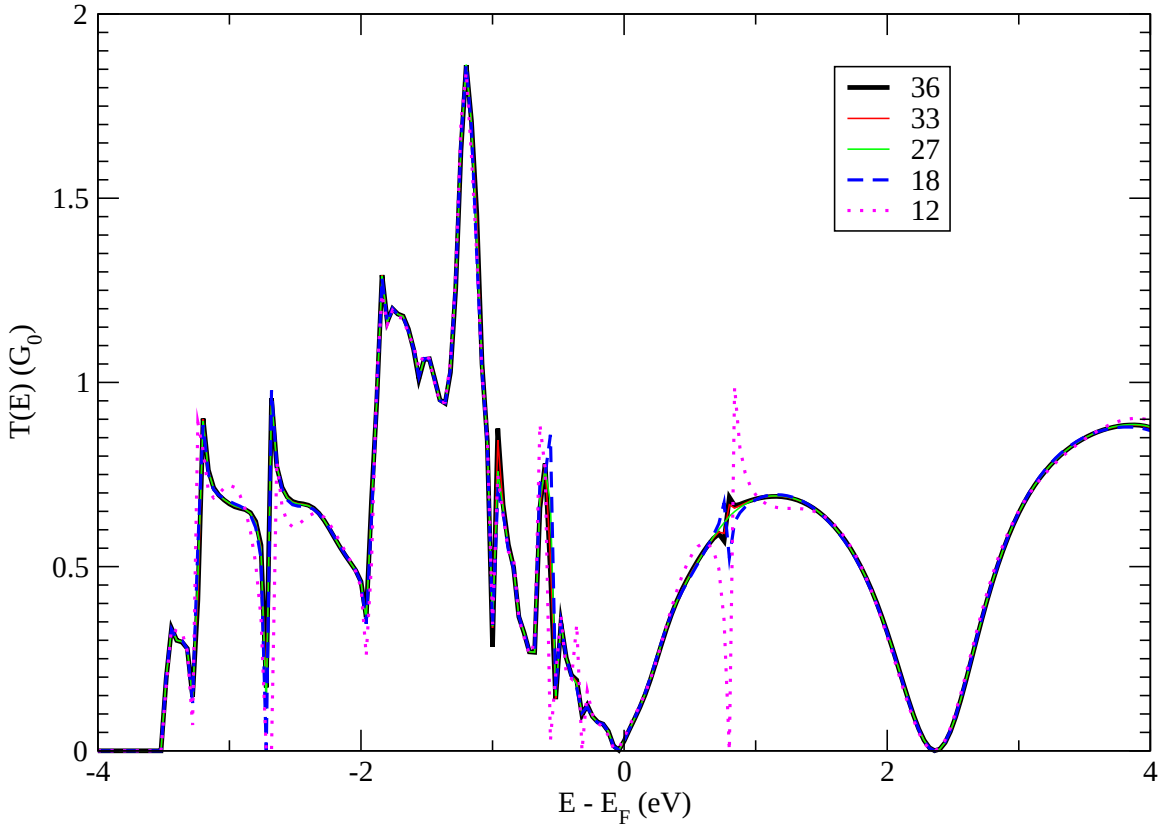

Figure 3.6: Transmission coefficient as a function of energy for a Au chain with an adsorbed CO molecule. The legend indicates the number of basis states per atom used in the calculation of the truncated basis and transmission curve. The solid black curve calculated with 36 states corresponds to the full 4-zeta basis. All curves except for "12" are on top of each other.

it is possible to recalculate the real-space representation of the atomic orbital basis functions as needed instead of precomputing and storing the values. The real-space representation of the orbitals represents a significant memory requirement. For example, in a system with $N_o = 10000$ orbitals, a grid spacing of 0.25 and an orbital cutoff radius of $r_{cut} = 4.5$ Å, a sphere of radius r_{cut} around an atom will contain roughly $N_g \approx 20000$ grid points. Since the value of the orbital at each point is required, $N_g N_o$ double precision values must be stored in memory — taking up roughly 1.6 GB. In a parallel calculations there is some overhead due to multiple CPUs needing copies of

a given orbital.

The group's DFT code now contains the option to recalculate the real-space representation as needed. However, a naive implementation would result in a very inefficient code. Suppose there are two atoms which have overlapping basis functions and each atom has 18 atomic orbitals. Then, to calculate the overlap, the real-space representation must be accessed $18 \times 18 = 324$ times. It is undesirable to recalculate at every access for this reason. Ideally it should be calculated once at each self-consistent step. The code implements a least recently used (LRU) caching algorithm.

The algorithm is effective because of the localized nature of the orbitals. Atoms are ordered so that spatial locality is maximized; in the case of a system with one dimension larger than the others (as in a nanowire) this amounts to ordering the atoms by their coordinate along the transport axis. So an orbital only overlaps with a finite set of other orbitals, which will have a nearby index. In a loop over all pairs of orbitals a certain real-space representation will be accessed many times in a short number of iterations and then much less frequently elsewhere. The LRU cache manages accesses to the representations. A preset maximum number of representations will be stored at a time. When a representation is requested a check is done to see if it is in the cache. If it is, then the value is returned immediately, and is marked as accessed. If not, the value is calculated and copied into the cache. When the cache is full, the representation which has not been accessed recently is replaced by the newly requested value. The walltime as a function of number of stored representations is shown in Figure 3.7. After a critical value of cache size is reached the walltime is significantly reduced. This is related to the finite number of orbitals that each orbital overlaps.

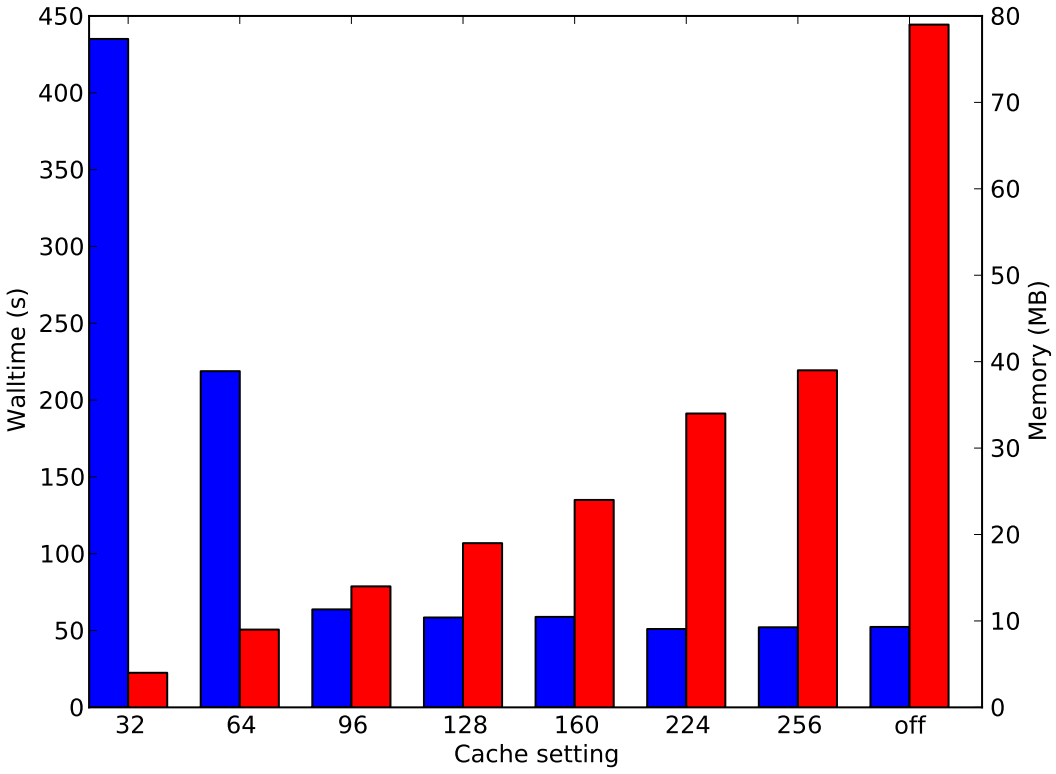

Figure 3.7: Walltime and memory as a function of cache size setting. Walltime is shown in blue and memory needed for the real-space representation is shown in red. The test system is a gold chain with an adsorbed CO molecule. There are 29 atoms and 512 basis functions in the calculation.

The crossover point, and thus the required size of cache for efficient calculations, can be estimated by $M_{int}N_{AO}$ where M_{int} is the average number of atoms within a radius of $2r_{cut}$ from each atom and N_{A0} is the average number of orbitals per atom. In the test case shown in Figure 3.7 with are 512 basis functions and 29 atoms $M_{int} \approx 5$ and $N_{AO} = 18$ so the speedup should occur when approximately 90 basis function representations are stored. As the transition does not depend on the total number of atoms or basis functions significant memory savings are possible in large systems.

3.5 Finite difference operations

Computing the action of finite difference operators on quantities defined on a grid represents a significant factor in many computations. Especially in the case of a large system with many grid points and a grid basis. Most commonly one uses the Laplace operator in the calculation of the kinetic energy and in the solution of the Poisson equation. In this section efficient implementation of the action of Laplace operator is shown.

As in (2.19) the action of a fourth order finite difference Laplace operator on a function f is

$$\nabla^2 f(i,j,k) = \sum_{n=-4}^{4} C_n f(i+n,j,k) + C_n f(i,j+n,k) + C_n f(i,j,k+n), \qquad (3.9)$$

where C_n are finite difference coefficients. For a simplified discussion a first order finite difference operator will be used in the examples. A straightforward implementation in FORTRAN is given below:

```
1 do k=1,z
2 do j=1,ny
3 do i=1,nx
4    nab_f(i,j,k) = c0*f(i,j,k) + &
5     c1*(f(i-1,j,k)+f(i+1,j,k)+f(i,j-1,k)+f(i,j+1,k)+f(i,j,k-1)+f(i,j,k+1))
6 end do
7 end do
8 end do
```

This style of implementation suffers from poor memory access properties and will as a consequence run slowly. Better spatial and temporal memory locality can be

achieved introducing a block size.

```
1 do kk=1,nz,bs
2 do jj=1,ny,bs
3 do ii=1,nx,bs
4    do k=kk,min(nz, kk+bs-1)
5    do j=jj,min(ny, jj+bs-1)
6    do i=ii,min(nx, ii+bs-1)
7       nab_f(i,j,k) = c0*f(i,j,k) + &
8                      c1*(f(i-1,j,k)+f(i+1,j,k)+f(i,j-1,k)+f(i,j+1,k)+f(i,j,k-1)+f(i,j,k+1))
9    end do
10   end do
11   end do
12 end do
13 end do
14 end do
```

The exact value of *bs* needed for optimal performance depends on the specific system, and factors such as cache size will result in different performance characteristics. Numerical tests with an Intel Core 2 Quad suggests a value in the range 8-20 is a good choice for *bs*. An alternative is to reorder grid points themselves, but this results in a more complicated mapping of grid point index to spatial location.

CHAPTER IV

NANOWIRES

In this chapter transport properties of nanowires are studied with first-principles calculations. Relevant experimental and theoretical findings are discussed in Section 4.1, followed by specific calculations. Sections 4.2 through 4.4 focus on the electronic properties of kinked nanowires. The role of quantum interference effects in atomic chains, silicon nanowires and graphene nanoribbons is examined in these sections. The final sections relate to gold nanowires: Section 4.5 discusses the impact of structural changes in nanowires undergoing elongation on the observed conductance traces, and Section 4.6 investigates the properties of a proposed molecular switch based on a porphyrin molecule in a gold nanowire break junction. The work presented in this chapter on atomic chains, silicon nanowires and gold nanowires has been published[11,13].

4.1 Background

One-dimensional nanowires exhibit outstanding electronic, transport and optical properties[83–86] and are promising candidates for future nanodevice applications[87–89]. The electrons in these structures are subject to quantum confinement and their motion is limited to one dimension leading to unique effects such as quantized conductance[3,90], Peierls instabilities[91] and Luttinger liquid behavior[92]. Nanowires with a wide range of composition and morphology have been observed. Crystalline wires with

diameters $\sim 0.5 - 500$ nm composed of metals, such as gold or silver[93], semiconductors such as silicon and GaAs[94], and insulators such as SiO_2 have all been fabricated. Additionally, a range of core-shell structures[89,95], dopant distributions[96–98] , surface terminations[96,99] and crystallographic orientations[100–102] have been explored. Chains composed of single atoms are less common, but are found in break junctions[3,90,103] and on surfaces[104–109]. Molecular units, such as DNA or thin strips of graphene[110], also exhibit one-dimensional phenomena and can be considered as nanowires. The large range of possible configurations allow significant influence over the properties of nanowires, motivating the extensive study of how to effectively tune wire parameters.

In a perfect one dimensional nanowire the conductance is equal to NG_0 where $G_0 = e^2/h$ is the conductance quantum and N is the number of available conduction channels at the Fermi energy. Defects in the wire introduce a scattering potential causing reflections which alter the electronic properties of the nanowire. An example, the decrease in conductance of an mono-atomic chain of Au atoms when a CO molecule is adsorbed, is described in subsection 3.3.1. Some possible defects are surface reconstructions, dopant atoms and change in crystallographic orientation. Scattering on defects causes an interference between the scattered wavefunctions inducing resonances, standing waves and other quantum phenomena that alter the conductance of the nanowire.

Recent advances in experimental methods have allowed the introduction of kinks, turns and zigzags in nanowires with control over direction, length and placement[86,111,112]. Similar control has been demonstrated over the geometry of graphene nanoribbons[113,114]. Control over the kinking of Ge nanowires has been achieved via chemical means, allow-

ing the easy selection of kinked wire geometry[115]. These kinked wires are envisioned as nonlinear connections between nanodevice components, allowing for design of circuits and topologies that are impossible or impractical with straight wires only. The controllable nature of these defects offers the opportunity to further explore the role of defects in nanowires. Work presented in this chapter is focused on understanding the effects of kink defects on electronic properties.

4.1.1 Atomic chains

In mechanically controlled break junction experiments a thin wire is pulled apart in a vacuum at low temperature. Early observations found quantization of conductance in break junctions[103]. Later efforts included imaging the structures simultaneously with conductance measurements and improved control over atomic chain formation[3,90]. Chains of gold atoms that were approximately 1 nm long were observed.

Chains of atoms on surfaces are typically formed via manipulation of atoms, either with a scanning tunneling microscope(STM) or via self-assembly. Early observations found self-assembled chains of indium atoms could be combined through manipulation with a STM tip to form wires over 70 nm long on Si(100)2x1 surfaces[107]. Researchers were aware of the potential of atomic chains on surfaces as platforms for studying low-dimensional transport physics. A STM was used to create chains of gold atoms on NiAl(110) surfaces and spatially resolved conductance measurements of a chain with 20 atoms provided the effective electron mass, dispersion relation and density of states in the one-dimensional wire[104]. Gold wires on Si(335) surfaces have

been characterized with STM and tight-binding calculations illustrated the interaction between neighboring chains[105]. Wang et al. characterized self-assembled gold chains on Ge(001) and examined the growth process[106]. Later, others found that gold chains on this surface are very loosely coupled to the surface and other wires, demonstrating one-dimensional electron liquid behavior[109]. After continued study the same group published evidence of Tomonaga-Luttinger liquid behavior, a signature of one-dimensional electrons, in the Au-Ge(001) system[108].

4.1.2 Silicon nanowires

Several investigations of transport properties in silicon nanowires have been carried out[116–131]. A variety of methods have been used, *ab initio* and tight-binding approaches have both been used with Green's function and transfer matrix based approaches for the transport. Studies of pristine, passivated and doped wires have been published and the effects of surface defects has also been studied.

A number of works examined the link between wire surfaces and electronic properties. The IV characteristics of small pristine and passivated (hydrogen) wires were calculated with NEGF-DFT by Ng et al. IV characteristics are shown to depend strongly on length, growth direction and surface passivisation. The effect of metal electrodes is examined and a wire length of 3 nm is suggested as a minimum to regain intrinsic wire properties[118]. Lherbier et al. used a Kubo-Greenwood approach and an NEGF-DFT approach to explore the effects of surface roughness in different transport regimes[127]. Svizhenko et al. used a NEGF-TB approach to study the effects of growth direction and surface roughness on small passivated (hydrogen) wires. A

current falloff at high bias voltage is calculated. Surface roughness is found to suppress low bias current and conductance and to decrease the current as wire length is increased. They suggest that in small wires a transition to the Anderson localization regime may occur at room temperature[119]. Markussen et al. calculated the resistance and mean free path in long wires. A real-space Kubo method and a recursive Green's function method were both used to study metallic and semiconducting wires; both methods are shown to give similar results. Long unpassivated wires are found to be very sensitive to defects in the surface but largely unaffected by disorder in the wire core. A strong dependence on defects in the surface passivisation is also found[124]. Ponomareva et al. studied the energetics of various wire geometries and found that tetrahedral wires in [111] direction were the most stable. They also discovered that these wires have superior conducting properties when compared to other wire geometries. Their results are obtained with a tight-binding approach, but they do some supplemental calculations with an *ab initio* method. The transport results were obtained with a transfer matrix approach[122].

Other works instead focused on the role of dopants in nanowires. Crossover from ballistic to diffusive transport when silicon nanowires are doped with B or P was studied from a perspective of scaling theory[132]. It was found that information from single dopant scattering was sufficient to predict the main trends of the crossover. The energetics of Mn doped Si nanowires was studied by Giorgi et al.[133]. They demonstrated the role of Mn's favored alignment in $\langle 111 \rangle$ Si nanowires in stabilizing the ferromagnetic ordering. The effects of dopants on conductance in passivated wires was studied by Serra et al. with an *ab initio* method based on the Landauer

formalism. Impurities in the core are found to cause significant scattering and surface trapped impurities are found to have little effect[120]. In contrast to bulk Si, B-doped nanowires have lower resistance than those doped with P (the opposite is true in bulk)[121].

Some authors have focused on the properties of interfaces. The interface between Al(100) wires and carbon nanotubes was found to reduce the measured conductance of carbon nanotubes[7]. Landman et al. studied passivated nanowires connected to aluminum electrodes. They find that short wires (less than 1 nm) are metallic due to gap states induced by the contacts. Longer wires are found to have Schottky barriers with heights 1.5 to 2 times higher than the bulk value. Calculations were done with a combination of DFT and a transfer matrix approach[123].

Ricardo Rurali has written an extensive review article detailing previous studies from a theoretical point of view[134]. However, little work has been presented on kink defects in nanowire systems, first-principles or not.

4.2 Atomic chains

In this section various kinks are introduced in mono-atomic gold chains and the relation between kink geometry and change in conductance is examined. Background information is provided in Section 4.1.1. Atomic chains have proven to be good platforms for studying low-dimensional electron transport physics.

Kinked structures with 2, 3 and 4 turns are examined: an angle, a triangle and a step, respectively (see Figure 4.1). The Au-Au distance is fixed at 2.9 Å for all calculations in this section. The presence of a kink substantially modifies the potential felt

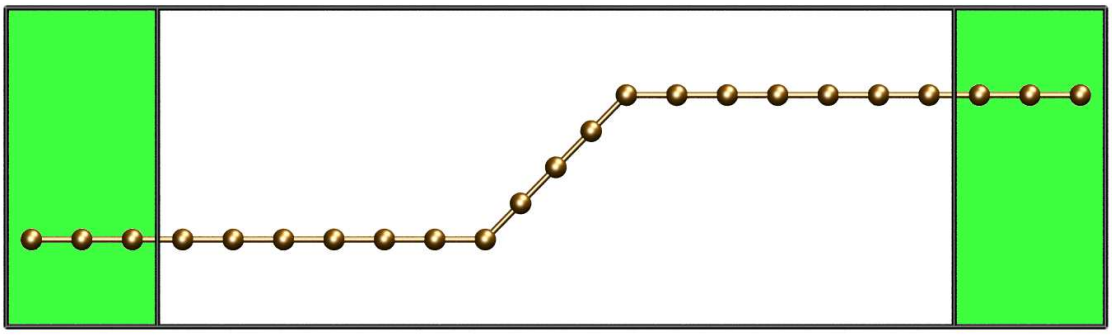

(a)

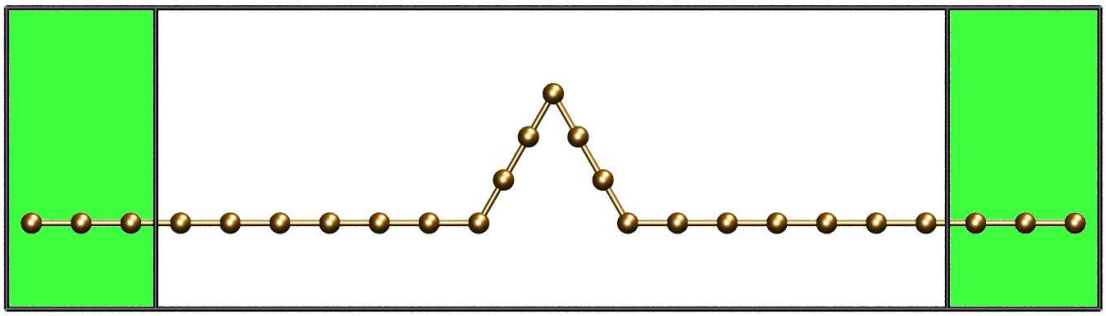

(b)

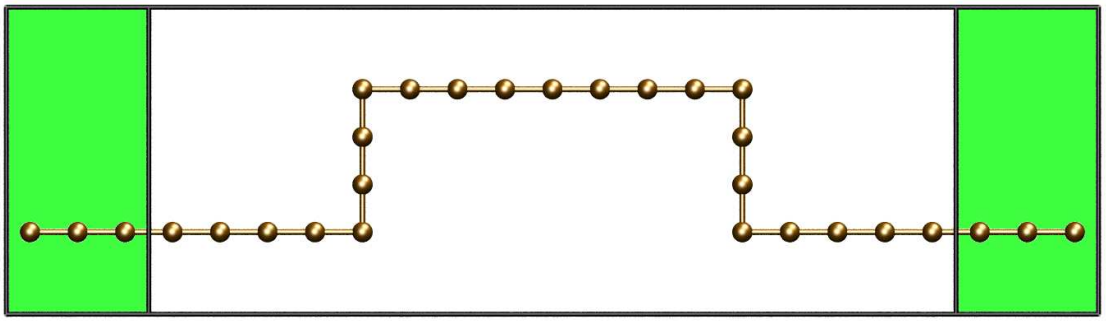

(c)

Figure 4.1: Au nanowires with different kinks. The boxes indicate electrode and scattering regions with the electrode region highlighted in green.

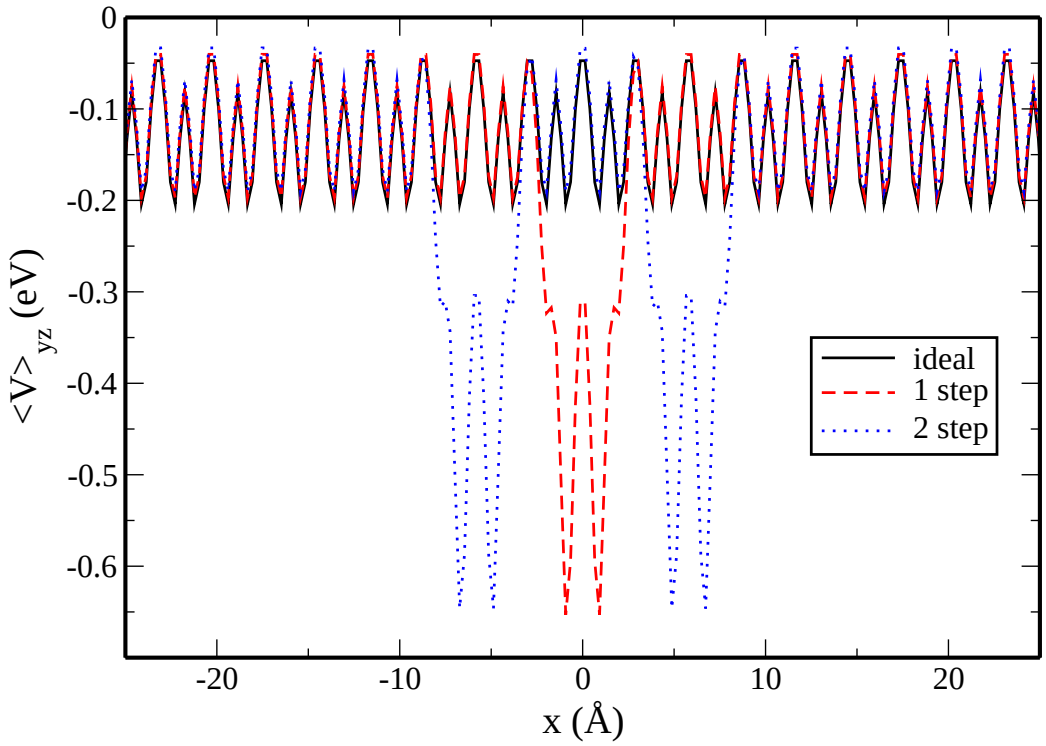

Figure 4.2: Average self-consistent potential along transport direction for several configurations. The potential is calculated by averaging the self-consistent potential along the transport direction.

by the electrons. This is illustrated in Figure 4.2 where the self-consistent potential in a straight wire is compared to a wire with an angle (Figure 4.1a, $\alpha = \pi/2$) and a step (Figure 4.1c). Figure 4.2 shows that the kinks introduce a substantial perturbation that depends on the geometry of the kinks. The conductance is supressed compared to a perfect wire by the introduction of the scattering potential (see Figure 4.3). Figure 4.3 shows that the transmission probability of a kinked wire depends on the kink angle and is reduced compared to the straight wire.

The geometry dependence of the low-bias conductance, $G = T(E_F)$, where E_F is the Fermi energy, for the three model kink structures (Figure 4.1) is shown in Figure 4.4. In the case corresponding to Figure 4.1a the two turns are separated by

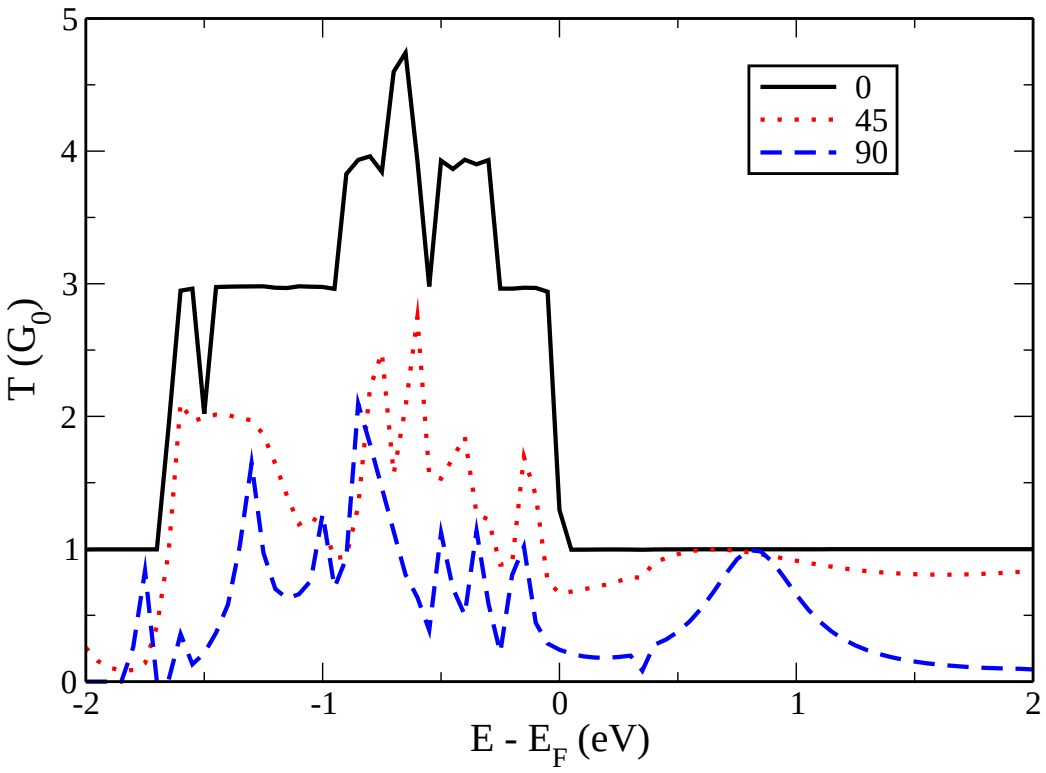

Figure 4.3: Transmission coefficient at zero bias for several kink angles of an monatomic gold chain in vacuum. The solid black curve corresponds to the infinite equally spaced chain in vacuum. Gold atoms are separated by 2.9 Å. A gold chain with an angled kink is shown in figure 4.1a

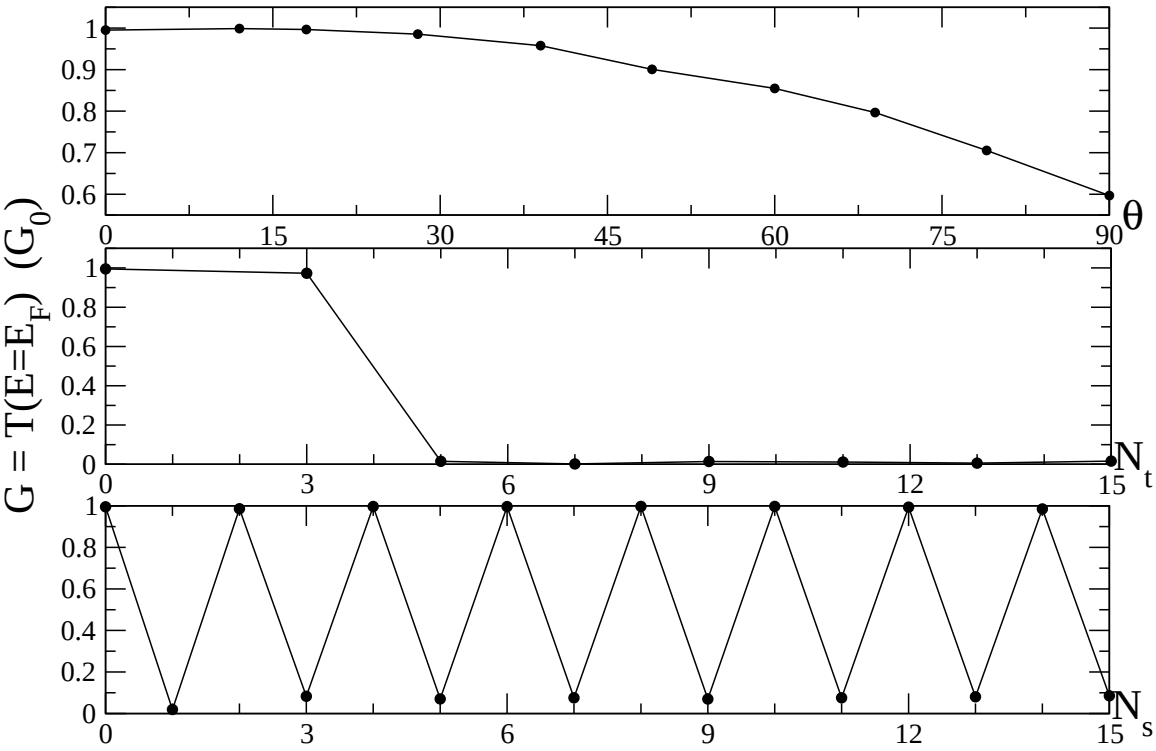

Figure 4.4: Conductance at the Fermi level for mono-atomic Au nanowires with a a) single kink as function kink angle b) triangular kink as a function of number of atoms in the triangle c) step as function of step length for a step height of 3 atoms.

5 atoms and the angle of α varies from 0 to $\pi/2$ (with 0 corresponding to no kink). For small angles, $\theta < \pi/6$, there is only a small decrease in conductance (Figure 4.4). The change in potential is lower when the kink has a low angle. In the range $\pi/6 < \theta < \pi/2$ the conductance steadily decreases as the angle is increased.

Increasing the number of turns, but maintaining the linear structure, gives a triangular kink (Figure 4.1b), chosen to be equilateral for simplicity. The number of atoms in the kink N_t is always odd because each leg has the same number of atoms. As N_t is increased, the conductance is suppressed, almost completely.

The last monatomic wire geometry studied is a step (Figure 4.1c). The conductance is calculated by fixing the number of atoms in the sides to be equal to three

and varying the number of atoms in the top segment. As the number of atoms in the top segment of the step, N_s, is increased there is an even-odd oscillation of the conductance. This even-odd oscillation is similar to the conductance oscillation behavior in ideal equally spaced atomic chains[135–138]. Some authors predict perfect conductance for chains composed of an odd number of atoms[136,137,139], some find the opposite[135,140]. Some authors predict oscillations with periods greater than two[141–143]. With the geometry shown in Figure 4.1c the even number chains are perfect conductors while the chains with an odd number of atoms have conductance of $G \approx 0$. An isolated short monatomic chain behaves like a molecule. The calculations show that the wavefunction of the lowest unoccupied state of the chain is an odd function if the number of the atoms in the chain is even and an even function if the number of atoms is odd. When the chain of atoms (top segment in Figure 4.1c) is contacted with the rest of the system, the wave function at the Fermi level is localized for odd number of atoms. An extended resonance like wavefunction is formed at the Fermi level with an even number of atoms. This latter wavefunction is a current carrying state while the former completely suppresses the conductance.

The variation of conductance in these model systems highlights some of the possible peculiarities of constructing circuits from kinked systems and illustrates the rich variety of possible conductance properties depending on the kink geometry.

4.3 Silicon nanowires

Silicon nanowires are single crystals of silicon which are thin in two dimensions and extended in the third. They are considered as potential building blocks for future

electronics[144]. Many devices based on silicon nanowires have been demonstrated, including diodes[144], transistors[144–146], chemical sensors[85] and lasers[147]. A brief overview of previous theoretical efforts focused on transport properties can be found in the introduction to this chapter (in section 4.1). Allowable geometries of nanowires are limited by several factors including crystal structure and growth conditions. The effect of kinks in realistic examples of Si nanowires[148] are presented in this section.

Many configurations are possible with Si nanowires and advances in experimental methods have allowed the introduction of kinks, turns and zigzags in nanowires with control over direction, length and placement[86,111,112]. Si nanowires are commonly grown along low-index crystal directions [100], [110], [111] and [112] and kinks between many of these directions have been observed. In the calculations a system of a [100] wire with a [111] kink is considered as shown in Figure 4.5. Along the [100] direction the wire is surrounded by 4 (100) surfaces and along the [111] direction the wire is surrounded by 6 (110) surfaces. The length of the [111] section along the transport direction is varied from $l = a/2$ to $l = 3a/3$, where a is the lattice constant of the wire. The wires have a diameter of about 1 nm. The calculated transmission for straight [100] and [111] nanowires is shown in Figure 4.6. As in the case of an infinite gold wire (see Section 4.2 the conductance is an integer multiple of G_0, corresponding to the number of open channels. Introducing kinks into the wire causes scattering which decreases the conductance significantly. The conductance values of nanowires with a kink are shown in Table IV.1. Figure 4.7 shows that in the $l = 0.5 \times a$ and $l = 1.5 \times a$ cases the conductance is completely suppressed while in the case of $l = 1.0 \times a$ the conduction is decreased by a factor of 20. The difference in conduction for wires with

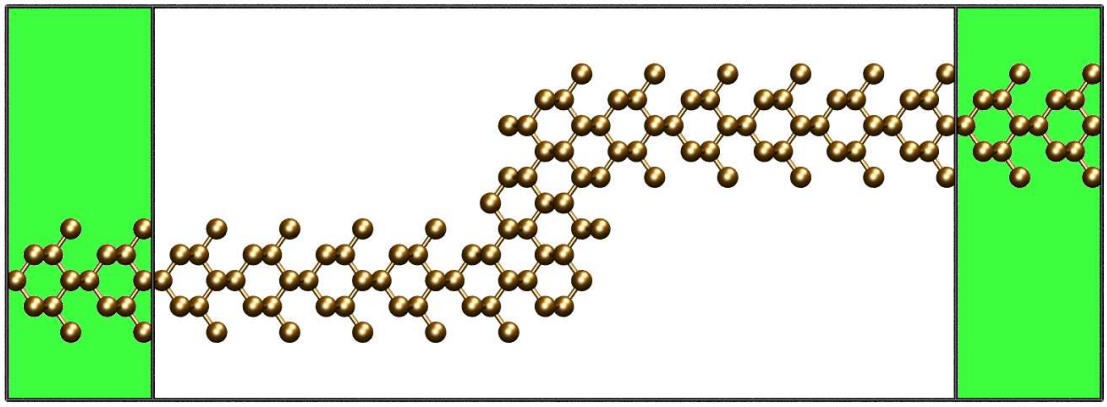

Figure 4.5: A [100] silicon nanowire with a [111] kink. The length of the kink is $0.5a$ along the transport direction. The [100] wire is enclosed by four (100) surfaces. The [111] kink is enclosed by 6 (110) surfaces. The boxes indicate the lead and scattering regions (electrode region highlighted in green).

Table IV.1: Conductance in several Si nanowires. Kinked $L = x$ corresponds to a [100] nanowire with a [111] kink that is x Åalong the [100] axis.

System	$G(G_0)$
Pristine [100]	4.04
Pristine [111]	1.98
Kinked $L = 0.5a$	1.5×10^{-10}
Kinked $L = 1.0a$	7.2×10^{-2}
Kinked $L = 1.5a$	2.6×10^{-7}

different kink lengths is likely due to resonance mechanism similar to the case of the mono-atomic gold step described in Section 4.2.

The last set of examples shows the conductance change in the cases of Si and Al nanowire step structures. The stepped Si nanowires can be constructed by connecting one of the segments shown in Figure 4.5 with its mirror image. The wires point along the [100] direction and have a step with [111] segments for legs. Along the top of the step points along [100]. The stepped Al wires have the same basic structure as the

Table IV.2: Conductance in several nanowires. L_k is the length of the [111] legs of the step along the [100] axis in units of the wire's lattice constant. L_T is the length of the top section of the step in units of the wire's lattice constant. The conductance of the straight Al wire is $7G_0$.

L_k, L_T (SiNW)	$G(G_0)$	L_k, L_T (AlNW)	$G(G_0)$
$0.5, 2.0$	6.3×10^{-3}	$1.5, 4$	0.12
$0.5, 3.0$	2.1×10^{-2}	$0.5, 2$	0.21
$0.5, 4.0$	6.4×10^{-2}	$0.5, 3$	0.27

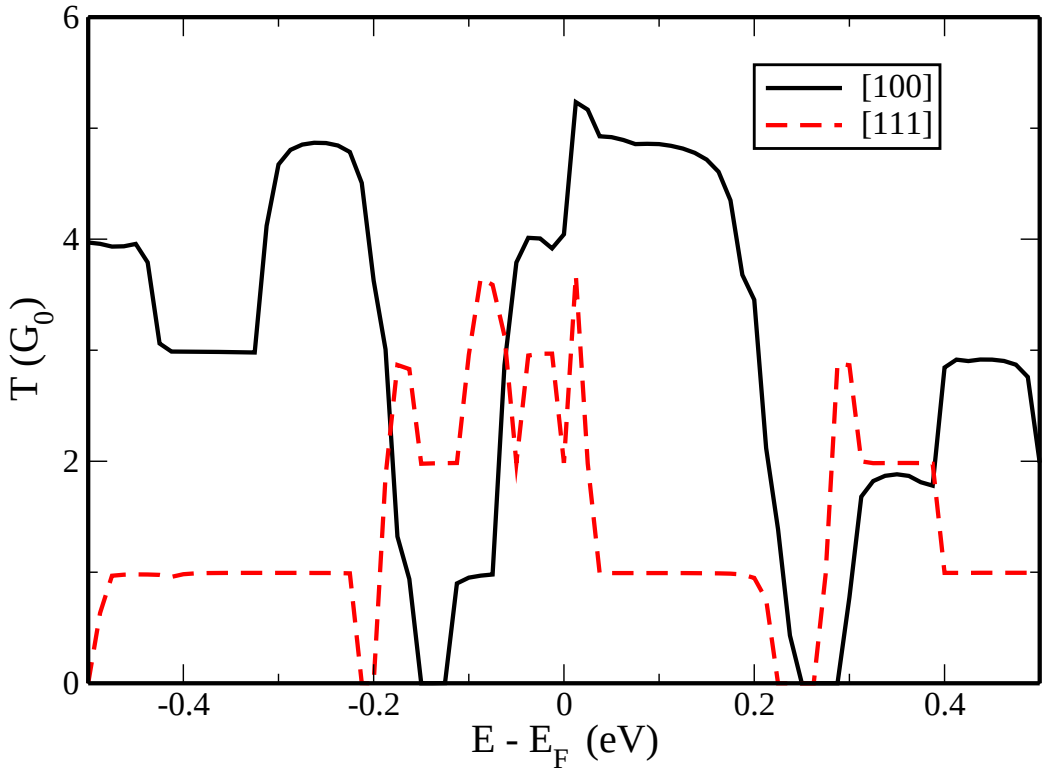

Figure 4.6: Transmission coefficient as a function of energy for [100] and [111] unpassivated Si nanowires.

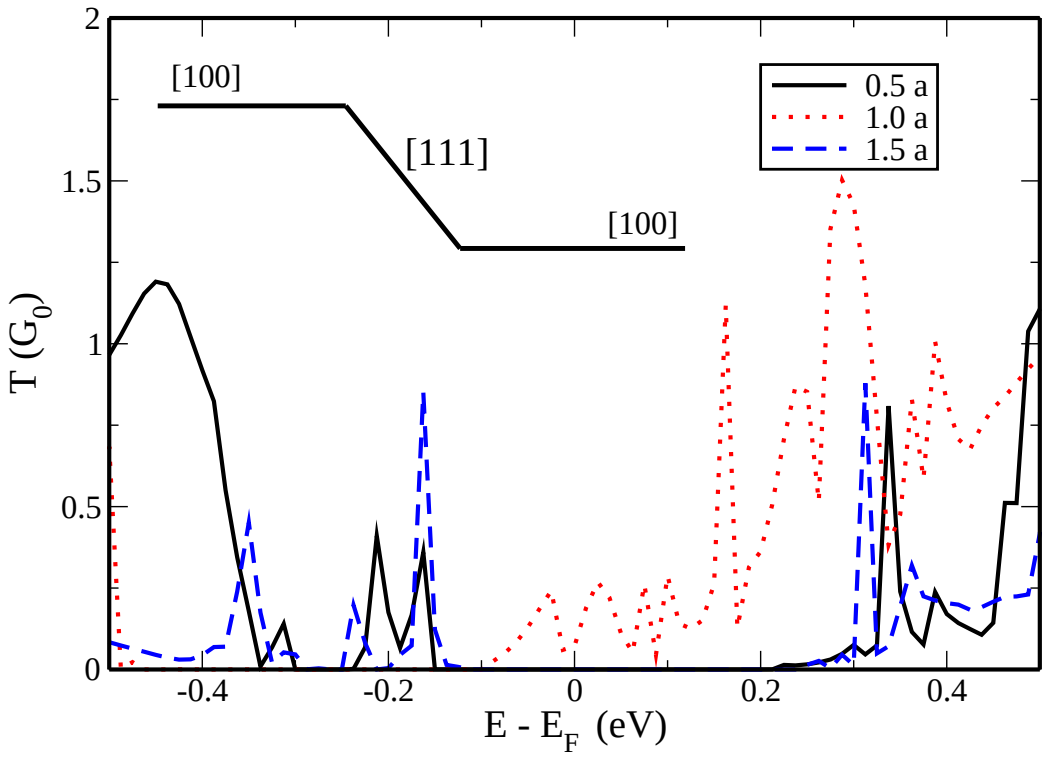

Figure 4.7: Transmission coefficient as a function of energy for kinked SiNWs. The numbered curves to [100] wires with [111] kinks of different lengths. The legend indicates the length of the kinked section where a is the lattice constant of Si.

stepped Si nanowires except they are based on the fcc lattice instead of the diamond lattice. The conductance of the stepped Si nanowire for various geometries is shown in Table IV.2. In each case the conductance is found to be small. The conductance of the stepped Si nanowire is somewhat larger than an individual kink. This shows that quantum states formed in the stepped structure influence the conductance and a stepped structure is not a simple superposition of two kinks. Table IV.2 shows the conductance of the stepped Al nanowire. The conductance of a straight Al nanowire of the same diameter is 7 G_0. The conductance of the stepped Al nanowire is much smaller than that of the straight wire but it is larger than the similar Si nanowire structures.

4.4 Graphene nanoribbons

Graphene is a two-dimensional monolayer of carbon atoms in a honeycomb lattice. Since 2004, when the material was found in a isolated form[149], there has been significant interest in the material[150], especially once the the massless Dirac fermion nature of charge carriers was confirmed by additional experiments[151,152]. Narrow strips of graphene, graphene nanoribbons, are predicted to exhibit electronic properties, such as a band gap, which make them potentially useful components of electronic devices at the nanoscale[110,153–155]. A variety of methods can be used to create narrow strips of graphene: carbon nanotubes can be chemically unzipped[156], standard lithography techniques can be used to obtain ribbons with widths $\sim$ 10nm[157], smaller ribbons can be created with scanning tunneling microscope lithography[114] and small ribbons can be created via chemical self-assembly methods[113]. These narrow strips

of graphene, known as graphene nanoribbons, have been the subject of many studies[110,153–155,158,159].

With the recent development of methods allowing atomically precise fabrication of graphene nanoribbons, the influence of various geometric factors can be studied in a controlled way. When a bottom-up self-assembly technique[113] is used, control can be exerted by modifying the precursor molecules. Thus, exotic shapes with long-range order, such as kinked or bent nanoribbons, can be obtained. Similar results can be achieved with other precision methods[114]. It is possible to have a graphene nanoribbon aligned along a particular lattice direction and at another point change the lattice direction of the wire. In this work these nanoribbons are referred to as bent or kinked, but it should be noted that they are not deformed or strained. Varied configurations of the graphene nanoribbons could be combined to achieve functional circuit components. Understanding the relation between atomic positions and electronic properties is key to the design.

A number of theoretical works have investigated the role of edges in graphene nanoribbons. Yan. Q. et al. have explored the influence of edge doping on current-voltage characteristics[160]. The effect of various terminating edges with different chemical groups was investigated by E. Kan et al.[161]. Few works have focused on the effects edge disorder at the DFT level[162] while many have investigated at the tight-binding level[163,164]. In all these works strong dependence was found on the particulars of the atomic configurations. In other work, quantum interference effects in junctions with multiple electrodes[10] and nanowires with kinks[11] were shown to be important. In this section the role of kinks and extra edge atoms in thin graphene nanoribbons are

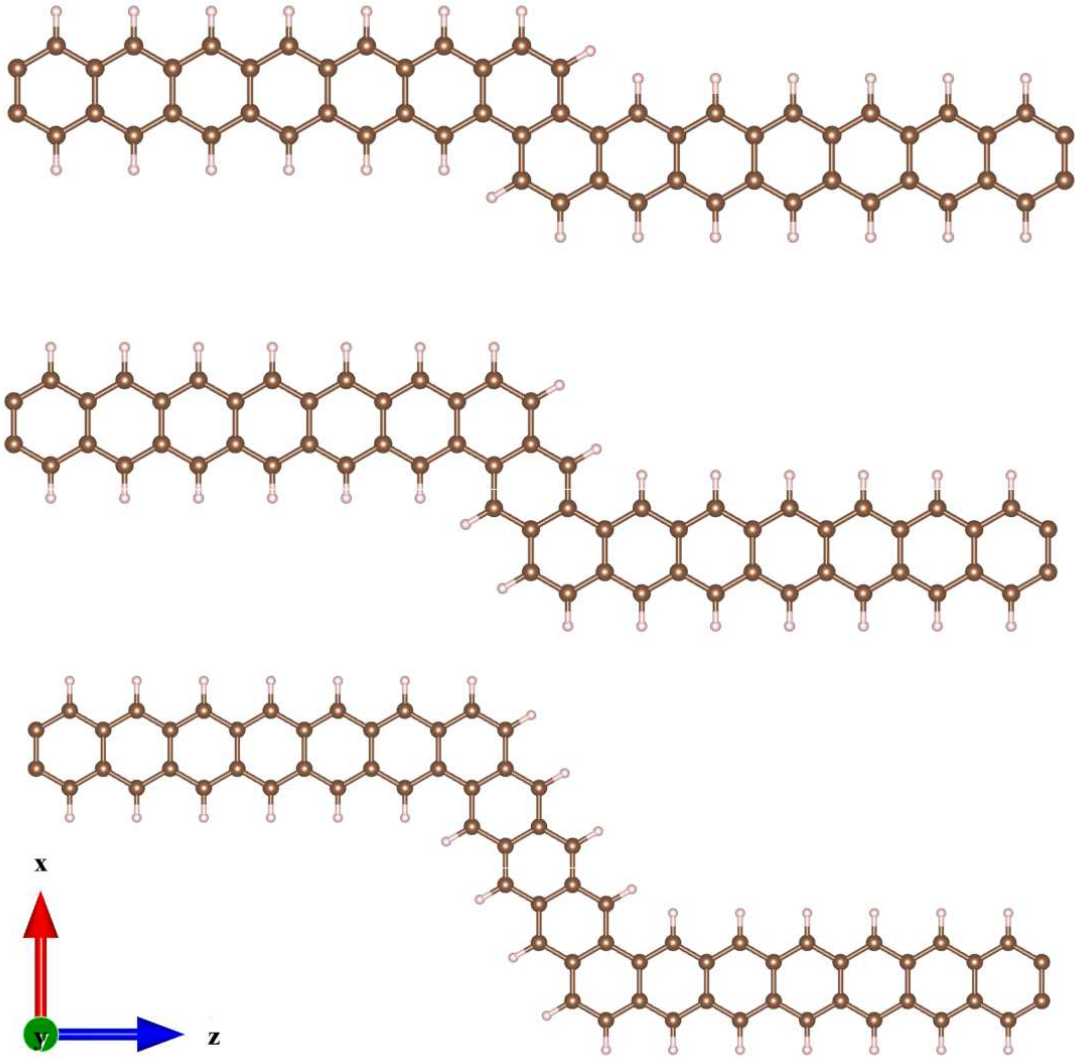

Figure 4.8: Thinnest possible graphene nanoribbons with a kink. From top to bottom there are the cases with two, three and five rings in the kinked section. These correspond to the curves labeled 2,3 and 5 in 4.9.

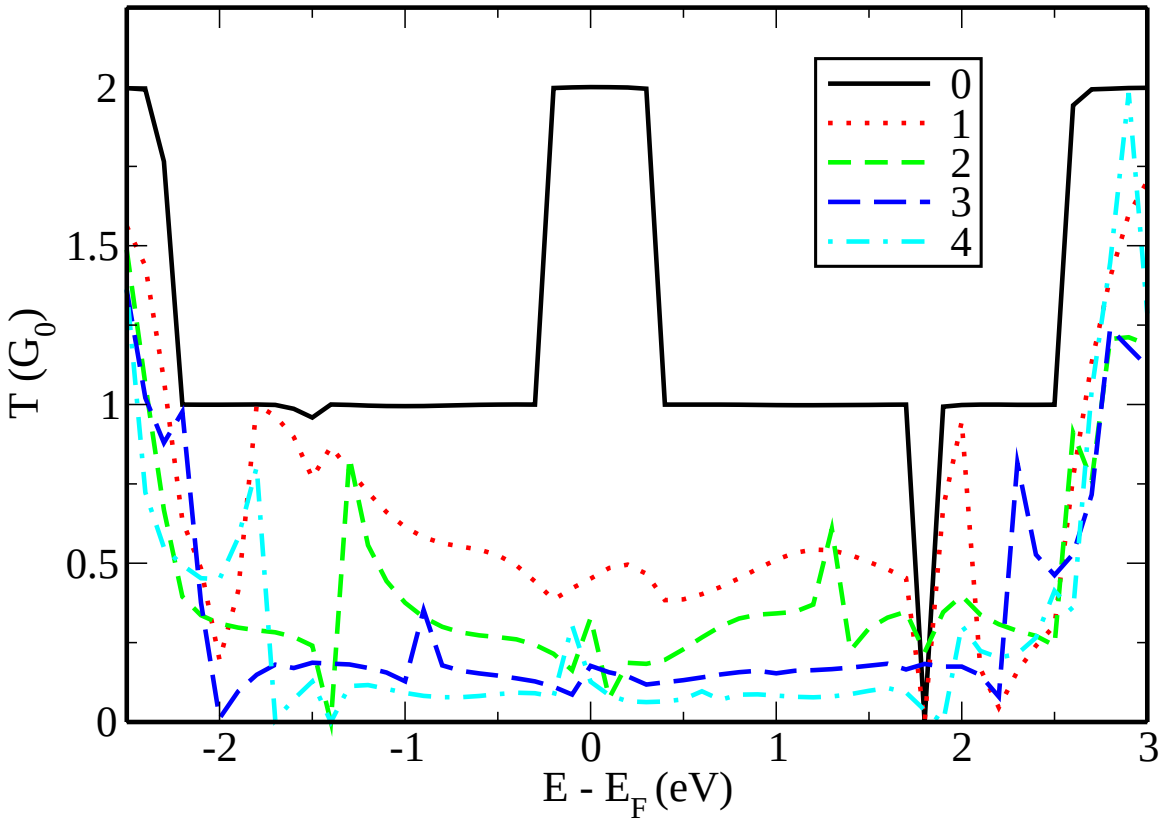

Figure 4.9: Transmission coefficient for kinked graphene nanoribbons as a function of the number of rings in the kinked region (see Fig. 4.8). The solid black line indicates the case of no kink in the ribbon.

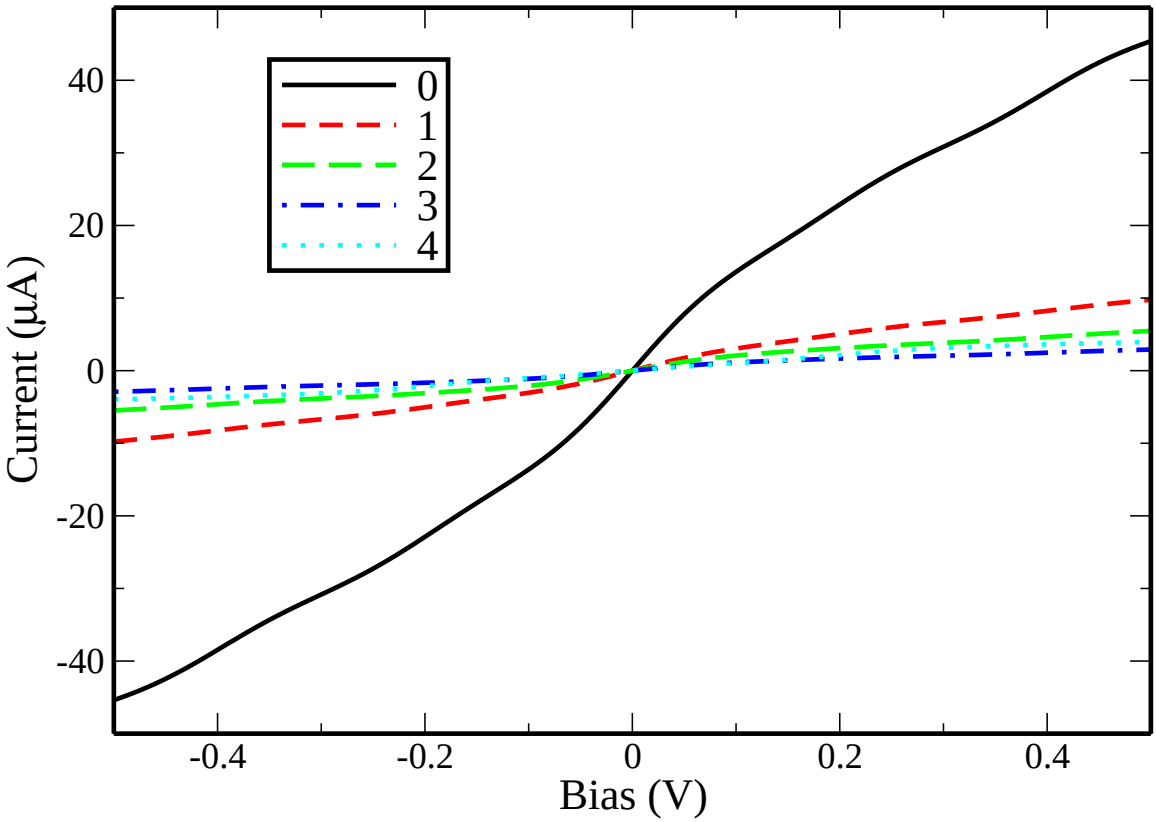

Figure 4.10: Current-voltage response of kinked graphene nanoribbons. The curves correspond to transmission functions shown in figure 4.9.

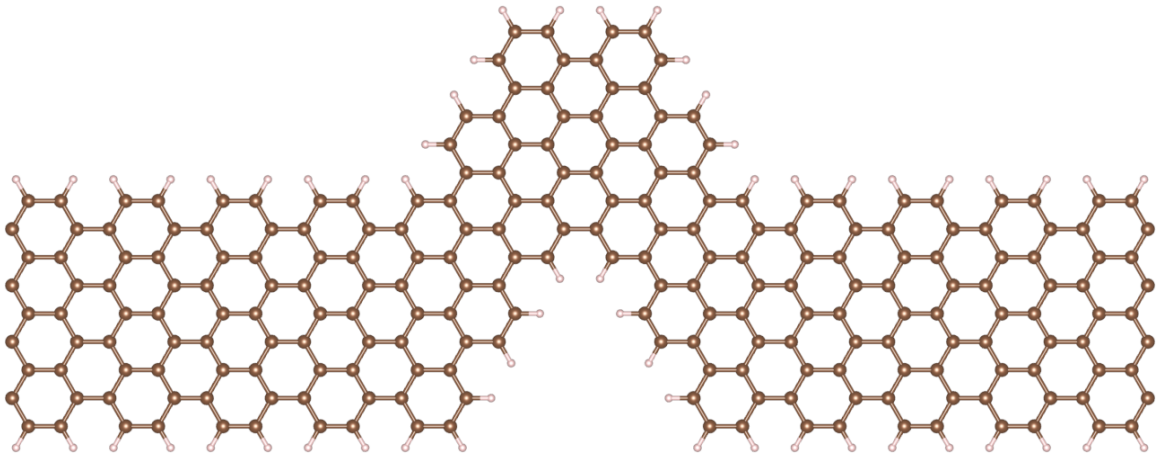

Figure 4.11: Armchair nanoribbon with a chevron shaped kink. The structure corresponds to nanoribbons made in Reference[113].

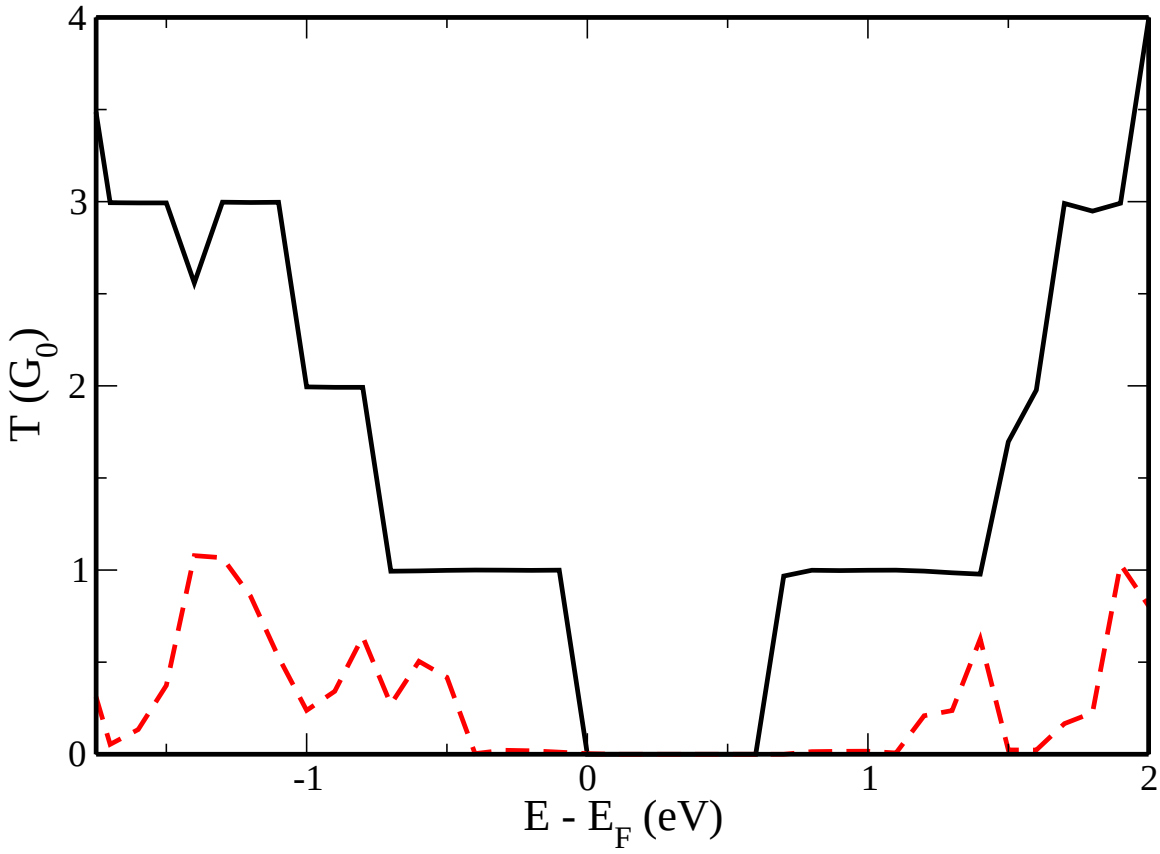

Figure 4.12: Transmission in an armchair ribbon with a chevron shaped kink (see Fig. 4.11). The solid black curve is the conductance of perfect nanoribbon corresponding to the electrode used in the chevron calculation. The dashed red curve corresponds to the graphene nanoribbon with a chevron kink.

investigated.

First, the role of bends or kinks in thin graphene nanoribbons is examined. In scanning electron microscope images of graphene nanoribbons changes in lattice direction within ribbons are clearly visible[114]. The length of these bends is expected to strongly affect the conductance behavior of the graphene nanoribbon in the phase coherent regime. Nanoribbons with varying lengths of kink segment are shown in Figure 4.8, with the middle ribbon representing the simplest planar kinked ribbon with two bends. A lattice constant of $a = 1.42$ Å is used and the distance between C

and H atoms is 1.09 Å. The length of the kink is measured in terms of how many rings are in the kink segment. The conductance as a function of number of atoms in the kink is shown in Figure 4.9. In the ideal case (curve 0) the conductance at the Fermi energy is 2 and is an integer multiple of the quantum of conductance $G_0 = 2e^2/h$ for other energies. Once a bend has been introduced the transmission probability for electrons decreases due to scattering and is no longer an integer multiple of G_0. The conductance decrease is proportional to the length of the kinks. The lowest conductance is about 0.1 G_0, which is about 20 times smaller than the conductance of the straight ribbon. The current-voltage response is shown in Figure 4.10.

Next, the case of a single chevron shape embedded in an armchair graphene nanoribbon (see Figure 4.11) , a geometry seen in recent nanoribbons created via a self-assembly technique[113], is investigated. The transmission as function of electron energy is calculated for the ideal ribbon where the band gap is found to be $E_g \approx 0.5$ eV. When a chevron shaped kink is introduced, the band gap increases to $E_g \approx 1.5$ eV. In the ideal case the conductance is a multiple of the quantum of conductance. The transmission for the ideal case and the chevron kink case are show in Figure 4.12 by the solid black and dashed red curves, respectively. While the chevron section also has armchair edges, the scattering is enough to decrease the transmission.

Another type of defect is the addition of an extra ring of carbon atoms on the edge. This type of edge defect is expected to be common in ribbons fabricated by a number of different techniques, such as chemically unzipped carbon nanotubes. An example of the thinnest possible zigzag graphene nanoribbon with five extra rings on

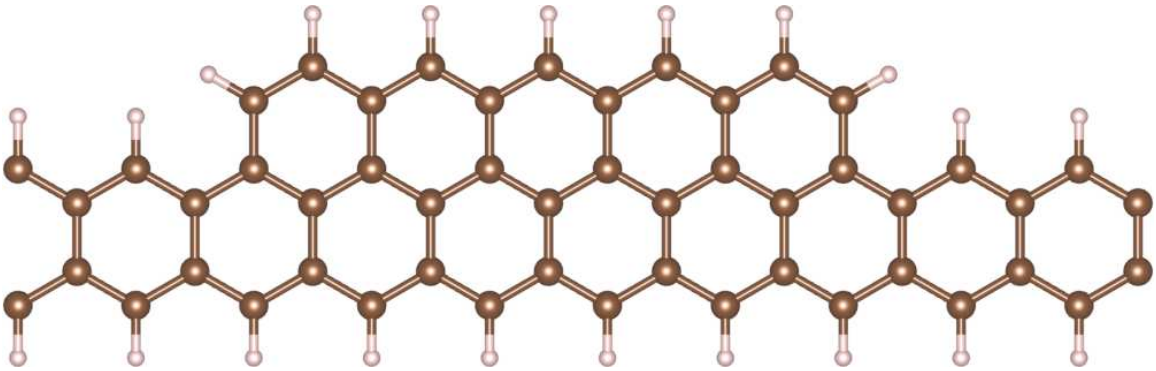

Figure 4.13: A zigzag nanoribbon with extra rings on one edge. The structure shown corresponds to the curve labeled 5 in Fig. 4.14.

one edge is shown in Figure 4.13. The transmission function for different numbers of extra rings is shown in Figure 4.14. In general, extra rings cause a decrease in conductance. When a single extra ring is added, the conductance is suppressed over a wide range of energies, indicating localization of the wavefunction. As the number of extra rings is increased, the decrease is not monotonic; e.g. when the number of extra rings is increased to two the transmission is suppressed, but not to the same extent as in the single ring case. Depending on the energy, different numbers of rings may demonstrate higher conductance.

In summary, the transport properties of graphene nanoribbons with kinks (changes in direction) and with extra rings was investigated. The dependence of conductance on length of the kink section and number of extra rings shows effects of quantum interference and wavefunction localization. Changes in direction were found to cause more significant changes in conductance than addition of extra rings on the edges. The effect of extra rings on the edge was to introduce a scattering center and reduce the number of available conduction channels from two to one. While in the kinked

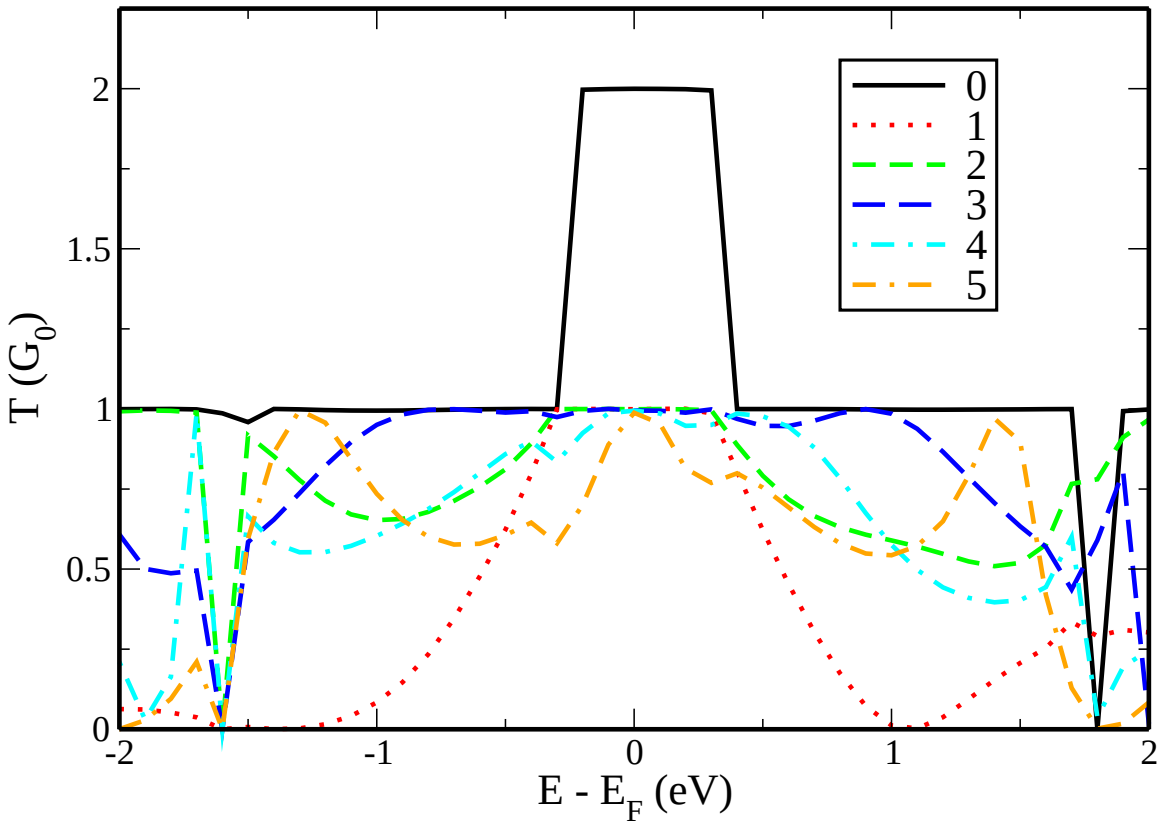

Figure 4.14: Conductance of zigzag graphene nanoribbons with extra rings on one edge. The solid black curve indicates the ideal graphene nanoribbon with no extra rings. The labels indicate the number of consecutive extra rings added to the edge.

ribbon case the induced scattering resulted in non-integer conductance.

4.5 Gold nanowires

In this section junctions created by mechanically deformed metallic nanowires are studied. The connection between structural changes which occur during elongation and resulting material properties is examined in detail with molecular dynamics simulations and first principles calculations of low-bias conductance.

Changes to the crystalline structure, such as slipping or reorientation, have been well characterized[165–168]. Conditions which facilitate the formation of mono-atomic chains have been identified[3,90,167–169]. However, limited attention has been focused on non-crystalline structures which form during the elongation process.

ReaxFF reactive force field is designed to approach the accuracy of quantum mechanical methods with significantly lower computational expense[170]. The force fields are constructed by fitting analytical curves to data from density functional theory calculations[171]. The particular parametrization acceptably reproduces both high and low coordination states. A comparison of energy per particle for different geometries is shown in Figure 4.15. ReaxFF produces more reliable geometries and improved energies compared to tight-binding second moment approximation methods when compared against DFT calculations with the PBE functional[13].

The simulations focus on the elongation of fcc Au nanowires aligned along the $< 100 >$ direction. Nanowires with diameters $D = 1.1, 1.5, 1.9$ nm are elongated at various rates ranging from $0.1 - 5$ m/s. Simulations of low temperature (10K) and room temperature (298K) are shown. The key development is the identification of

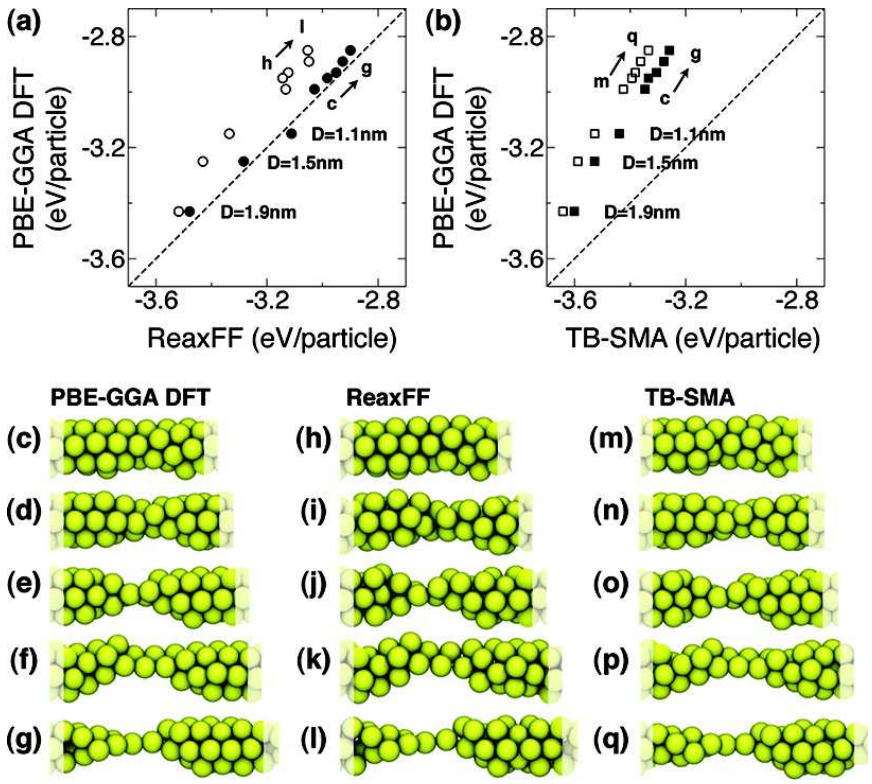

Figure 4.15: a) DFT energy per particle vs ReaxFF energy per particle. b) DFT energy per particle vs TB-SMA energy per particle. Open symbols indicate structures obtained with each method independently and filled symbols indicate geometries taken from DFT calculations. (c-q) snapshots of geometries obtained with each method.

polytetrahedral clusters forming in the neck region of wires as they elongate. As wires are elongated, a region where the wire is thinner forms due to the tensile strain on the wire. In this region, depending on conditions, structures consisting of several tetrahedral subunits are observed. Figure 4.16 illustrates some of the possible structures. The number of structures with different local coordination numbers, determined with the R_{ylm} method based on spherical harmonics, is shown in Figure 4.17. There are two peaks present, at $cn = 6$ and $cn = 8$. A dependence on the diameter of the elongated nanowire is seen where the ratio of $cn = 6$ to $cn = 8$ structures increases

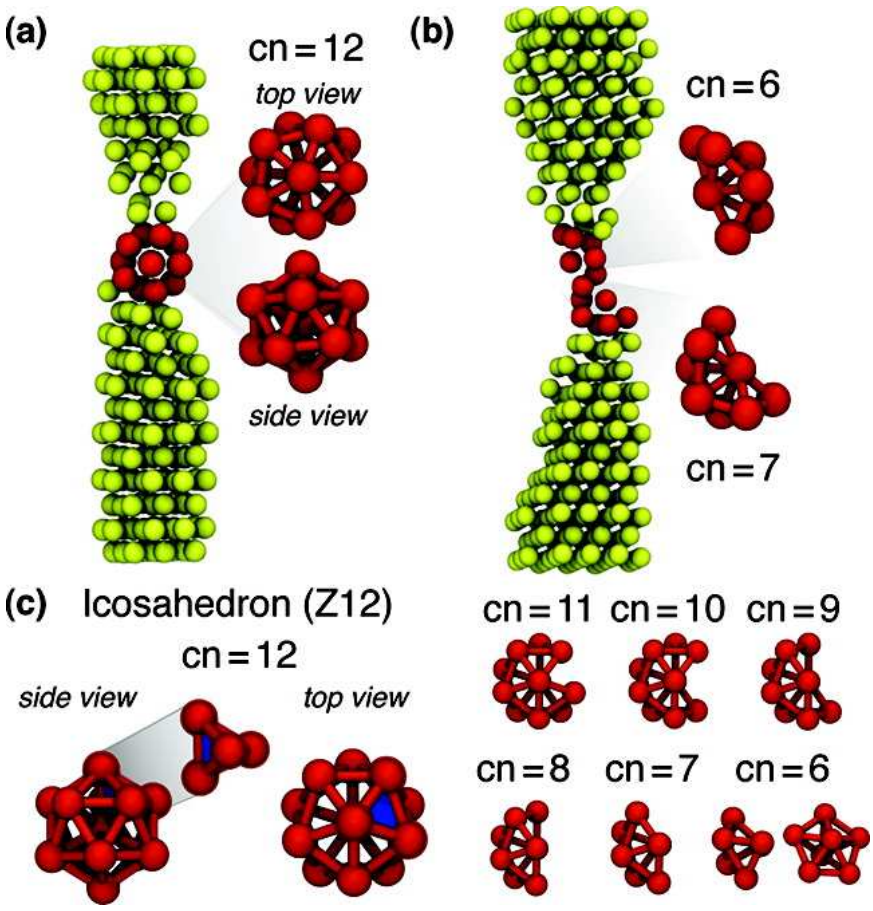

Figure 4.16: Elongated Au nanowire snapshots with polytetrahedron structures. Polytetrahedral structures are highlighted in red. c) Different observed clusters, *cn* is the coordination number of the cluster

as the diameter of the wire is increased.

In mechanical break junctions the conductance is recorded as the wire is stretched. To simulate the conductance trace of a stretched wire snapshots of the elongating wire are saved. The conductance of the saved geometries is then calculated by computing the transmission spectra and taking $G = T(E_F)$. A typical trace shows a series of steps which correspond to changes in the wire geometry as it is stretched. Non-integer values are seen throughout the process, but as the wire cross-section becomes very small, integer values are more common. Gradual changes in the conductance

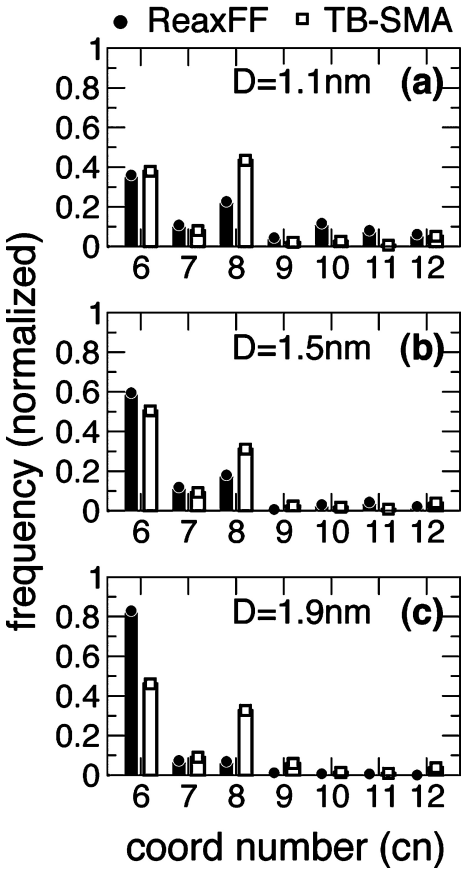

Figure 4.17: Frequency of clusters as a function of coordination number in three Au nanowires. The diameter of the nanowire is a) D=1.1nm b) D=1.5nm and c) D=1.9nm. The simulations are done at 298 K and histograms are taken from simulations with elongation rates ranging from 0.1 to 5 m/s.

traces, as opposed to step-like behavior, are seen to correspond to the formation of polytetrahedra structures in the neck of the wires. This is consistent with recent related work by Tavazza et al[168].

While not the lowest possible energy configurations of few gold atoms, the structures formed in elongated wires play a role in determining the conductance properties of the wires. Further, as the simulations suggest, the increased number of polytetrahedral structures at room temperature highlights the need to consider their effect.

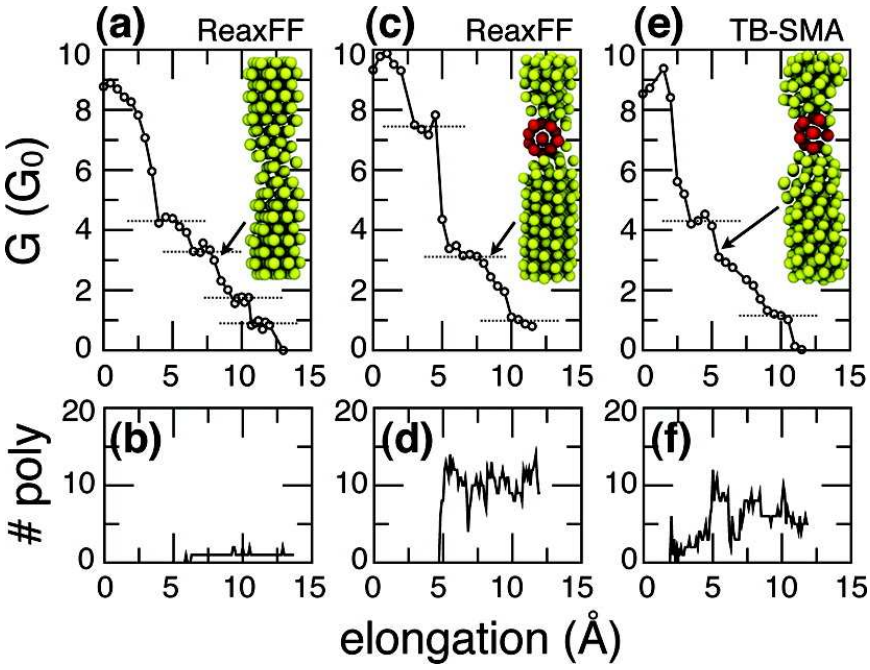

Figure 4.18: Conductance and number of polyhedra as a function of wire elongation. (a-b) correspond to T=298K with the ReaxFF potential, (c-d) correspond to T=10K with the ReaxFF potential and (e-f) correspond to T=10K with the TB-SMA potential. In all cases the wire diameter is 1.1nm and the elongation rate is 1 m/s. The snapshots are taken for geometries with conductance of 3 G_0

4.6 Au-tetraphenyl-porphyrin

Tetraphenyl-porphyrin (TPP) based molecules are established building blocks in nanoscale systems on surfaces[172–174]. The wide use of this molecule is generally due to the structural stability and varied chemistry available because the center of the molecule can hold hydrogen or metal atoms. Due to these factors the self-assembly of many structures is possible; including films[175,176], networks[177,178] and chains[179].

The development of effective nanoscale electronic switches is a major research goal of many groups. Switches operated by light[180], current[181,182] and other means[183–186] have all been demonstrated. Recently, it has been shown that TPP molecules can be used to created four-level conductance switches based on proton transfer[173]. After

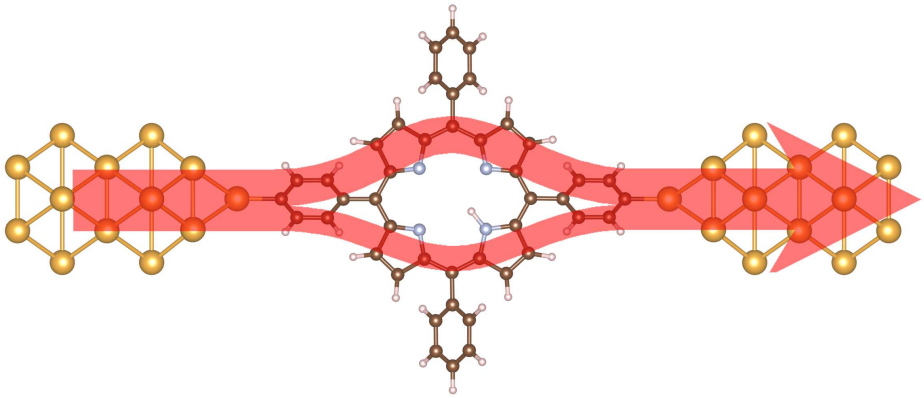

Figure 4.19: 1-H tetraphenyl-porphyrin molecule with gold contacts

deprotonation there is a single hydrogen in the center ring of the molecule. Four distinct conductance levels are observed in STM measurements.

Another common tool for studying molecular electronic characteristics are break junctions. Recently electron transport measurements have been controllably reproduced[187] and others have found clear signatures of quantum interference in conductance measurements[188]. It is natural then to investigate if the switching effect is present in break junctions with TPP molecules and whether effects of quantum interference are visible.

Optimized geometries of individual 0H-TPP, 1H-TPP and 2H-TPP molecules are obtained with supercell calculations using VASP[189]. Using a conjugate gradient method, geometries were optimized until forces were below 0.05 eV/Å. Then molecules were contacted to FCC gold nanowire electrodes as in Figure 4.19. With ends of the electrodes held fixed, atomic coordinates were again optimized with VASP until forces were below 0.05 eV/Å. The local density approximation was used for exchange and correlation and projector augmented waves were used to represent core

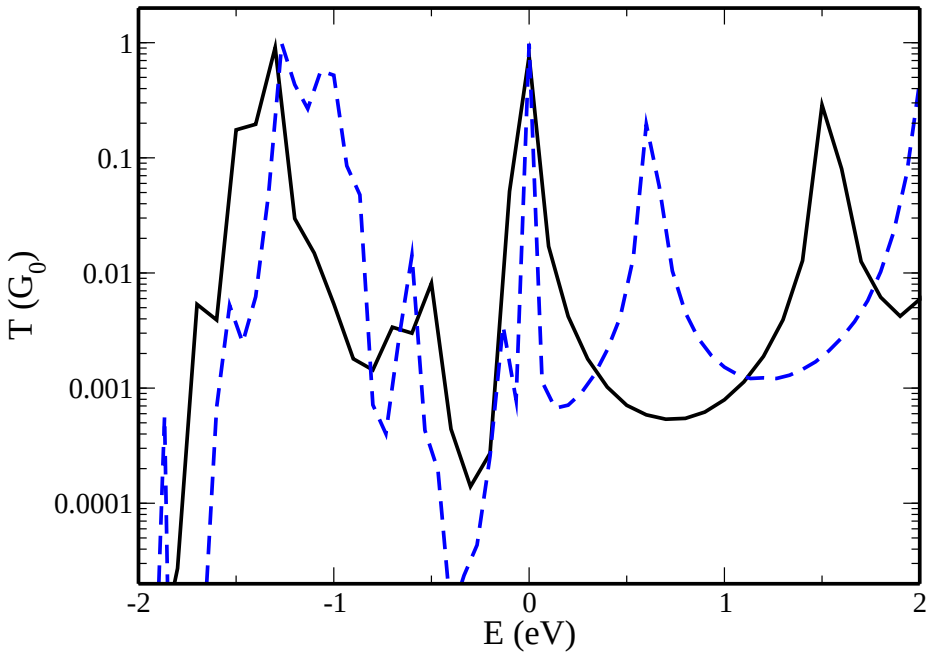

Figure 4.20: Transmission in tetraphenyl-porphyrin molecules between gold electrodes. Transmissions for 1H-TPP molecules are shown by the solid black curve. The four configurations produce identical curves within the resolution of the figure. The dashed blue curve shows the transmission through a 0H-TPP.

electrons. Transport calculations were done at zero-bias with the GPAW code where a double zeta plus polarization (dzp) basis set was used. The transmission curves are shown in Figure 4.20. The black curve represents the calculated transmission of the four possible single hydrogen configurations. No difference is visible in the resolution of the plot. The dashed blue curve shows the case of no hydrogen in the macrocycle of the molecule. These results suggest that molecules with different numbers of hydrogen atoms can be distinguished. However, it also indicates that the difference between proton location is not easily discerned in break junction geometries.

4.7 Summary

In summary, a number of issues related to nanowires have been addressed. The role of kink-like defects in several classes of nanowires was studied. Mono-atomic chains, silicon nanowires and graphene nanoribbons were used as example systems. Generally it is found that the kink geometry strongly influences the electronic properties. In most cases the kink suppresses the conductance and the kinked wires are not good conductors, but certain geometries can induce resonance states and in that case the conductance of the kinked wire remain similar to the conductance if the ideal wire. This indicates that kinks introduced via defects should be carefully monitored when considering device performance and fabrication. Thicker kinked wires are likely to be better conductors as there are many more conduction channels available and the perturbation induced by the kink has less effect. In a possible break junction experiment where a tetraphenyl-porphyrin molecule expected to shown switching behavior no clear evidence of switching was found. Polytetrahedral structures formed in elongated gold nanowires were studied and their influence on conductance and wire formation were elucidated.

CHAPTER V

MULTI-TERMINAL DEVICES

In this chapter applications of the multi-terminal formalism developed in Chapter II are presented. First an overview of current experimental and theoretical efforts relating to multi-terminal devices is presented in section 5.1. Section 5.2 contains the solution to an analytic model system, which is used to demonstrate the accuracy of the method and highlight interesting features of multi-terminal systems. Next, numerical examples with a density functional theory Hamiltonian of a four-terminal graphene device and six terminal carbon nanotube junction are presented. Work shown in this chapter has been published[10].

5.1 Background

Electron transport calculations in two-terminal nanodevices have been rapidly developing ever since the first transport measurements. Due to the simplicity of the formulation, the Non-equilibrium Green's function (NEGF) approach using density functional theory's (DFT) Kohn-Sham Hamiltonian has become a popular approach to calculate transport properties of nanostructures[7,50–59].

It is well known from classical electronic measurements that four-terminal techniques are preferable to two-terminal techniques. The application of four-terminal techniques to nanoscale systems, however, is a difficult task. Scanning tunneling microscopes (STM) with four probes have recently become available[190] (although far

less common than standard STM). These devices allow the desirable four-terminal electronic measurements. For example, a four-probe measurement of a ZnO nanowire allowed characterization of the intrinsic wire properties without contact effects, allowing a clearer understanding of the role of surface defects in ZnO nanowires[191]. Other three- and four-probe measurements with flexible organic transistors[192] and gated molecular junctions[193] have been published. The four-terminal resistance of a nanowire formed in a GaAs/AlGaAs heterostructure was measured[194]. Measurements with two and three terminals have been used to characterize crossed nanotube junctions[195].

Beyond devices with three and four terminals quantum crossbar structures, grids of nanowires, are becoming more common — devices have been demonstrated with a variety of methods and materials. Grids of InAs nanowires on SiO_2 were shown to produce high performance nanoscale transistors[196]. Fabrication of grids with a wide range of metal nanowires (gold, chromium, titanium, niobium, platinum, nickel and aluminum) has been demonstrated[197], with wires as small as 8 nm shown to form large aligned arrays. Later, crossbar devices with individually addressed wires were used to make functional circuits[198]. Crossbar structures have also been created with layer-by-layer deposition of graphene on silicon carbide[199]. Similar to devices based on nanowires, networks of carbon nanotubes attached to nanopillars have been grown[200]. Following in the traditional approach of the semiconductor industry, researchers have focused on increasing the total number of device components and the density of components[201]. These crossbar devices have been analyzed in the context of classical electrical circuits. However, as the relevant device dimensions are decreased, quantum

mechanical effects will play a larger role.

Computational approaches for three-terminal and four-terminal calculations have recently become available[202–212]. The first multi-terminal calculations used tight binding Hamiltonians[202,210–212]. The extension of the Green's function formalism to three and four terminal systems was used to study graphene T (three terminals) and cross (four terminals) junctions[202]. The transport properties are found to depend strongly on the atomic details of the scattering region. Early studies with tight-binding Hamiltonians analyzed three-terminal molecular junctions with benzene molecules and proposed their use as quantum interference based transistors[211,212]. The scattering matrix formalism was also extended for structures with three and four terminals where it was used to show the unique spin transport properties in these systems[210]. However, the method was only presented for two-dimensional devices.

Few first-principles calculations exist[204,208]. These calculations use the NEGF formalism extended to the three- and four-terminal cases. An implementation of the NEGF formalism for four terminals with a DFT Hamiltonian, with particular attention to the application of finite bias voltages, was described by Saha et al.[204]; the primary focus was the demonstration of the method and they described examples of a radialene molecule contacted to carbon chains and two crossed carbon chains with varying separation. In the following year the same group went on to investigate an organic molecule contacted to four gold nanowires[208]. It was found that a 9,10-Bis((2′-para-mercaptophenyl)-ethinyl)-anthracene molecule contacted to the gold nanowires via thiol groups exhibited large negative differential resistance and other non-linear effects in current-voltage response.

The extension of the NEGF formalism to four-terminal devices is straightforward but tedious. In the case of the two-terminal NEGF, the Hamiltonian of the system is infinite dimensional, but it has a block tridiagonal matrix structure which allows for efficient evaluation of the Green's function for each energy point. In the four-terminal case the structure of the Hamiltonian matrix is more complicated[204], and while the matrix is still sparse with nonzero block matrices, the calculation of its inverse is more difficult. The extension to more than four terminals is possible but the calculation becomes even more complex.

A complex potential quantum transport framework was recently developed[10,48,213]. In this approach complex absorbing potentials (CAPs) are added to the Hamiltonian in the leads and transform the infinite open system into a finite closed system by effectively cutting the leads off at a finite distance from the central region. Excellent agreement with non-equilibrium Green's function calculations was found[48]. However, much less computational effort was required because the evaluation of Green's functions for the leads is avoided in the CAP formalism. In the multi-terminal case, a CAP is added to the Hamiltonian of each lead and the transmission coefficients are calculated by using a transmission formula that is generalized for the multi-terminal case. The main advantage of the approach, as in the two-terminal case, is that one can deal with finite dimensional matrices instead of infinite dimensional ones. Another advantage is the simplicity of the implementation, which allows the approach to be easily extended for N-terminal junctions. Details of the formalism and the extension to the general case of N terminals are presented in Chapter II and are published in Reference[10].

5.2 Analytic model

In this section an analytically solvable model system is used to show the accuracy of the multi-terminal transport formalism developed in Chapter II. The model is based on a tight-binding Hamiltonian and the analytic solution is given in detail for the case of 4 electrodes. Then 4 and 8 terminal systems will be discussed with numerical examples. The accuracy of the method and some interesting features of multi-terminal systems are highlighted.

The tight-binding Hamiltonian with first nearest-neighbor interaction is

$$H_{\mathrm{TB}} = \sum_i \epsilon_i |i\rangle\langle i| - t \sum_i \left(|i\rangle\langle i+1| + |i+1\rangle\langle i| \right). \tag{5.1}$$

The system consists of five regions: four leads and a central scattering region. Assuming that leads only interact with the center region the Hamiltonian of the device is

$$\boldsymbol{H} = \begin{pmatrix} H_1 & 0 & 0 & 0 & \tau_1^+ \\ 0 & H_2 & 0 & 0 & \tau_2^+ \\ 0 & 0 & H_3 & 0 & \tau_3^+ \\ 0 & 0 & 0 & H_4 & \tau_4^+ \\ \tau_1 & \tau_2 & \tau_3 & \tau_4 & H_C \end{pmatrix}, \tag{5.2}$$

where H_i is the Hamiltonian of lead i ($i \in \{1,2,3,4\}$) and τ_i is the Hamiltonian matrix that couples lead i to the central region C. Lead i is kept at a potential $\boldsymbol{V}_i$. Considering on-site elements $2t$, and connecting elements $-t$, the Hamilontian of the

central region is

$$H_C = \begin{pmatrix} 2t+V_1 & 0 & 0 & 0 & -t \\ 0 & 2t+V_2 & 0 & 0 & -t \\ 0 & 0 & 2t+V_3 & 0 & -t \\ 0 & 0 & 0 & 2t+V_4 & -t \\ -t & -t & -t & -t & 4t+V_C \end{pmatrix}. \tag{5.3}$$

The Hamiltonian of the lead i is an infinite tridiagonal matrix,

$$H_i = \begin{pmatrix} 2t+V_i & -t & 0 & 0 \\ -t & 2t+V_i & -t & 0 \\ 0 & -t & 2t+V_i & \dots \\ 0 & 0 & \dots & \dots \end{pmatrix}. \tag{5.4}$$

The connection matrices, τ_i, have one non-zero element, $-t$, located in the final column of row i. For example:

$$\tau_3 = \begin{pmatrix} \dots & 0 & 0 \\ \dots & 0 & 0 \\ \dots & 0 & -t \\ \dots & 0 & 0 \\ \dots & 0 & 0 \end{pmatrix} \tag{5.5}$$

The self-energy of a lead i is

$$\Sigma_i = \tau_i g_i \tau_i^+. \tag{5.6}$$

The Green's function of the lead is

$$g_i = \frac{E - V_i}{2t^2} - \frac{i}{2}\sqrt{1 - \frac{(E - V_i - 2t^2)^2}{4t^2}} = \frac{e^{-i\phi_i}}{t} \tag{5.7}$$

where

$$\phi_i = \arccos\left(\frac{E - V_i - 2t}{2t}\right). \tag{5.8}$$

With these definitions the self-energy matrices, Σ_i are 5×5 and contain only one non-zero element $te^{-i\phi_i}$ located on the diagonal at (i, i). For example,

$$\Sigma_2 = \begin{pmatrix} 0 & 0 & 0 & 0 & 0 \\ 0 & te^{-i\phi_2} & 0 & 0 & 0 \\ 0 & 0 & 0 & 0 & 0 \\ 0 & 0 & 0 & 0 & 0 \\ 0 & 0 & 0 & 0 & 0 \end{pmatrix}. \tag{5.9}$$

The Green's function for the central region is

$$G_C(E) = \frac{1}{E - H_C - \Sigma_1 - \Sigma_2 - \Sigma_3 - \Sigma_4}. \tag{5.10}$$

With these definitions the Green's function is

$$G_C(E) = \begin{pmatrix} a_1 & 0 & 0 & 0 & -t \\ 0 & a_2 & 0 & 0 & -t \\ 0 & 0 & a_3 & 0 & -t \\ 0 & 0 & 0 & a_4 & -t \\ -t & -t & -t & -t & E - 4t - V_C \end{pmatrix}^{-1}, \tag{5.11}$$

where $a_i = E - 2t - V_i - te^{-t\phi_i}$. The Green's function can be written in the following block form

$$G_C = \begin{pmatrix} A & T^+ \\ T & B \end{pmatrix}^{-1} \tag{5.12}$$

where

$$A = \begin{pmatrix} a_1 & 0 & 0 & 0 \\ 0 & a_2 & 0 & 0 \\ 0 & 0 & a_3 & 0 \\ 0 & 0 & 0 & a_4 \end{pmatrix}, \tag{5.13}$$

$$T = -\begin{pmatrix} t & t & t & t \end{pmatrix} \quad \text{and} \quad B = (E - 4t - V_C)\,. \tag{5.14}$$

The inverse of block matrix can be found by partitioning[62] (see also Eq. 2.63)

$$G_C = \begin{pmatrix} A^{-1} + A^{-1}T^+STA^{-1} & -A^{-1}T^+S \\ -STA^{-1} & S \end{pmatrix} \tag{5.15}$$

where S is the inverse of the Schur compliment of A,

$$S = (B - TA^{-1}T^{+})^{-1}. \tag{5.16}$$

Since A is diagonal

$$A^{-1} = \begin{pmatrix} f_1 & 0 & 0 & 0 \\ 0 & f_2 & 0 & 0 \\ 0 & 0 & f_3 & 0 \\ 0 & 0 & 0 & f_4 \end{pmatrix} \tag{5.17}$$

where $f_i = a_i^{-1}$. With the previous definitions

$$S = \left[E - 4t - V_C - t^2 \sum_{i=1}^{n=4} f_i \right]^{-1}. \tag{5.18}$$

From this point forward S will be referred to as s to reflect the fact that it is a scalar.

The elements of the Green's function can now be explicitly calculated,

$$G_C = \begin{pmatrix} d_1 & F_{12} & F_{13} & F_{14} & stf_1 \\ F_{21} & d_2 & F_{23} & F_{24} & stf_2 \\ F_{31} & F_{32} & d_3 & F_{34} & stf_3 \\ F_{41} & F_{42} & F_{43} & d_4 & stf_4 \\ stf_1 & stf_2 & stf_3 & stf_4 & s \end{pmatrix} \tag{5.19}$$

where $d_i = f_i + st^2 f_i^2$ and $F_{ij} = st^2 f_i f_j$. The expression for the transmission between

two leads is

$$T_{ij} = \mathrm{Tr}\left[\Gamma_i G_C^+ \Gamma_j G_C\right] \tag{5.20}$$

where

$$\Gamma_i = i\left[\Sigma_i - \Sigma_i^+\right]. \tag{5.21}$$

The structure of Γ_i is sparse with only one non-zero element, $r_i = -2t\sin\phi_i$, located at (i,i). Now consider $\Gamma_j G$; The effect of multiplying by Γ_j is to pick out row j from G. For example,

$$\Gamma_2 G^+ = \begin{pmatrix} 0 & \dots & 0 \\ r_2 G_{21}^+ & \dots & r_2 G_{25}^+ \\ 0 & \dots & 0 \\ \vdots & & \vdots \\ 0 & \dots & 0 \end{pmatrix}. \tag{5.22}$$

Multiplying the terms and taking the trace gives

$$T_{ij} = 4t^2 \sin\phi_i \sin\phi_j \left|F_{ij}\right|^2 \tag{5.23}$$

for $i \neq j$. Note that this expression is general and holds for any number of leads.

5.2.1 Four-terminal junction

As a first example the transmission in the four-terminal device shown in Fig. 5.1 is calculated. The system is described by a tight binding Hamiltonian, discussed previously. The Hamiltonian of the leads is defined in Eq. (5.4) with $V_i = 0$ and

Table V.1: Transmission in four-terminal junctions. The energy is in atomic units.

E	CAP	Analytical
0.0	0.000465	0.000096
0.1	0.110523	0.109824
0.2	0.151629	0.151405
0.3	0.173274	0.173261
0.4	0.186677	0.186729
0.5	0.195814	0.195856
1.0	0.216982	0.216996
1.5	0.225005	0.225001
2.0	0.229159	0.229155

$t = 50$ (in atomic units). The Hamiltonian of the central region is defined in Eq. (5.3) with $t = 50$ and $V_C = 10$ (in atomic units). This value for t corresponds to the values obtained with a three point finite difference discretization with a step size of 0.1 atomic unit. The transmission coefficient calculated by using the CAP is compared to the analytical solution in Table V.1 and in Fig. 5.2. Due to the symmetry of the Hamiltonian in this model, the transmission between any two leads is identical. Table I shows that the results of the CAP calculation are in excellent agreement with the analytical calculations. The agreement improves as the energy increases, because the CAP can more easily absorb the higher energy wave functions. The accuracy can be increased further by increasing the range of the CAP. Fig. 5.2 shows that the transmission monotonically increases with energy. This is similar to the behavior of the transmission probability of a one-dimensional step barrier, where the transmission converges to 1 with increasing energy. In the four terminal case the transmission converges to 1/4.

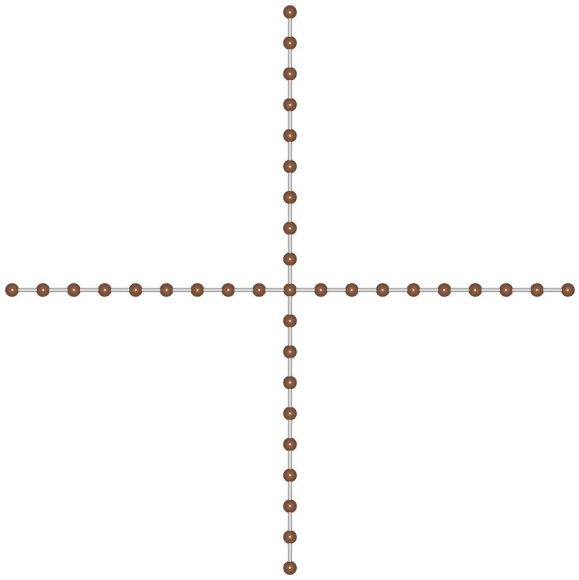

Figure 5.1: 4-terminal junction.

5.2.2 Eight-terminal junction

The next analytically solvable example is the eight-terminal junction shown in Figure 5.3. The crossing points A, B, C, and D are separated by 21 sites. The same Hamiltonian is used as in the previous 4-terminal example, except that $V_C = 0$ is used in the present case. Thus the scattering in the 8-terminal junction is purely due to the cross points. In the 8-terminal example there are three different transmission coefficients T_{12}, T_{14} and T_{15} (connecting lead 1 to leads 2, 4, and 5; see Figure 5.3); all other transmissions are equal to these three due to the symmetry of the Hamiltonian. Figure5.4 shows the transmission coefficients calculated by using the CAP and by the analytical solution. The results of the CAP and analytical approaches are in perfect agreement.

The top graph of Figure 5.4 shows the transmission between leads 1 and 2, T_{12}. This transmission is much larger than the other two transmissions T_{14} and T_{15} (see

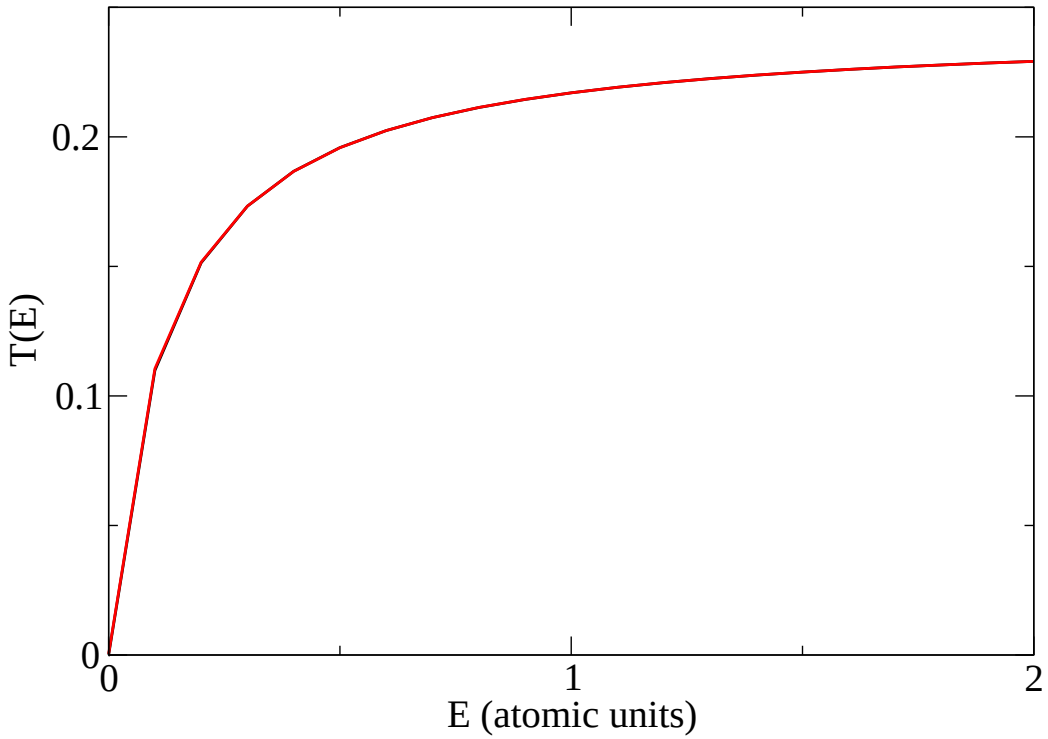

Figure 5.2: Transmission in a 4-terminal junction. The results of the CAP and the analytical calculation are in complete agreement and cannot be distinguished in the resolution of the figure.

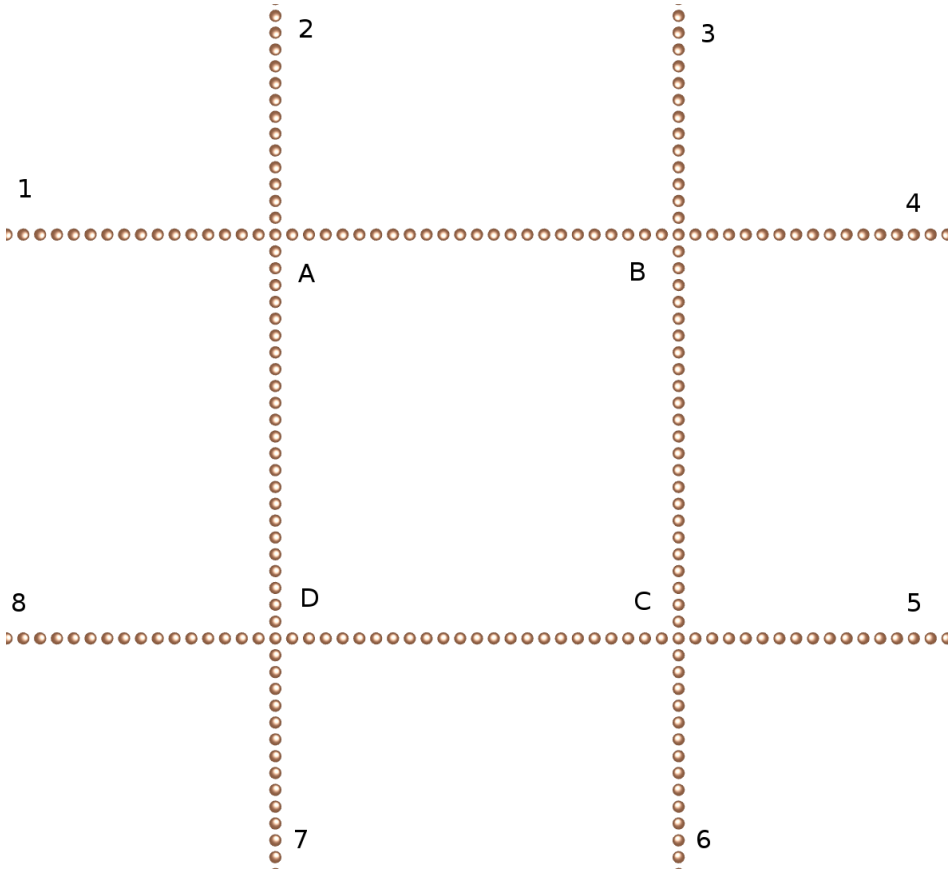

Figure 5.3: 8-terminal junction.

Figure 5.4). This is not surprising, because these two leads are directly connected and there is only one scattering center between the two leads. The transmission oscillates around 5/16 with an amplitude of 4/16. This oscillation is due to the interference between the waves that directly scatter from 1 to 2 and those that go around the square and get backscattered from the vertices A, B, C, and D. The frequency of the oscillation increases with the distance between crossing points because the energy spacing of the standing waves between crossing points decreases and more and more standing waves contribute to the interference.

The bottom graph of Figure 5.4 shows the transmission coefficients T_{14} and T_{15}.

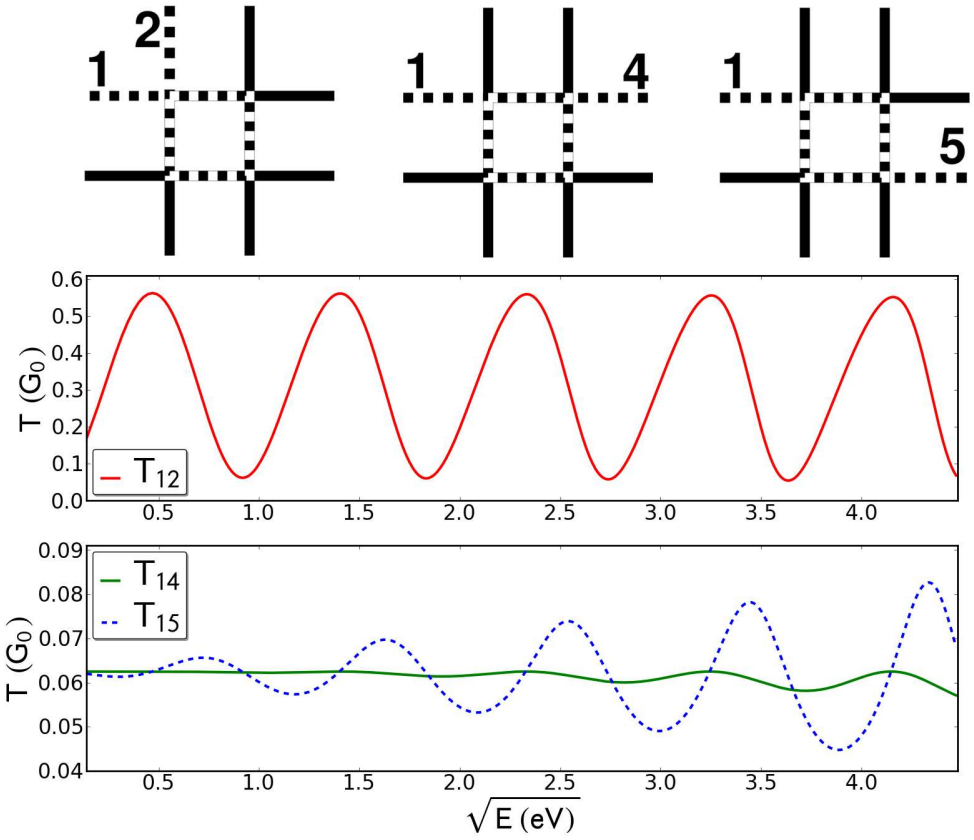

Figure 5.4: Transmission in a 8-terminal junction. The paths of electrons between terminals is shown in the top panel. The results of the CAP and the analytical calculation is in complete agreement and cannot be distinguished in the resolution of the figure.

These transmissions behave similarly to T_{12}, oscillating around 1/16. The interference effect causes a very interesting behavior: in certain energy regions the transmission from $1-5$ is larger than the transmission from $1-4$, which is along a straight line. The period of oscillations, similar to the previous case, depends on the distance between the crossing points.

5.3 Numerical Examples

5.3.1 Four-terminal graphene device

The first realistic example is a four-terminal graphene cross junction. A cross junction consists of an intersection between armchair and zigzag graphene ribbons. The geometry of the device is shown in Figure 5.5. The region within the dotted box is the scattering region of the device. The armchair leads are $n_a = 8$ unit cells wide and the zigzag leads are $n_z = 6$ unit cells in width. Matrix elements are calculated with density functional theory using an atomic orbital basis set.

In contrast to the simple devices discussed previously, with the graphene device there are more unique values for the transmission coefficients between leads. This is caused by the broken symmetry of the system at the corners of the cross region. However, the differences between the different values for turning a corner are small and similar behavior is observed. The calculated transmission is shown in Figures 5.6. Results are in agreement with the results of tight-binding calculations[202]. It is interesting to note that there is no gap for transmission between the two armchair leads, but there is a gap for transmission between the two zigzag leads. A similar gap

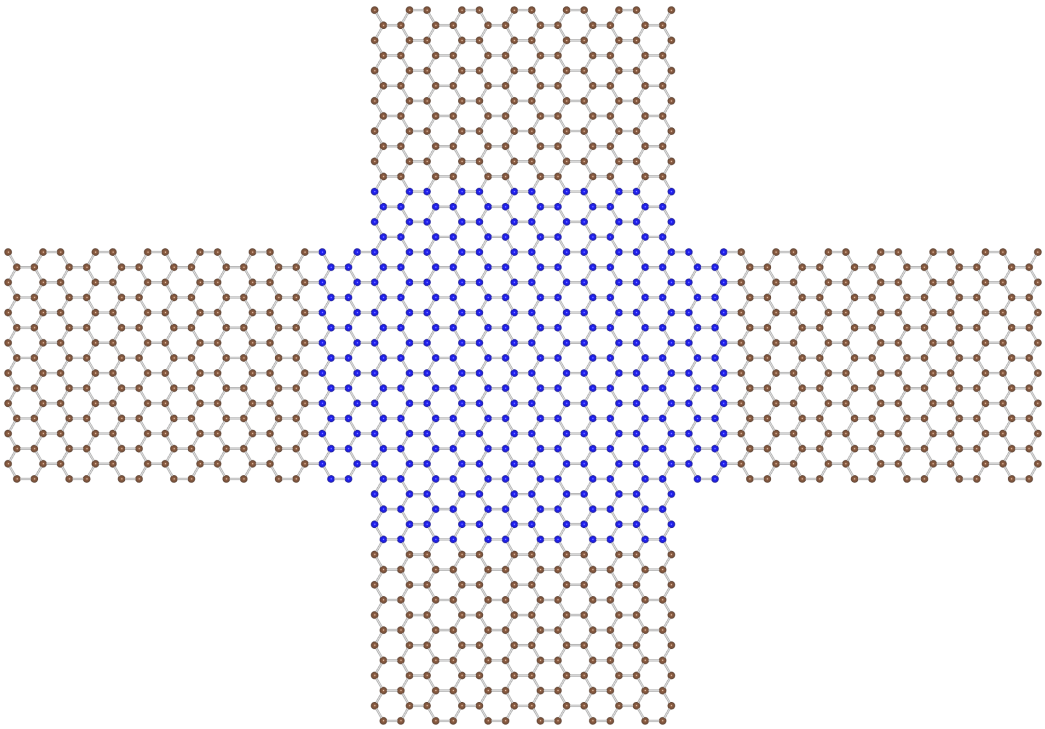

Figure 5.5: Graphene cross-junction device. Atoms in the scattering region are highlighted in blue.

is found for the transmission between the two types of leads.

5.3.2 Six-terminal carbon nanotube junction

The final example is a six-terminal junction built from three $(5, 0)$ semiconducting nanotubes. Two tubes are placed parallel to each other. The third tube, oriented perpendicular to the other two, is placed on top as shown in Figure 5.7. Ideal structures for the nanotubes are used.

The transmission coefficients as a function of energy are shown in Figures 5.8 and 5.9. Similar to the graphene case, the symmetry of the system is broken by the relative orientations of the nanotubes. That is, T_{24} is not the same as T_{35}. However, the two curves have similar features. Since the nanotubes in this configuration are

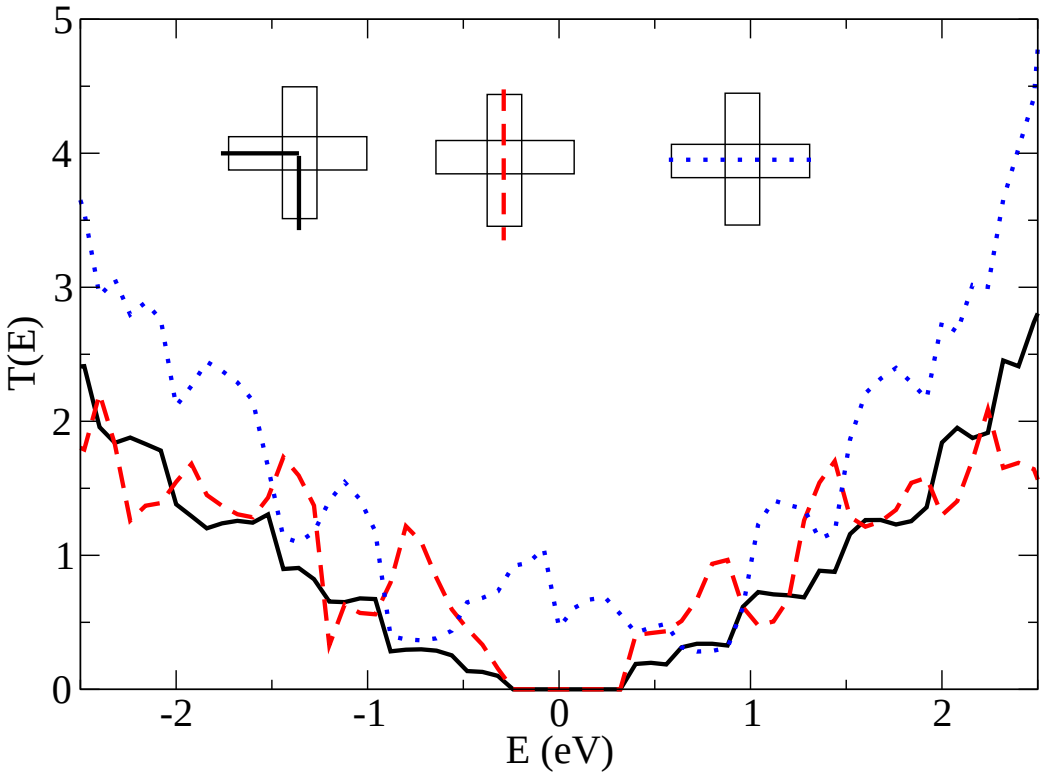

Figure 5.6: Transmission coefficient in a graphene cross-junction device.

loosely coupled, the transmission along the axis of any given nanotube is very similar to that through an isolated nanotube. Figure 5.8 shows that T_{23} and T_{16} both retain their semiconducting gap. The transmission along the two tubes is however not the same because one has two scattering centers and the other only has one. Due to the weak nature of the coupling the transmission through leads on different tubes is significantly lower (see Figure 5.8). The lowest transmission is seen to be from terminals 2 to 4 where the electron would have to go through all three tubes.

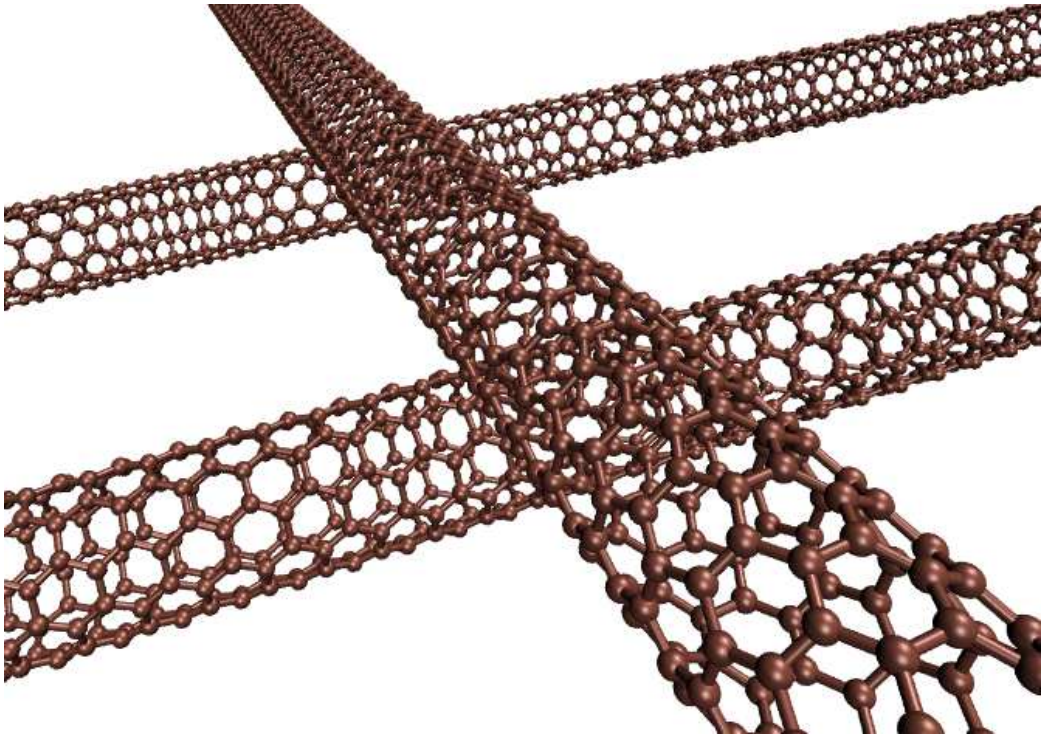

Figure 5.7: 6 terminal CNT junction.

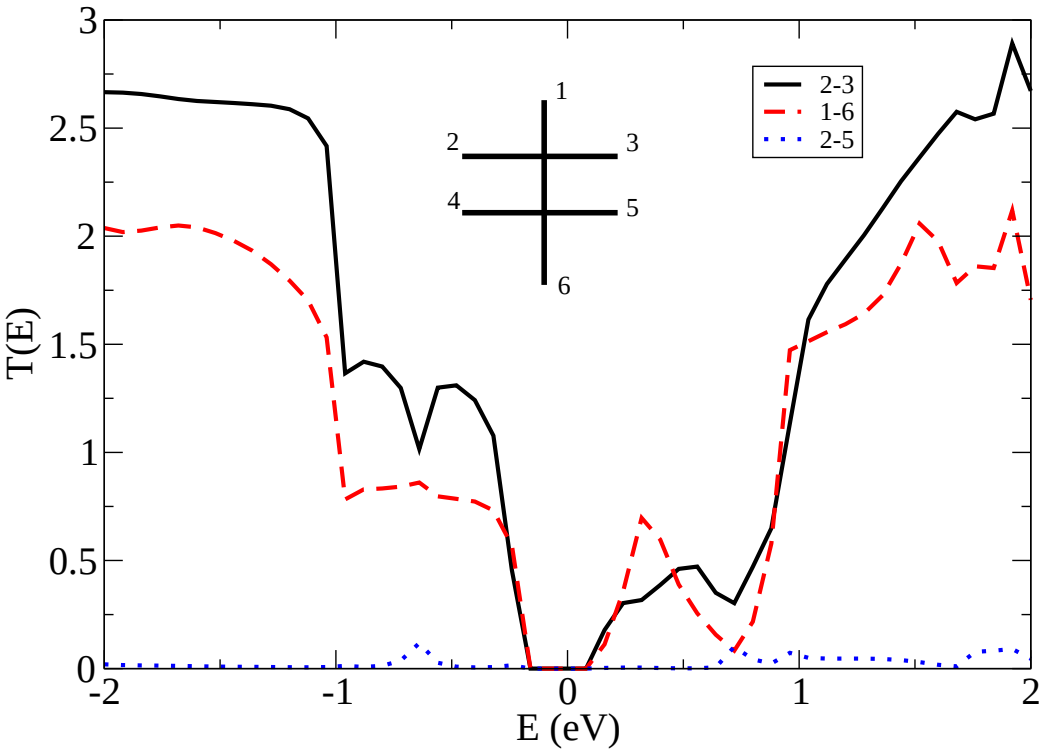

Figure 5.8: Transmission in a 6 terminal CNT junction.

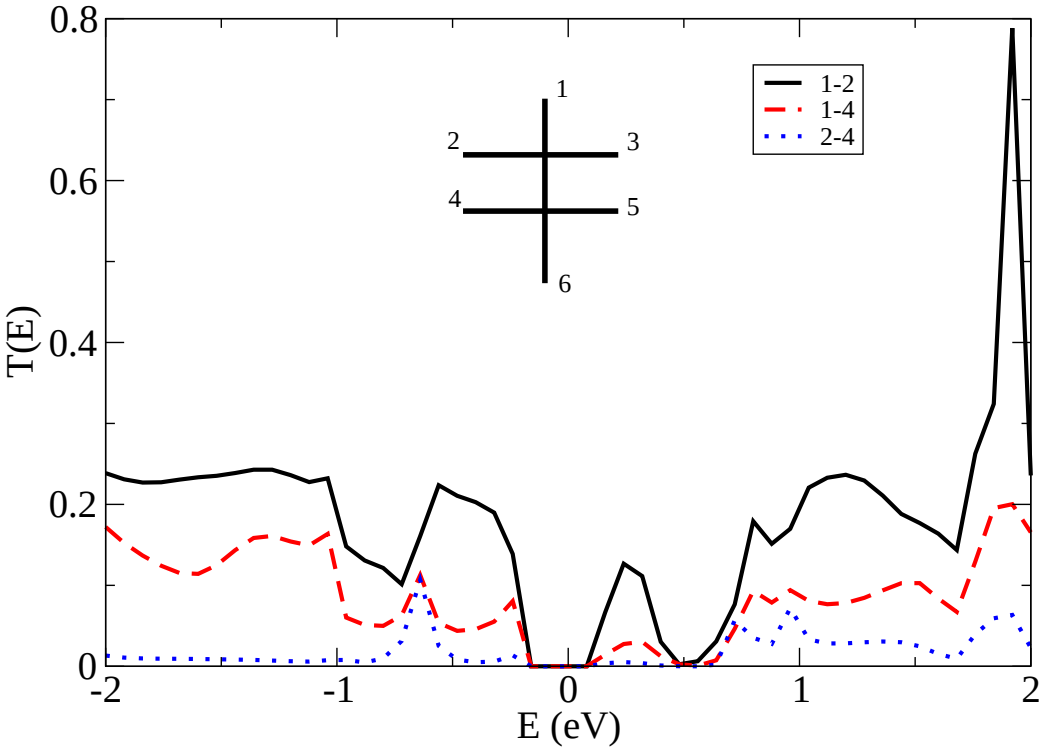

Figure 5.9: Transmission in a 6 terminal CNT junction.

5.4 Summary

In this chapter the accuracy of the complex absorbing potential approach to first-principles transport calculations was demonstrated along with evidence for quantum effects in multi-terminal junctions. First, background information related to multi-terminal calculations and nanoscale experiments was given. Second, a simple tight-binding Hamiltonian model was solved analytically. The analytical results, non-equilibrium Green's function calculation and complex absorbing potential calculation were in complete agreement. Then examples with 4 and 8 terminals were calculated with the tight-binding Hamiltonian. Unique effects of quantum interference were found in this system. The probability of electron transmission to a given electrode was found to depend on the energy of the electron. A 4-terminal graphene junction

and a 6-terminal carbon nanotube junction were examined with a Kohn-Sham density functional theory Hamiltonian. Good agreement was found with previous results and the signatures of quantum interference were found to be present in the six terminal junction.

CHAPTER VI

GRAPHENE ELECTRONICS

Graphene is widely touted as an ideal electrode material (for a brief overview of graphene see section 4.4). In this Chapter the contact properties of graphene with carbon nanotubes and MoS_2 are discussed. The work on graphene-CNT junctions is presented in Section 6.1. Another two-dimensional material, molybdenum disulphide (MoS_2), has recently become a topic of interest due its optical properties. However, as a new material the design of good contact materials requires further study. In Section 6.2 I examine graphene-MoS_2 bilayers with electronic structure calculations. Relevant background information will be given at the beginning of each section.

6.1 Graphene-carbon nanotube junctions

In this section the properties of carbon nanotube(CNT)-graphene junctions are investigated with first-principles electronic structure and electron transport calculations. Contact properties are found to be key factors in determining the performance of nanotube based electronic devices. In a typical single-walled CNT-metal junction there is a p-type Schottky barrier of up to $\sim$ 0.4 eV which depends on the nanotube diameter. Calculations of the Schottky barrier height (SBH) in CNT-graphene contacts indicate that lower barriers are present with graphene electrodes. Current-voltage (IV) characteristics of junctions with finite contact region suggest the suitability of the junctions for applications and provide insight to explain recent experimental

findings.

Carbon nanotubes (CNTs) and graphene have attracted a lot of attention because of their unique electrical, optical, thermal, and mechanical properties[214–217]. Graphene has very large electron mobility at room temperature[150] and is easy to fabricate on a wafer scale[218,219], but does not possess a band gap[150], making it challenging to create graphene-based transistors with the large on/off ratios which are required for logic applications[220]. While CNTs have a useful large energy gap allowing fabrication of transistors with large on/off ratios, the performance of these transistors crucially depends on the contacts between the CNT and the electrodes[214–217]. All-carbon hybrid architectures suited for applications are possible through the combination of advantageous material properties of graphene and nanotubes. For example, a highly efficient all-carbon solar cell could be constructed by combining CNTs to efficiently generate electron-hole pairs[221] with transparent conductive graphene electrodes[222–225].

A long standing issue for CNT and graphene based electronics has been the quality of contacts with electrode materials such as Pd, Ti, or Al[226–229]. A common feature of the CNT-metal contacts has been the presence of a Schottky barrier at the nanotube-metal interface[230,231]. The Schottky barriers severely limit transistor conductance in the "ON" state, and reduce the current delivery capability — a key factor of device performance. High work-function metal (e.g. Pd) contacts have reduced the Schottky barrier providing nearly ohmic contacts to single-walled CNTs[214,228,232] and enabled room-temperature conductance near the ballistic transport limit. Generally it is found that Pd has a negligible Schottky barrier height (SBH) when nanotubes have a diameter larger than ~ 1.4 nm, and that smaller nanotubes such as the (8,0)

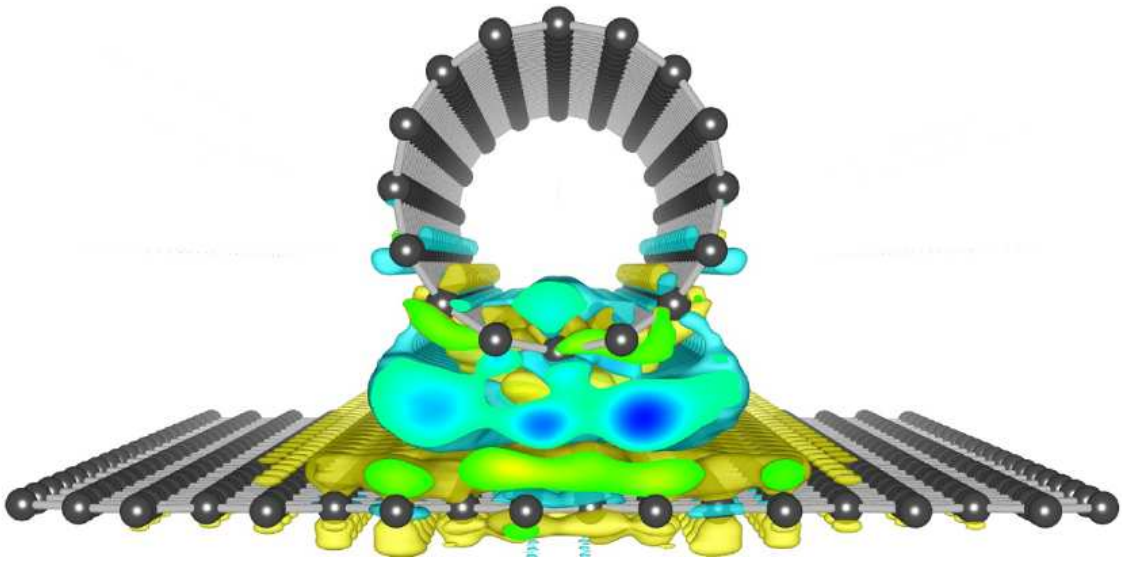

Figure 6.1: Charge transfer between graphene and an (8,0) nanotube. Self-consistent density is obtained for the case of the nanotube far away from the graphene and the case of the graphene and nanotube separated by $d \approx 3.0$ Å. The system is periodic along the nanotube axis. Blue indicates an excess of charge and yellow a depletion.

(diameter ~ 0.62 nm) have barriers of up to ~ 0.4 eV, depending on diameter. The SBH at CNT-metal contacts has also been previously studied with first-principles calculations[233–237], which find that the SBH depends strongly on the atomic details of the system and agreement with the experimental findings that the Ti and Pd(100) contacts have the lowest SBH.

While the properties of graphene or CNTs in contact with common electrode metals have been investigated[214,228,232–237], junctions between the two materials have been the subject of only a few studies. T. Pei *et al.*[238] recently presented measurements with few layer graphene and large nanotubes (diameter unspecified). They conclude that graphene is an unsuitable electrode material for use in transistor devices based on the few devices they measured. However, it should be noted that detailed analysis

of the contact geometry is lacking and it is well known that the work function of graphene depends on the number of layers[239]. Another group has demonstrated that the inclusion of a graphitic interface layer shows improved electronic characteristics in single wall CNT devices[240]. It has also been shown that contact resistance between graphite and multiwalled CNTs can be tuned by controlling the contact geometry[241].

In this section, contact properties of graphene-CNT interfaces are investigated with first-principles calculations. The p-type Schottky barrier height (SBH) is calculated for semiconducting (8,0) and (10,0) nanotubes on graphene surfaces with the potential profile lineup method[233,242]. These calculations correspond to the limit of an extended clean contact region between graphene and a long CNT. With this model it is shown that the SBH is low compared to that found in Pd-CNT contacts. Simulations with a finite contact region show the role of contact region length, edge effects and nanotube chirality in determining the electrical properties. The calculations show that the electronic properties of the junction are primarily determined by the nanotube chirality.

First the barrier heights are calculated in ideal contacts, followed by current-voltage characteristics for (8,0) and (10,0) CNTs in contact with graphene with different length of overlap of graphene and CNTs in the scattering region are presented. The section concludes with a discussion of the results in terms of recent experiments.

Two types of geometries are used in this work: a "device" geometry with a carbon nanotube connected to a graphene lead (see Figure 6.2) and an "ideal" contact geometry where a carbon nanotube sits atop a graphene sheet in a periodic cell (see Figure 6.1). Different methods were used to obtain optimized coordinates in each

case. In the "ideal" case the total energy is minimized by optimizing a number of geometric factors such as rotation of the nanotube, nanotube – graphene distance and translation of the nanotube with respect to the graphene. Following this an unconstrained optimization is done until all forces are less than 0.01 eV/Å. This approach is used to avoid local minima in the energy landscape. All calculations for this geometry are done with density functional theory (DFT) as implemented in VASP[189]. Projected augmented waves are used to represent core electrons and the local density approximation is used for exchange and correlation. The Brilloiun zone is sampled by 15 points along the nanotube axis generated with the Monkhorst-Pack method. In the other case of the "device" geometry, a different procedure is used due to the large cell size, large number of atoms and the non-periodic nature of the geometry. A code based on planewaves is more suitable for smaller systems with periodic simulation cells and is impractical for application to large non-periodic systems which contain large amounts of vacuum. In this case a szp atomic orbital basis set is used. Coordinates are optimized until all forces are less than 0.05 eV/Å and the electrode Brilloiun zones were sampled with a 3×25 grid of kpoints generated by the Monkhorst-Pack method. The self-consistent calculation of the scattering region is done with 3 tranverse kpoints and electron transmission probability curves are generated with 31 transverse kpoints to obtain converged values.

The potential profile lineup method has been used to study the Schottky barrier between metal and semiconductor[242]. A similar approach that has been used to study CNT-metal junctions[233,234] is adopted in this section. The difference between the Fermi level of the combined system and valence band edge of the semiconductor

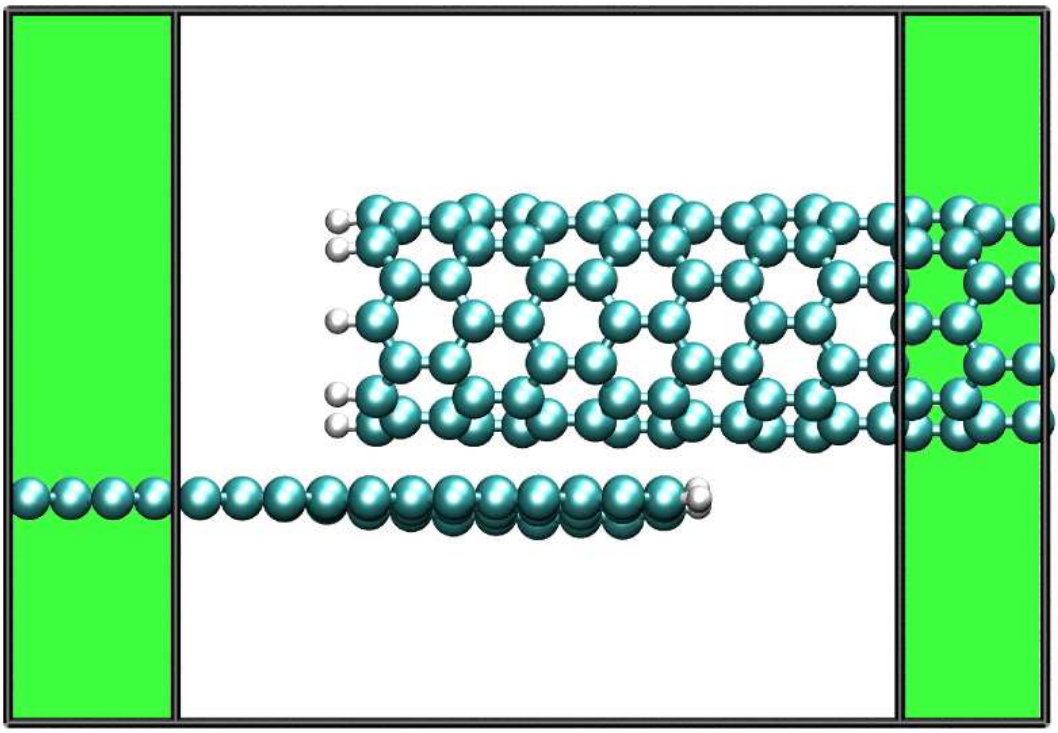

Figure 6.2: Graphene-carbon nanotube device. The nanotube is (8,0) and the graphene is aligned along the zigzag direction with an overlap region of 10 Å. The boxes indicate scattering and electrode regions with the electrode regions highlighted in greeen.

is the p-type Schottky barrier:

$$\Delta_p = E_F - E_V, \tag{6.1}$$

where E_F is the Fermi level of the combined graphene-nanotube system and E_V is valence band edge of the nanotube. The SBH, Δ_p, can be determined by comparing features of the metal/semiconductor combined system to those of the pure semiconductor system by rewriting (1) as

$$\Delta_p = (E_F - \langle V_1 \rangle_{\mathrm{CNT}}) - (E_V - \langle V_2 \rangle_{\mathrm{CNT}})\,. \tag{6.2}$$

The average potential at an atomic core in system i is indicated by $\langle V_i \rangle$. The atomic core potential is used to line up the energy levels of the nanotube-only calculation and the combined graphene-nanotube calculation. In the calculation E_F and $\langle V_1 \rangle$ are taken from the combined system and $\langle V_1 \rangle$ is evaluated only with the carbon atoms which are furthest from the graphene. This is done to reduce error associated with charge transfer. Charge transfer was analyzed via a Bader charge analysis[243], where the density is partitioned accoring to zero-flux surfaces indicating the charge assosiated with each atom. Analysis reveals that the charge transfer is limited to the interface region. The valence band edge E_V and $\langle V_2 \rangle$ are taken from a calculation with a nanotube only. In this case, with only the nanotube in the simulation cell, the average is done over all atoms in the nanotube.

This approach is used to calculate the p-type Schottky barrier heights for (8,0)

Table VI.1: Properties of nanotubes: E_b is the calculated band gap, d is the nanotube diameter, and Δ_p is the p-type Schottky barrier

Nanotube	E_b (eV)	d (nm)	Δ_p (eV)
(8,0)	0.55	0.63	0.094
(10,0)	0.8	0.78	0.04

and (10,0) nanotubes with calculated band gaps of 0.55 eV and 0.8 eV, respectively. These nanotubes are the smallest "big gap" semiconducting nanotubes with diameters of $\sim$ 0.62 nm and $\sim$ 0.78 nm. A SBH of 0.094 eV was found in the (8,0) case and 0.04 eV was found in the (10,0) case, significantly lower than the valued measured in Pd-CNT junctions $\Delta_p \approx 0.4$ eV[227]. These results are summarized in Table VI.1. This is in contrast to the measured value of $\Delta_p \approx 0.4$ eV in Pd-CNT junctions[227]. The redesitribution of charge between the graphene and CNT is shown in Figure 6.1 indicating the formation of bonds. The low Schottky barrier can be attributed to the similiar work function of graphene (4.5 eV) and CNT (4.5-4.8 eV)[244] and the quality of contact in the calculation. While the workfunction of small zigzag nanotubes is known to vary with nanotube diameter, deviation from the 4.5 eV value is expected to start with (8,0) nanotubes ($\sim$ 4.75 eV) and increase with smaller diamter[244]. Measurements done with multi-layer graphene (with a varying workfunction[239]) and unclear contact quality that show the presence of barriers[238] can be attributed to these factors. This conclusion is supported by measurements where a graphitic layer surrounds the nanotube and improved characteristics such as higher "ON" currents are observed after an annealing process[240].

To compliment the calculation of the SBH the current-voltage (IV) characteristics

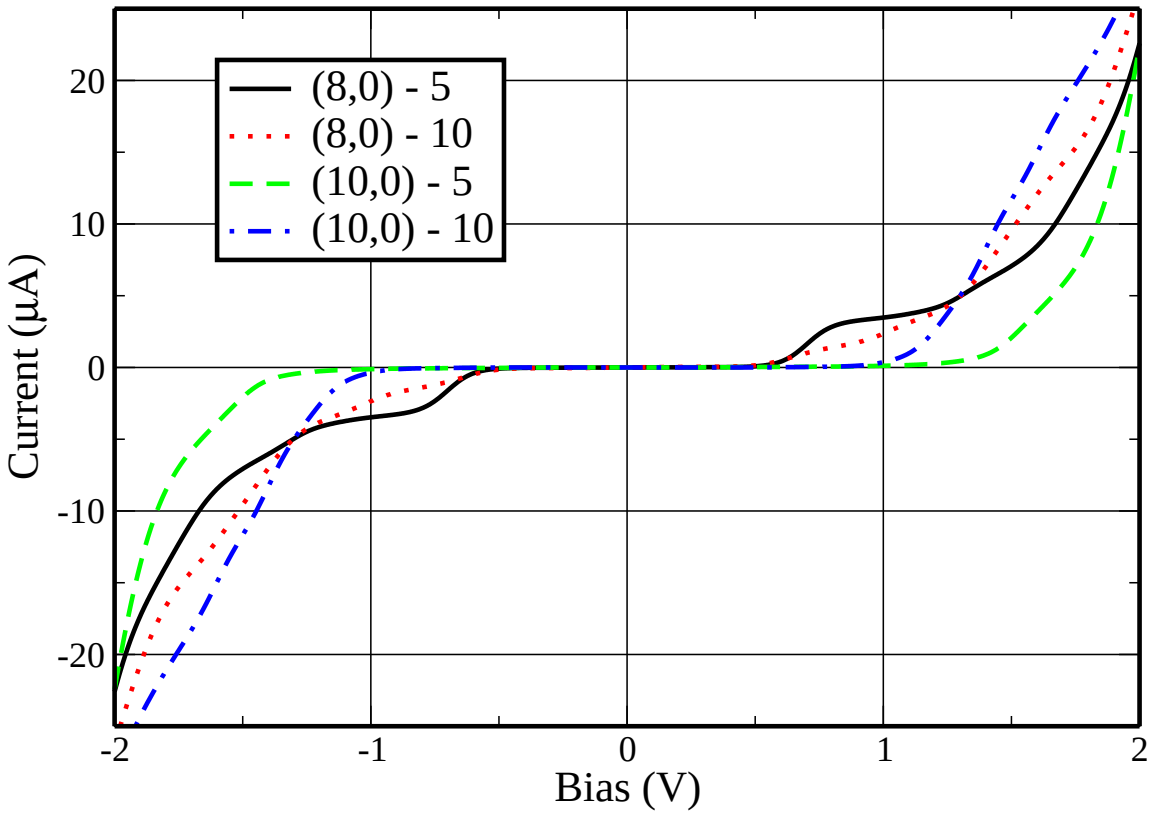

Figure 6.3: Calculated current-voltage response for various CNT-graphene junctions. The low-bias transmission spectrum is integrated to obtain the IV curves. Curves with (8,0) and (10,0) nanotubes with a 5 Å and 10 Å of overlap with the graphene are shown (see Figure 6.2).

of CNT-graphene junctions with (8,0) and (10,0) nanotubes are investaged within the NEGF-DFT formalism. For each nanotube two different lengths of overlap region between the CNT and graphene electrode, namely 5 Å and 10 Å, are used. The graphene electrodes are aligned along the zigzag direction. Some general trends can be observed in the computed IV characteristics (see Figure 6.3). Increasing the length of the overlap region between the carbon nanotube and graphene decreases the transport gap toward the value expected for just the nanotube alone. This suggests that the influence of edge effects is decreased as the overlap region is extended. The size of

transport gap depends also on the CNT — the nanotube with the larger band gap, the (10,0) has a larger transport gap. These points indicate that the charactistics of junctions depend strongly on the specific nanotube employed. Note that the profile of the IV curve differs between nanotubes: junctions with (8,0) nanotubes show a small initial increase in current followed by a sharper increase at high voltages, while the (10,0) nanotubes show a single sharp increase in current. In the high bias regions the current obtains high values on the order of 20 μA which is roughly the electron-phonon interaction limited value in singe-wall nanotubes that are longer than the electron mean free path[245]. One can then expect that in a clean interface between a carbon nanotube and graphene the interface will not be the limiting factor.

In conclusion the electronic properties of CNT-graphene contacts were presented in this section. First, it was shown that the p-type Schottky barrier is low in very long ideal junctions with (8,0) and (10,0) nanotubes. Values for the SBH of 0.094 eV and 0.04 eV were found for the (8,0) and (10,0) cases, respectively. These signifcantly lower than the reported values for Pd of $\Delta_p \approx 0.3 - 0.4$ eV. To further investigate the transport properties the current-voltage response of (8,0) and (10,0) nanotubes in contact with graphene was calculated. The chirality of the nanotube was found to be more important than the length of the contact region. These calculations provide qualitative insight into the role of the junctions in determining the IV characteristics. Recent experiments offer conflicting opinions on the suitability of graphitic carbon contacts for applications, such as transistors. The results indicate that the contacts are suitable and suggest that an experiment with single-wall nanotubes contacting suspended graphene may be required to diminish substrate effects.

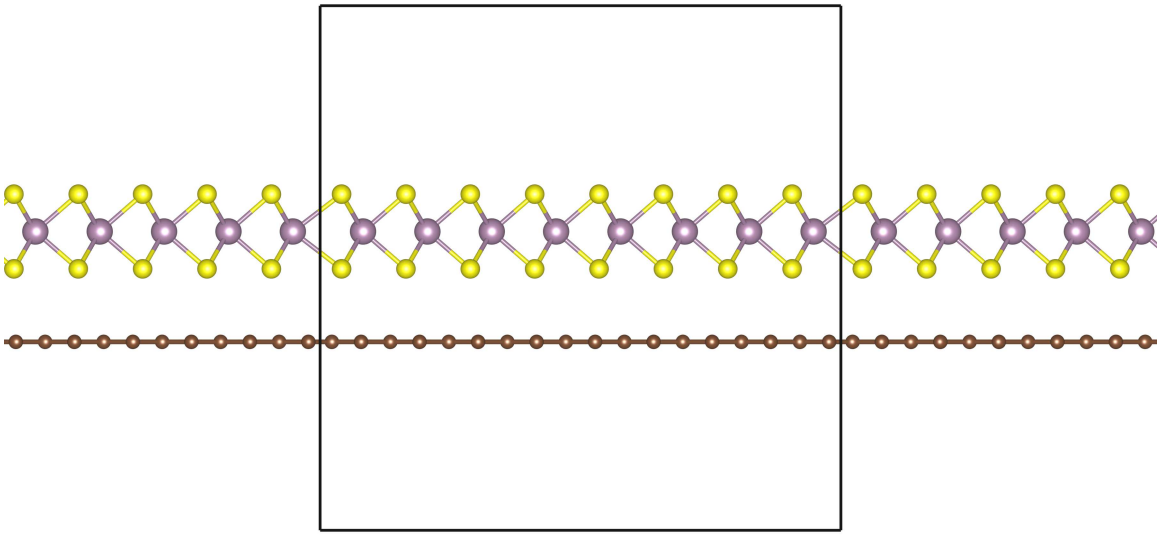

Figure 6.4: Graphene-MoS_2 bilayer. The unit cell used in calculations is shown by the black box.

A variety of two-dimensional materials have been predicted and, since the experimental realization of graphene, others have been observed[152]. Notable are the oxidized forms of graphene and boron nitride (BN)[246] which has a direct band gap[247] and small lattice mismatch with graphene, making[248] it a suitable substrate material[249]. Molybdenum disulphide is another two-dimensional material with a potentially wide range of applications. In bulk form MoS_2 has an indirect gap, but in single layers it has a direct gap of 1.8 eV[250]. Strikingly, this was shown when photoluminescence increased as the number of layers was decreased, highlighting the transition of bulk to the single layer regime. The single layer form has been shown to possess long range order and good stability[251] and has been manufactured with standard mechanical

cleavage, laser thinning[252] and chemical means[253,254]. Functional transistors based on single layers of the material with high on/off ratios of over 10^8 and high mobilities of $200 - 500$ cm$^2V^{-1}s^{-1}$ [255] have been demonstrated. For comparison, electron mobility in silicon is $450 - 1400$ cm$^2V^{-1}s^{-1}$ and mobilities as high as 200000 cm$^2V^{-1}s^{-1}$ have been reported in graphene[256]. However, the reported high mobility in MoS_2 is atypical and much lower observed mobilities are common. This has recently motivated searches for contact materials which outperform the usual Au electrodes. With density functional calculations using a PBE functional, it was suggested that Ti contacts are a reasonable alternative[257].

It is natural to consider the combination of graphene and MoS_2, where graphene is ideal as an electrode material and MoS_2 provides the useful direct band gap. A side view of the combined graphene-MoS_2 system is shown in Figure 6.4. However, few works have been published on the combination of the two materials[258–260]. Density functional calculations suggest an inter-layer spacing of 3.32 Å and small band gap of 2 meV induced in the graphene[258], otherwise theoretical analysis of the combined material has not been published. Combinations of the materials have been demonstrated via a solution-phase method[260] with the goal of creating a battery electrode material, but the realization of single layer MoS_2 is unclear via this method. Another group showed a similar method for producing MoS_2 nanoflakes on reduced graphene oxide[259].

Calculations in this section were done with the GPAW[261,262] code using a double zeta plus polarization LCAO basis, projector augmented waves for the core electrons and a 16 x 8 Monkhorst-Pack sampling of the Brillouin zone. To account for the

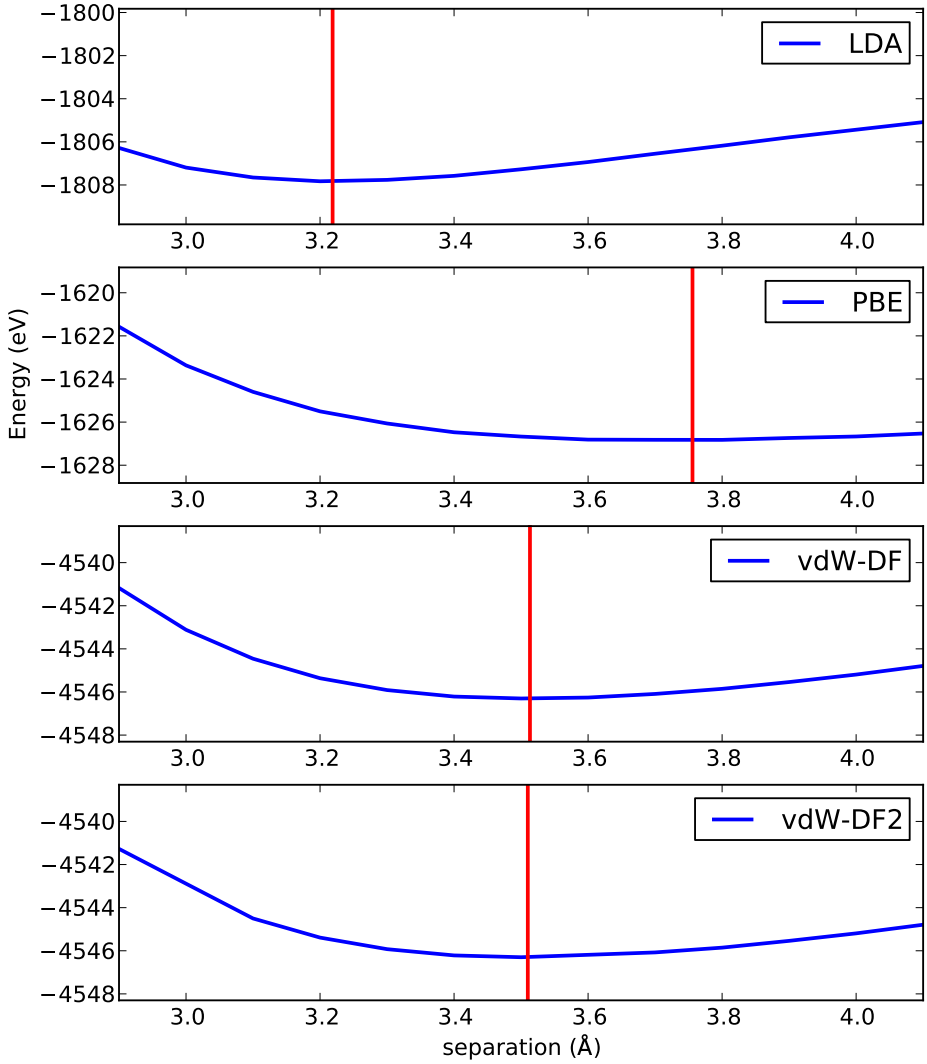

Figure 6.5: Graphene-MoS_2 bilayer spacing calculated with several exchange-correlation functionals. The vertical lines indicate the minima of fitted curves. The values from top to bottom are 3.22, 3.76, 3.51 and 3.51.

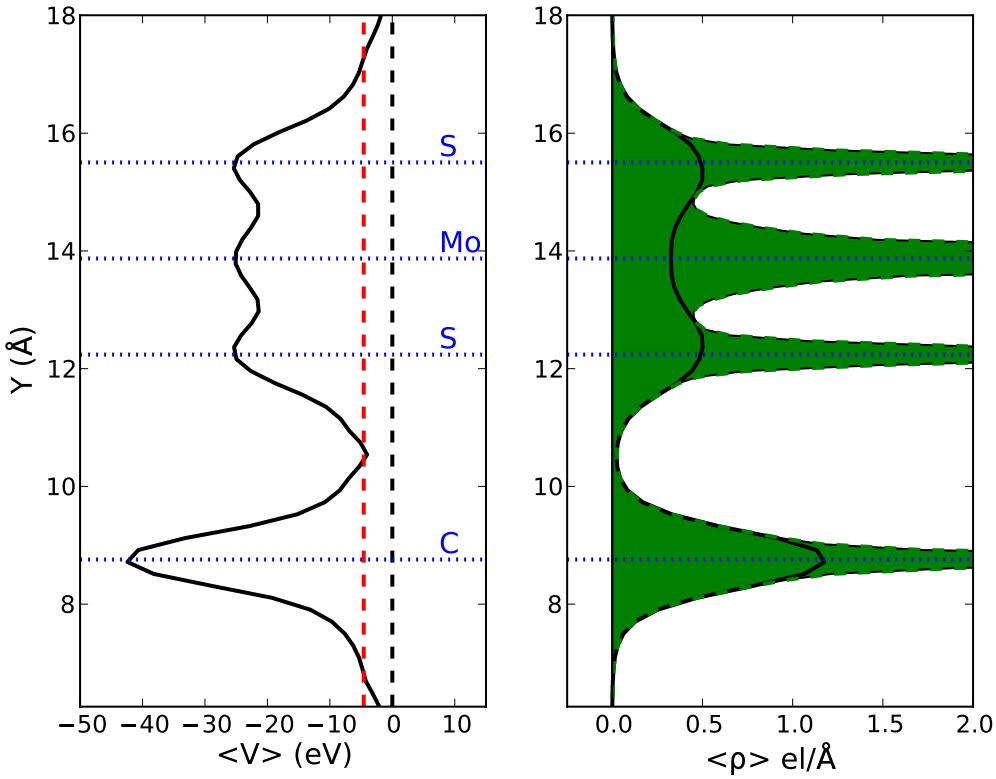

Figure 6.6: Graphene-MoS_2 bilayer density and potential. The average location of each plane of atoms is shown by the dashed blue lines. On the left the vacuum level is 0 eV, the plane averaged potential is shown with a solid black line and the Fermi level is indicated by the dashed red curve. On the right the all-electron density is shaded in green and the black line is the pseudo-valence density.

Table VI.2: Graphene-MoS_2 properties computed with a range of exchange-correlation functionals. The MoS_2 band gap, E_g, p-type and n-type Schottky barrier heights, Δ_p and Δ_n, and tunneling barrier height Φ_B are shown.

XC functional	E_g (eV)	Δ_p (eV)	Δ_n (eV)	Φ_B (eV)	d (Å)
LDA	1.593	1.243	0.349	-1.444	3.22
PBE	1.571	1.404	0.167	1.021	3.76
vdW-DF	1.575	1.285	0.289	0.988	3.51
vdW-DF2	1.590	1.417	0.173	0.538	3.51

different unit cells of graphene and MoS_2 a simulation box with 108 C atoms in the graphene layer and 96 atoms in the MoS_2 layer was used. There is still a small lattice mismatch, so MoS_2 was strained by approximately 1% to match the optimized graphene cell. The layers were separated from the edge of the simulation box by 10 Å on both sides.

In bulk form graphene and MoS_2 layers are bound by van der Waals forces, which are not described correctly by standard functionals. For this reason all simulations in this section were done with a range of exchange-correlation functionals: LDA, PBE, vdW-DF[263] and vdW-DF2[264] . Figure 6.5 shows the total energy as a function of layer separation (distance between the highest C atom and lowest S atom) for each functional and Table VI.2 summarizes computed properties such as band gap for the range of functionals. In the case of LDA an interlayer spacing of 3.22 Å was found, which compares well to a value found by another group using LDA with a planewave basis set[258]. As expected PBE predicts a larger value than LDA of 3.76 Å. However, when two related functionals which contain van der Waals corrections are used values of 3.51 Å are found. The vdW-DF2 functional is preferred to the vdW-DF functional

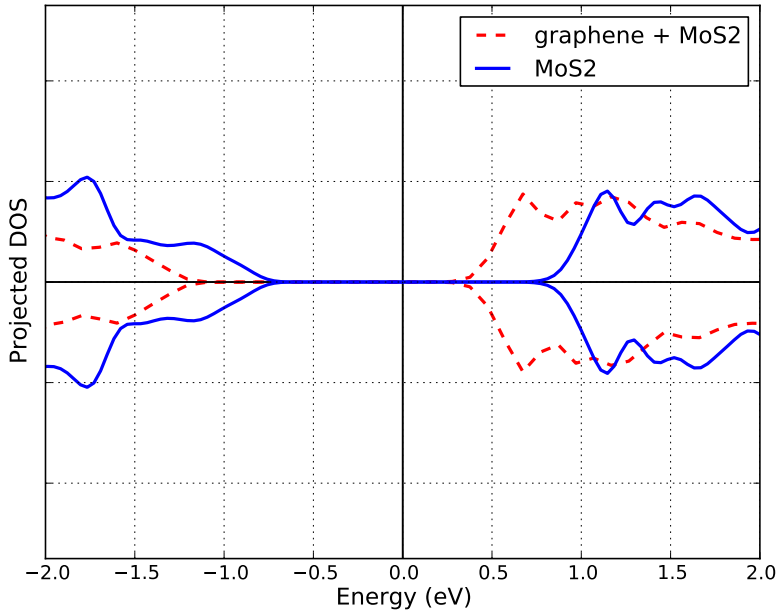

Figure 6.7: Projected density of states on S atoms in graphene-MoS_2. The top and bottom curves correspond to the top and bottom layers of S atoms. Solid blue lines indicate the case of free standing MoS_2 and the dashed red lines show MoS_2 on graphene. The bottom layer of S atoms is closer to the graphene in this case.

as it shows slight improvement over vdW-DF when compared against accurate coupled cluster calculations[264]. In light of these factors the vdW-DF2 functional is used in generating the figures in this section.

Photocurrent measurements have revealed information about defect/impurity trapping in MoS_2 and the Schottky barrier between Au (and Ti) and MoS_2[265]. Using the potential profile lineup method[233,242], as in section 6.1, the Schottky barrier height can be calculated in graphene-MoS_2 contacts. Barrier heights and band gaps calculated with the different functionals are shown in Table VI.2. All functionals used consistently underestimate the experimental MoS_2 gap of 1.8 eV. Figure 6.6 shows the potential and density in the combined system, averaged in planes parallel to the

layers. In the left panel of Figure 6.6 the vacuum level is shown at 0 eV and the dashed red line indicates the Fermi level. On average the potential is just above the Fermi level indicating a barrier for electrons passing between the materials, the difference between this potential maximum and Fermi level is defined as Φ_B. In particular, LDA predicts no barrier for electrons with $\Phi_B = -1.444$ eV and vdW-DF2 predicts $\Phi_B = 0.538$ eV. However, as these are plane-averaged values there are potential paths for electrons in the region between the graphene and bottom layer of S atoms. The region of potential exceeding the Fermi level is approximately 0.2-0.5 Å with the functionals that predict a barrier — much shorter than the 0.9 Å and 1.59 Å reported for Ti and Au, respectively[257]. On the right panel of Figure 6.6 the all-electron density is shown in green and the pseudo-valence density is shown by the solid black curve. The explanation of paths in the potential allowing charge transfer is supported by the non-zero electron density in the contact region.

The local density of states near the Fermi energy is an important factor in determining the electronic properties of a junction. Figures 6.7, 6.8 and 6.9 compare the projected density of states on the S, C and Mo atoms in the cases when the graphene and MoS_2 are separated and in contact. In Figure 6.7 a distinction between the top and bottom S atoms is made, where the bottom atoms are closest to the graphene layer. When brought into contact with graphene the states of the S and Mo atoms are shifted towards the Fermi level, with the Mo states moving the closest. Note that the presence of the graphene does not significantly alter the character of the curves, only shifts them. Graphene's density of states is shifted with the Dirac point above the Fermi level when in contact. To quantify the shifts in states from the contact

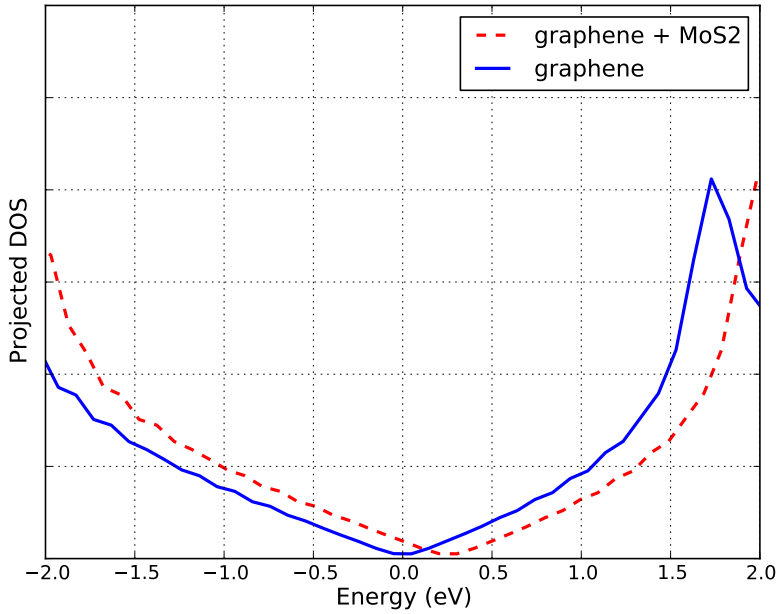

Figure 6.8: Projected density of states on C atoms in graphene-MoS_2

in terms of barriers the p-type Schottky barrier, Δ_p, was calculated, as in Section 6.1, with the potential profile lineup method and the n-type barrier was calculated by $\Delta_n = E_{gap} - \Delta_p$. The results for the range of functionals are given in Table VI.2.

The analysis is completed by examining the spatial distribution of individual states near the Fermi level. The HOMO-2 through LUMO+2 pseudo-wavefunctions squared are shown in Figure 6.10. As in the case of Figure 6.6, the wavefunctions are averaged in planes normal to the graphene and MoS_2 layers. The HOMO, LUMO, LUMO+1 and LUMO+2 states are delocalized across the graphene and MoS_2 and are especially associated with the Mo layer suggesting that this state will play a role in transfer of charge between the graphene and MoS_2. In contrast, the HOMO-1 and HOMO-2 states are strongly associated with the graphene layer.

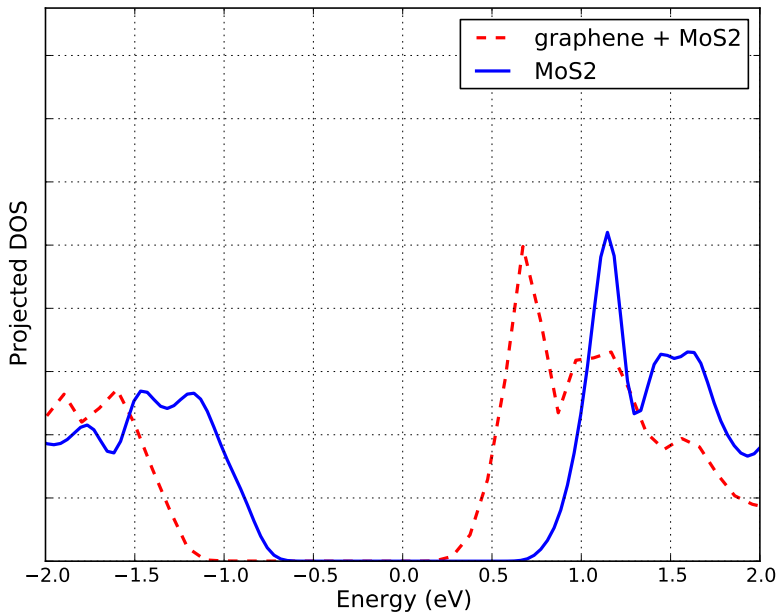

Figure 6.9: Projected density of states on Mo atoms in graphene-MoS_2

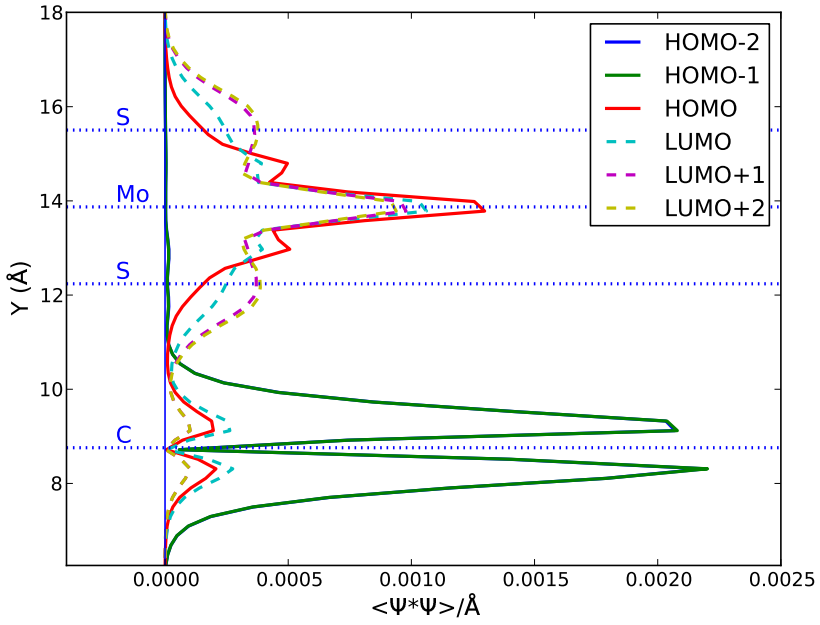

Figure 6.10: Spatial distribution of states near the Fermi level in graphene-MoS_2. The dashed blue lines indicate the averaged location of atoms in each plane.

In conclusion, the electrical contact properties of graphene-MoS_2 junctions were examined with density functional theory calculations using a range of exchange-correlation functionals. Analysis was mainly done in terms of van der Waals corrected functionals, with barrier heights, band gaps, charge density distribution, density of states and wavefunctions near the Fermi level all investigated. The calculations show that graphene should form good contacts with MoS_2 which allow the creation of high quality devices.

CHAPTER VII

CONCLUSION

In this dissertation the properties of nanoscale devices including molecular break junctions, nanowires, nanotubes, graphene and MoS_2 were investigated primarily with density functional theory. Ground state properties such as density of states and optimized geometries were computed via standard density function theory and transport properties were calculated by non-equilibrium Green's function and complex absorbing potential frameworks using a DFT Hamiltonian. A key development included the extension of the complex absorbing potential framework to the general N-terminal case.

The formalism used throughout this thesis is presented in Chapter II. There the foundations of density functional theory, including the Hohenberg-Kohn theorem, Kohn-Sham equations, basis sets and exchange and correlation functions can be found. In addition, elements of scattering theory and the extension of the complex absorbing potential formalism to the general case of devices with N terminals are presented. As crossbar geometries are realized with thinner, more densely packed wires[201], the need for analysis which accounts for quantum effects will become more necessary. With multi-probe STMs becoming more available and self-assembly techniques advancing more, multi-terminal measurements of nanoscale systems will be made. The formalism described in this thesis sets the groundwork for calculation of electronic properties of these systems.

Details of the computational techniques are presented in Chapter III. The self-consistent solution procedure, parallel implementation, memory efficiency and finite difference operations are discussed. Also, the issue of convergence in calculated transport properties is addressed with an example calculation. These computational techniques have been implemented in the Varga group's DFT suite and provide the ground work for studying larger and more complex systems with less time.

Nanowires are examined in Chapter IV; the focus of this chapter is on kinked nanowires and gold nanowire break junctions. Atomic chains, silicon nanowires and graphene nanoribbons with kink and related defects are discussed. In general it found that quantum interference effects are responsible for significant decreases in conductance and, in some cases, large on/off oscillations in conductance. The role of polytetrahedral clusters in elongated gold nanowires was examined through transport calculations where the geometry was taken from snapshots of molecular dynamics simulations. Finally, it was found that a proposed molecular switch, tetraphenylporphyrin, did not show signs of switching when contacted with two gold nanowires in a break junction configuration. Extension of this work to passivated nanowires and the inclusion of finite voltages in the calculations are possible future directions of this work. However, computational advances will be required as the dimension of the realistic systems shown here is large.

Multi-terminal devices were discussed in Chapter V. Validation of the formalism was done on a model system with a tight-binding Hamiltonian. The analytical solution of the model system in the case of a single junction of N wires is presented and compared with numerical results and perfect agreement was found. The model

calculations also highlighted the unique oscillations in the transmission spectra of crossbar systems. A density functional Hamiltonian was used to study a four terminal graphene junction and a six terminal carbon nanotube junction.

Graphene based electronics were analyzed in Chapter VI. The electronic properties carbon nanotube-graphene junctions were simulated. When graphene is used as an electrode a lower p-type Schottky barrier was found than in the case of a standard electrode metal. The chirality of the nanotube is found to be the most important factor in determining electrical characteristics. Transport calculations supplement the discussion by showing the favorable IV characteristics of the junctions. Graphene's interaction with another two-dimensional material, MoS_2, was also addressed in this chapter. Different exchange-correlation functionals were evaluated in determining the equilibrium geometry and electronic properties. It was found that graphene could provide a suitable alternative to Au electrodes for creating high quality MoS_2 devices. A recent development known as *valleytronics* makes use of the fact that some materials have multiple minima in momentum space with matching energies[266–268]. Two papers appearing at nearly the same time show that polarized light can be used to preferentially excite carriers in a single valley[269,270]. Future work will examine the valley polarization in the combined system of graphene and MoS_2.

[1] BJ Van Wees, H. Van Houten, CWJ Beenakker, J.G. Williamson, LP Kouwenhoven, D. Van der Marel, and CT Foxon. Quantized conductance of point contacts in a two-dimensional electron gas. *Physical Review Letters*, 60(9):848–850, 1988.

[2] L. Olesen, E. Laegsgaard, I. Stensgaard, F. Besenbacher, J. Schiøtz, P. Stoltze, K. W. Jacobsen, and J. K. Nørskov. Quantized conductance in an atom-sized point contact. *Physical Review Letters*, 72:2251–2254, Apr 1994.

[3] Hideaki Ohnishi, Yukihito Kondo, and Kunio Takayanagi. Quantized conductance through individual rows of suspended gold atoms. *Nature*, 395(6704):780–783, Oct 1998.

[4] W. Kohn, A. D. Becke, and R. G. Parr. Density functional theory of electronic structure. *The Journal of Physical Chemistry*, 100(31):12974–12980, 1996.

[5] R.G. Parr and W. Yang. *Density-functional theory of atoms and molecules*, volume 16. Oxford University Press, USA, 1994.

[6] W. Koch, M.C. Holthausen, and M.C. Holthausen. *A chemist's guide to density functional theory*, volume 2. Wiley Online Library, 2001.

[7] Jeremy Taylor, Hong Guo, and Jian Wang. Ab initio modeling of quantum transport properties of molecular electronic devices. *Physical Review B*, 63(24):245407, Jun 2001.

[8] X.-G. Zhang, Kalman Varga, and Sokrates T. Pantelides. Generalized bloch theorem for complex periodic potentials: A powerful application to quantum transport calculations. *Physical Review B*, 76(3):035108, Jul 2007.

[9] K. Stokbro, J. Taylor, M. Brandbyge, and P. Ordejón. Transiesta: a spice for molecular electronics. *Annals of the New York Academy of Sciences*, 1006(1):212–226, 2003.

[10] Brandon G. Cook, Peter Dignard, and Kálmán Varga. Calculation of electron transport in multiterminal systems using complex absorbing potentials. *Physical Review B*, 83:205105, May 2011.

[11] B. G. Cook and K. Varga. Conductance of kinked nanowires. *Applied Physics Letters*, 98(5):052104, 2011.

[12] J.A. Driscoll, B. Cook, S. Bubin, and K. Varga. First-principles study of field emission from carbon nanotubes and graphene nanoribbons. *Journal of Applied Physics*, 110:024304, 2011.

[13] Christopher R. Iacovella, William R. French, Brandon G. Cook, Paul R. C. Kent, and Peter T. Cummings. Role of polytetrahedral structures in the elongation and rupture of gold nanowires. *ACS Nano*, 5(12):10065–10073, 2011.

[14] P. Hohenberg and W. Kohn. Inhomogeneous electron gas. *Phys. Rev.*, 136(3B):B864–B871, Nov 1964.

[15] E. Kaxiras. *Atomic and electronic structure of solids*. Cambridge Univ Pr, 2003.

[16] W.E. Pickett. Pseudopotential methods in condensed matter applications. *Computer Physics Reports*, 9(3):115–197, 1989.

[17] N. Troullier and J.L. Martins. Efficient pseudopotentials for plane-wave calculations. *Physical Review B*, 43(3):1993–2006, 1991.

[18] D. R. Hamann. Generalized norm-conserving pseudopotentials. *Physical Review B*, 40:2980–2987, Aug 1989.

[19] David Vanderbilt. Optimally smooth norm-conserving pseudopotentials. *Physical Review B*, 32:8412–8415, Dec 1985.

[20] Leonard Kleinman and D. M. Bylander. Efficacious form for model pseudopotentials. *Physical Review Letters*, 48(20):1425–1428, May 1982.

[21] Srgio Filipe Sousa, Pedro Alexandrino Fernandes, and Maria Joo Ramos. General performance of density functionals. *The Journal of Physical Chemistry A*, 111(42):10439–10452, 2007.

[22] D. M. Ceperley and B. J. Alder. Ground state of the electron gas by a stochastic method. *Physical Review Letters*, 45:566–569, Aug 1980.

[23] J. P. Perdew and Alex Zunger. Self-interaction correction to density-functional approximations for many-electron systems. *Physical Review B*, 23:5048–5079, May 1981.

[24] C D Hu and David C Langreth. A spin dependent version of the langreth-mehl exchange-correlation functional. *Physica Scripta*, 32(4):391, 1985.

[25] J.P. Perdew. Generalized gradient approximations for exchange and correlation: A look backward and forward. *Physica B: Condensed Matter*, 172(1-2):1–6, 1991.

[26] A. D. Becke. Density-functional exchange-energy approximation with correct asymptotic behavior. *Phys. Rev. A*, 38:3098–3100, Sep 1988.

[27] John P. Perdew. Density-functional approximation for the correlation energy of the inhomogeneous electron gas. *Physical Review B*, 33:8822–8824, Jun 1986.

[28] John P. Perdew and Wang Yue. Accurate and simple density functional for the electronic exchange energy: Generalized gradient approximation. *Physical Review B*, 33:8800–8802, Jun 1986.

[29] John P. Perdew. Accurate density functional for the energy: Real-space cutoff of the gradient expansion for the exchange hole. *Physical Review Letters*, 55:1665–1668, Oct 1985.

[30] David C. Langreth and M. J. Mehl. Beyond the local-density approximation in calculations of ground-state electronic properties. *Physical Review B*, 28:1809–1834, Aug 1983.

[31] David C. Langreth and John P. Perdew. Theory of nonuniform electronic systems. i. analysis of the gradient approximation and a generalization that works. *Physical Review B*, 21:5469–5493, Jun 1980.

[32] H.L. Schmider and A.D. Becke. Optimized density functionals from the extended g2 test set. *The Journal of chemical physics*, 108:9624, 1998.

[33] Jianmin Tao, John P. Perdew, Viktor N. Staroverov, and Gustavo E. Scuseria. Climbing the density functional ladder: Nonempirical meta-generalized gradient approximation designed for molecules and solids. *Physical Review Letters*, 91:146401, Sep 2003.

[34] Y. Zhao and D.G. Truhlar. The m06 suite of density functionals for main group thermochemistry, thermochemical kinetics, noncovalent interactions, excited states, and transition elements: two new functionals and systematic testing of four m06-class functionals and 12 other functionals. *Theoretical Chemistry Accounts: Theory, Computation, and Modeling (Theoretica Chimica Acta)*, 120(1):215–241, 2008.

[35] Axel D. Becke. Density-functional thermochemistry. iii. the role of exact exchange. *The Journal of Chemical Physics*, 98(7):5648–5652, 1993.

[36] Jochen Heyd and Gustavo E. Scuseria. Efficient hybrid density functional calculations in solids: Assessment of the heyd–scuseria–ernzerhof screened coulomb hybrid functional. *The Journal of Chemical Physics*, 121(3):1187–1192, 2004.

[37] O.A. Vydrov and T. Van Voorhis. Nonlocal van der waals density functional made simple. *Physical review letters*, 103(6):63004, 2009.

[38] G. Román-Pérez and J.M. Soler. Efficient implementation of a van der waals density functional: application to double-wall carbon nanotubes. *Physical review letters*, 103(9):96102, 2009.

[39] John P. Perdew, J. A. Chevary, S. H. Vosko, Koblar A. Jackson, Mark R. Pederson, D. J. Singh, and Carlos Fiolhais. Atoms, molecules, solids, and surfaces: Applications of the generalized gradient approximation for exchange and correlation. *Physical Review B*, 46:6671–6687, Sep 1992.

[40] Marco Buongiorno Nardelli, J.-L. Fattebert, and J. Bernholc. $o(n)$ real-space method for ab initio quantum transport calculations: Application to carbon nanotube–metal contacts. *Physical Review B*, 64(24):245423, Dec 2001.

[41] N. D. Lang. Resistance of atomic wires. *Physical Review B*, 52:5335–5342, Aug 1995.

[42] M. Di Ventra, S. T. Pantelides, and N. D. Lang. First-principles calculation of transport properties of a molecular device. *Physical Review Letters*, 84(5):979–982, Jan 2000.

[43] K. Varga. r -matrix calculation of bloch states for scattering and transport problems. *Physical Review B*, 80(8):085102, Aug 2009.

[44] Massimiliano Di Ventra. *Electrical Transport in Nanoscale Systems*. Cambridge University Press, 2008.

[45] S. Datta. *Electronic transport in mesoscopic systems*. Cambridge Univ Pr, 1997.

[46] S. Datta. *Quantum transport: atom to transistor*. Cambridge Univ Pr, 2005.

[47] K. Varga and J.A. Driscoll. *Computational Nanoscience: Applications for Molecules, Clusters, and Solids*. Cambridge Univ Pr, 2011.

[48] J. A. Driscoll and K. Varga. Calculation of self-energy matrices using complex absorbing potentials in electron transport calculations. *Physical Review B*, 78(24):245118, Dec 2008.

[49] K. Varga and S. T. Pantelides. Quantum transport in molecules and nanotube devices. *Physical Review Letters*, 98(7):076804, Feb 2007.

[50] Sergey V. Faleev, François Léonard, Derek A. Stewart, and Mark van Schilfgaarde. Ab initio tight-binding lmto method for nonequilibrium electron transport in nanosystems. *Physical Review B*, 71(19):195422, May 2005.

[51] J. J. Palacios, A. J. Pérez-Jiménez, E. Louis, E. SanFabián, and J. A. Vergés. First-principles phase-coherent transport in metallic nanotubes with realistic contacts. *Physical Review Letters*, 90(10):106801, Mar 2003.

[52] K. Stokbro, J. Taylor, M. Brandbyge, J. L. Mozos, and P. Ordejón. Theoretical study of the nonlinear conductance of di-thiol benzene coupled to au(111) surfaces via thiol and thiolate bonds. *Computational Materials Science*, 27(1-2):151 – 160, 2003.

[53] Eldon G. Emberly and George Kirczenow. Models of electron transport through organic molecular monolayers self-assembled on nanoscale metallic contacts. *Physical Review B*, 64(23):235412, Nov 2001.

[54] Marco Buongiorno Nardelli, J.-L. Fattebert, and J. Bernholc. $o(n)$ real-space method for ab initio quantum transport calculations: Application to carbon nanotube–metal contacts. *Physical Review B*, 64(24):245423, Dec 2001.

[55] Yongqiang Xue, Supriyo Datta, and Mark A. Ratner. Charge transfer and "band lineup" in molecular electronic devices: A chemical and numerical interpretation. *J. Chem. Phys.*, 115(9):4292–4299, 2001.

[56] K.S. Thygesen and K.W. Jacobsen. Molecular transport calculations with wannier functions. *Chemical Physics*, 319(1-3):111 – 125, 2005. Molecular Charge Transfer in Condensed Media - from Physics and Chemistry to Biology and Nanoengineering in honour of Alexander M. Kuznetsov on his 65th birthday.

[57] San-Huang Ke, Harold U. Baranger, and Weitao Yang. Electron transport through molecules: Self-consistent and non-self-consistent approaches. *Physical Review B*, 70(8):085410, Aug 2004.

[58] Pedro A. Derosa and Jorge M. Seminario. Electron transport through single molecules: scattering treatment using density functional and green function theories. *The Journal of Physical Chemistry B*, 105(2):471–481, 2001.

[59] S. Sanvito, C. J. Lambert, J. H. Jefferson, and A. M. Bratkovsky. General green's-function formalism for transport calculations with *spd* hamiltonians and giant magnetoresistance in co- and ni-based magnetic multilayers. *Physical Review B*, 59(18):11936–11948, May 1999.

[60] J. A. Driscoll and K. Varga. Convergence in quantum transport calculations: Localized atomic orbitals versus nonlocalized basis sets. *Physical Review B*, 81(11):115412, Mar 2010.

[61] J.R. Taylor. *Scattering theory*. John Wiley and Sons, Inc., 1972.

[62] W.H. Press, S.A. Teukolsky, W.T. Vetterling, and B.P. Flannery. *Numerical recipes in C*. Cambridge university press Cambridge, 1992.

[63] R. Kosloff and D. Kosloff. Absorbing boundaries for wave propagation problems. *Journal of Computational Physics*, 63(2):363 – 376, 1986.

[64] William H. Miller. Beyond transition-state theory: a rigorous quantum theory of chemical reaction rates. *Accounts of Chemical Research*, 26(4):174–181, 1993.

[65] Tamar Seideman and William H. Miller. Calculation of the cumulative reaction probability via a discrete variable representation with absorbing boundary conditions. *The Journal of Chemical Physics*, 96(6):4412–4422, 1992.

[66] J.G. Muga, J.P. Palao, B. Navarro, and I.L. Egusquiza. Complex absorbing potentials. *Physics Reports*, 395(6):357 – 426, 2004.

[67] A. Vibok and G. G. Balint-Kurti. Parametrization of complex absorbing potentials for time-dependent quantum dynamics. *The Journal of Physical Chemistry*, 96(22):8712–8719, 1992.

[68] S Brouard, D Macias, and J G Muga. Perfect absorbers for stationary and wavepacket scattering. *Journal of Physics A: Mathematical and General*, 27(12):L439, 1994.

[69] Georges Jolicard and Jeannette Humbert. Study of the one-channel resonance states. method without a stabilization procedure in the framework of the optical potential model. *Chemical Physics*, 118(3):397 – 405, 1987.

[70] David E. Manolopoulos. Derivation and reflection properties of a transmission-free absorbing potential. *The Journal of Chemical Physics*, 117(21):9552–9559, 2002.

[71] J. A. Driscoll and K. Varga. Calculation of self-energy matrices using complex absorbing potentials in electron transport calculations. *Physical Review B*, 78(24):245118, Dec 2008.

[72] Thomas M. Henderson, Giorgos Fagas, Eoin Hyde, and James C. Greer. Determination of complex absorbing potentials from the electron self-energy. *The Journal of Chemical Physics*, 125(24):244104, 2006.

[73] M P López Sancho, J M López Sancho, and J Rubio. Highly convergent schemes for the calculation of bulk and surface green functions. *Journal of Physics F: Metal Physics*, 15(4):851, 1985.

[74] Julian Velev and William Butler. On the equivalence of different techniques for evaluating the green function for a semi-infinite system using a localized basis. *Journal of Physics: Condensed Matter*, 16(21):R637, 2004.

[75] Tasko P Grozdanov and Ronald McCarroll. Calculations of photodissociation and photoionization cross sections by using a recursive expansion of green's operator with absorbing boundary conditions. *Journal of Physics B: Atomic, Molecular and Optical Physics*, 29(15):3373, 1996.

[76] Vladimir A. Mandelshtam and Howard S. Taylor. A simple recursion polynomial expansion of the green's function with absorbing boundary conditions. application to the reactive scattering. *The Journal of Chemical Physics*, 103(8):2903–2907, 1995.

[77] Hua Guo. A time-independent theory of photodissociation based on polynomial propagation. *The Journal of Chemical Physics*, 108(6):2466–2472, 1998.

[78] Dingguo Xu, Daiqian Xie, and Hua Guo. Theoretical study of predissociation dynamics of hcn/dcn in their first absorption bands. *The Journal of Chemical Physics*, 116(24):10626–10635, 2002.

[79] F. Bouakline, T. P. Grozdanov, L. Andric, and R. McCarroll. Calculations of near-threshold cross sections for photodissociation of ch[sup +] using the lanczos algorithm. *The Journal of Chemical Physics*, 122(4):044108, 2005.

[80] Pter Pulay. Convergence acceleration of iterative sequences. the case of scf iteration. *Chemical Physics Letters*, 73(2):393 – 398, 1980.

[81] G. Kresse and J. Furthmüller. Efficient iterative schemes for ab initio total-energy calculations using a plane-wave basis set. *Physical Review B*, 54(16):11169–11186, Oct 1996.

[82] L. S. Blackford, J. Choi, A. Cleary, E. D'Azevedo, J. Demmel, I. Dhillon, J. Dongarra, S. Hammarling, G. Henry, A. Petitet, K. Stanley, D. Walker, and R. C. Whaley. *ScaLAPACK Users' Guide*. Society for Industrial and Applied Mathematics, Philadelphia, PA, 1997.

[83] Yat Li, Fang Qian, Jie Xiang, and Charles M. Lieber. Nanowire electronic and optoelectronic devices. *Materials Today*, 9(10):18 – 27, 2006.

[84] Sven Barth, Francisco Hernandez-Ramirez, Justin D. Holmes, and Albert Romano-Rodriguez. Synthesis and applications of one-dimensional semiconductors. *Progress in Materials Science*, 55(6):563 – 627, 2010.

[85] Y. Cui, Q. Wei, H. Park, and C.M. Lieber. Nanowire nanosensors for highly sensitive and selective detection of biological and chemical species. *Science*, 293(5533):1289, 2001.

[86] Bozhi Tian, Ping Xie, Thomas J. Kempa, David C. Bell, and Charles M. Lieber. Single-crystalline kinked semiconductor nanowire superstructures. *Nature Nanotechnology*, 4(12):824–829, Dec 2009.

[87] F. Patolsky, G. Zheng, and C.M. Lieber. Fabrication of silicon nanowire devices for ultrasensitive, label-free, real-time detection of biological and chemical species. *Nature Protocols*, 1(4):1711–1724, 2006.

[88] Song Jin, Dongmok Whang, Michael C. McAlpine, Robin S. Friedman, Yue Wu, and Charles M. Lieber. Scalable interconnection and integration of nanowire devices without registration. *Nano Letters*, 4(5):915–919, Apr 2004.

[89] J. Xiang, W. Lu, Y. Hu, Y. Wu, H. Yan, and C.M. Lieber. Ge/si nanowire heterostructures as high-performance field-effect transistors. *Nature*, 441(7092):489–493, 2006.

[90] A. I. Yanson, G. Rubio Bollinger, H. E. van den Brom, N. Agrait, and J. M. van Ruitenbeek. Formation and manipulation of a metallic wire of single gold atoms. *Nature*, 395(6704):783–785, Oct 1998.

[91] Tomoya Ono and Kikuji Hirose. First-principles study of peierls instability in infinite single row al wires. *Physical Review B*, 68(4):045409, Jul 2003.

[92] P. Segovia, D. Purdie, M. Hengsberger, and Y. Baer. Observation of spin and charge collective modes in one-dimensional metallic chains. *Nature*, 402(6761):504–507, 1999.

[93] B.H. Hong, S.C. Bae, C.W. Lee, S. Jeong, and K.S. Kim. Ultrathin single-crystalline silver nanowire arrays formed in an ambient solution phase. *Science*, 294(5541):348–351, 2001.

[94] A.I. Persson, M.W. Larsson, S. Stenström, B.J. Ohlsson, L. Samuelson, and L.R. Wallenberg. Solid-phase diffusion mechanism for gaas nanowire growth. *Nature materials*, 3(10):677–681, 2004.

[95] L.J. Lauhon, M.S. Gudiksen, D. Wang, C.M. Lieber, et al. Epitaxial core-shell and core-multishell nanowire heterostructures. *Nature*, 420(6911):57–61, 2002.

[96] E.C. Garnett, Y.C. Tseng, D.R. Khanal, J. Wu, J. Bokor, and P. Yang. Dopant profiling and surface analysis of silicon nanowires using capacitance–voltage measurements. *Nature Nanotechnology*, 4(5):311–314, 2009.

[97] D.E. Perea, E.R. Hemesath, E.J. Schwalbach, J.L. Lensch-Falk, P.W. Voorhees, and L.J. Lauhon. Direct measurement of dopant distribution in an individual vapour–liquid–solid nanowire. *Nature nanotechnology*, 4(5):315–319, 2009.

[98] E. Koren, N. Berkovitch, and Y. Rosenwaks. Measurement of active dopant distribution and diffusion in individual silicon nanowires. *Nano letters*, 10(4):1163–1167, 2010.

[99] M. Nolan, S. O'Callaghan, G. Fagas, J.C. Greer, and T. Frauenheim. Silicon nanowire band gap modification. *Nano Letters*, 7(1):34–38, 2007.

[100] L.E. Greene, M. Law, D.H. Tan, M. Montano, J. Goldberger, G. Somorjai, and P. Yang. General route to vertical zno nanowire arrays using textured zno seeds. *Nano Letters*, 5(7):1231–1236, 2005.

[101] H. Adhikari, A.F. Marshall, C.E.D. Chidsey, and P.C. McIntyre. Germanium nanowire epitaxy: shape and orientation control. *Nano letters*, 6(2):318–323, 2006.

[102] J.D. Holmes, K.P. Johnston, R.C. Doty, and B.A. Korgel. Control of thickness and orientation of solution-grown silicon nanowires. *Science*, 287(5457):1471–1473, 2000.

[103] JM Krans, JM Van Ruitenbeek, VV Fisun, IK Yanson, and LJ De Jongh. The signature of conductance quantization in metallic point contacts. *Nature*, 375(6534):767–769, 1995.

[104] N. Nilius, TM Wallis, and W. Ho. Development of one-dimensional band structure in artificial gold chains. *Science*, 297(5588):1853, 2002.

[105] M. Krawiec, T. Kwapiński, and M. Jałochowski. Scanning tunneling microscopy of monoatomic gold chains on vicinal si (335) surface: experimental and theoretical study. *physica status solidi (b)*, 242(2):332–336, 2005.

[106] J. Wang, M. Li, and E. I. Altman. Scanning tunneling microscopy study of self-organized au atomic chain growth on ge(001). *Physical Review B*, 70(23):233312, Dec 2004.

[107] Zhen-Chao Dong, Taro Yakabe, Daisuke Fujita, Taizo Ohgi, Duncan Rogers, and Hitoshi Nejoh. Metal atomic chains on the si(100) surface. *Japanese Journal of Applied Physics*, 37(Part 1, No. 3A):807–810, 1998.

[108] C. Blumenstein, J. Schäfer, S. Mietke, S. Meyer, A. Dollinger, M. Lochner, XY Cui, L. Patthey, R. Matzdorf, and R. Claessen. Atomically controlled quantum chains hosting a tomonaga-luttinger liquid. *Nature Physics*, 2011.

[109] J. Schäfer, C. Blumenstein, S. Meyer, M. Wisniewski, and R. Claessen. New model system for a one-dimensional electron liquid: Self-organized atomic gold chains on ge(001). *Physical Review Letters*, 101:236802, Dec 2008.

[110] Xiaolin Li, Xinran Wang, Li Zhang, Sangwon Lee, and Hongjie Dai. Chemically derived, ultrasmooth graphene nanoribbon semiconductors. *Science*, 319(5867):1229–1232, 2008.

[111] Youn-Joo Hyun, Alois Lugstein, Mathias Steinmair, Emmerich Bertagnolli, and Peter Pongratz. Orientation specific synthesis of kinked silicon nanowires grown by the vapourliquidsolid mechanism. *Nanotechnology*, 20(12):125606, 2009.

[112] Huan Chen, Hui Wang, Xiao-Hong Zhang, Chun-Sing Lee, and Shuit-Tong Lee. Wafer-scale synthesis of single-crystal zigzag silicon nanowire arrays with controlled turning angles. *Nano Letters*, 10(3):864–868, Jan 2010.

[113] J. Cai, P. Ruffieux, R. Jaafar, M. Bieri, T. Braun, S. Blankenburg, M. Muoth, A.P. Seitsonen, M. Saleh, X. Feng, et al. Atomically precise bottom-up fabrication of graphene nanoribbons. *Nature*, 466(7305):470–473, 2010.

[114] L. Tapaszto, G. Dobrik, P. Lambin, and L.P. Biro. Tailoring the atomic structure of graphene nanoribbons by scanning tunnelling microscope lithography. *Nature nanotechnology*, 3(7):397–401, 2008.

[115] Ildar R. Musin and Michael A. Filler. Chemical control of semiconductor nanowire kinking and superstructure. *Nano Letters*, 12(7):3363–3368, 2012.

[116] R. Rurali and N. Lorente. Metallic and semimetallic silicon $< 100 >$ nanowires. *Physical Review Letters*, 94(2):026805, Jan 2005.

[117] G. Fagas and J.C. Greer. Ballistic Conductance in Oxidized Si Nanowires. *Nano Letters*, 9:1856–1860, 2009.

[118] Man-Fai Ng, Lei Shen, Liping Zhou, Shuo-Wang Yang, and Vincent B. C. Tan. Geometry dependent iv characteristics of silicon nanowires. *Nano Letters*, 8(11):3662–3667, Oct 2008.

[119] Alexei Svizhenko, Paul W. Leu, and Kyeongjae Cho. Effect of growth orientation and surface roughness on electron transport in silicon nanowires. *Physical Review B*, 75(12):125417, Mar 2007.

[120] M.-V. Fernández-Serra, Ch Adessi, and X. Blase. Conductance, surface traps, and passivation in doped silicon nanowires. *Nano Letters*, 6(12):2674–2678, Nov 2006.

[121] M. V. Fernández-Serra, Ch. Adessi, and X. Blase. Surface segregation and backscattering in doped silicon nanowires. *Physical Review Letters*, 96(16):166805, Apr 2006.

[122] Inna Ponomareva, Madhu Menon, Deepak Srivastava, and Antonis N. Andriotis. Structure, stability, and quantum conductivity of small diameter silicon nanowires. *Physical Review Letters*, 95(26):265502, Dec 2005.

[123] Uzi Landman, Robert N. Barnett, Andrew G. Scherbakov, and Phaedon Avouris. Metal-semiconductor nanocontacts: Silicon nanowires. *Physical Review Letters*, 85(9):1958–1961, Aug 2000.

[124] Troels Markussen, Riccardo Rurali, Mads Brandbyge, and Antti-Pekka Jauho. Electronic transport through si nanowires: Role of bulk and surface disorder. *Physical Review B*, 74(24):245313, Dec 2006.

[125] Troels Markussen, Riccardo Rurali, Xavier Cartoixà, Antti-Pekka Jauho, and Mads Brandbyge. Scattering cross section of metal catalyst atoms in silicon nanowires. *Physical Review B*, 81(12):125307, Mar 2010.

[126] Troels Markussen, Antti-Pekka Jauho, and Mads Brandbyge. Electron and phonon transport in silicon nanowires: Atomistic approach to thermoelectric properties. *Physical Review B*, 79(3):035415, Jan 2009.

[127] Aurélien Lherbier, Martin P. Persson, Yann-Michel Niquet, François Triozon, and Stephan Roche. Quantum transport length scales in silicon-based semiconducting nanowires: Surface roughness effects. *Physical Review B*, 77(8):085301, Feb 2008.

[128] T. Markussen, R. Rurali, A.P. Jauho, and M. Brandbyge. Transport in silicon nanowires: role of radial dopant profile. *Journal of Computational Electronics*, 7(3):324–327, 2008.

[129] Man-Fai Ng, Liping Zhou, Shuo-Wang Yang, Li Yun Sim, Vincent B. C. Tan, and Ping Wu. Theoretical investigation of silicon nanowires: Methodology, geometry, surface modification, and electrical conductivity using a multiscale approach. *Physical Review B*, 76(15):155435, Oct 2007.

[130] Troels Markussen, Riccardo Rurali, Antti-Pekka Jauho, and Mads Brandbyge. Scaling theory put into practice: First-principles modeling of transport in doped silicon nanowires. *Physical Review Letters*, 99(7):076803, Aug 2007.

[131] Tomoki Iwanari, Toyo Sakata, Yutaka Miyatake, Shu Kurokawa, and Akira Sakai. Conductance of si nanowires formed by breaking si-si junctions. *Journal of Applied Physics*, 102(11):114312, 2007.

[132] Troels Markussen, Riccardo Rurali, Antti-Pekka Jauho, and Mads Brandbyge. Scaling theory put into practice: First-principles modeling of transport in doped silicon nanowires. *Physical Review Letters*, 99(7):076803, Aug 2007.

[133] G. Giorgi, X. Cartoixà, A. Sgamellotti, and R. Rurali. Mn-doped silicon nanowires: First-principles calculations. *Physical Review B*, 78(11):115327, Sep 2008.

[134] Riccardo Rurali. Colloquium: Structural, electronic, and transport properties of silicon nanowires. *Rev. Mod. Phys.*, 82(1):427–449, Feb 2010.

[135] N. D. Lang. Anomalous dependence of resistance on length in atomic wires. *Physical Review Letters*, 79(7):1357–1360, Aug 1997.

[136] Petr A. Khomyakov and Geert Brocks. Stability of conductance oscillations in monatomic sodium wires. *Physical Review B*, 74(16):165416, Oct 2006.

[137] R. H. M. Smit, C. Untiedt, G. Rubio-Bollinger, R. C. Segers, and J. M. van Ruitenbeek. Observation of a parity oscillation in the conductance of atomic wires. *Physical Review Letters*, 91(7):076805, Aug 2003.

[138] Y. J. Lee, M. Brandbyge, M. J. Puska, J. Taylor, K. Stokbro, and R. M. Nieminen. Electron transport through monovalent atomic wires. *Physical Review B*, 69(12):125409, Mar 2004.

[139] H.-S. Sim, H.-W. Lee, and K. J. Chang. Even-odd behavior of conductance in monatomic sodium wires. *Physical Review Letters*, 87(9):096803, Aug 2001.

[140] P. Havu, T. Torsti, M. J. Puska, and R. M. Nieminen. Conductance oscillations in metallic nanocontacts. *Physical Review B*, 66(7):075401, Aug 2002.

[141] Tomoya Ono. First-principles study on evenodd conductance oscillation of pt atomic nanowires. *The Journal of Physical Chemistry C*, 113(15):6256–6260, 2009.

[142] Ying Xu, Xingqiang Shi, Zhi Zeng, Zhao Yang Zeng, and Baowen Li. Conductance oscillation and quantization in monatomic al wires. *Journal of Physics: Condensed Matter*, 19(5):056010, 2007.

[143] K. S. Thygesen and K. W. Jacobsen. Four-atom period in the conductance of monatomic al wires. *Physical Review Letters*, 91(14):146801, Sep 2003.

[144] Y. Cui and C.M. Lieber. Functional nanoscale electronic devices assembled using silicon nanowire building blocks. *Science*, 291(5505):851, 2001.

[145] Y. Cui, Z. Zhong, D. Wang, W.U. Wang, and C.M. Lieber. High performance silicon nanowire field effect transistors. *Nano Letters*, 3(2):149–152, 2003.

[146] Hou T. Ng, J. Han, Toshishige Yamada, P. Nguyen, Yi P. Chen, and M. Meyyappan. Single crystal nanowire vertical surround-gate field-effect transistor. *Nano Letters*, 4(7):1247–1252, 2004.

[147] X. Duan, Y. Huang, R. Agarwal, and C.M. Lieber. Single-nanowire electrically driven lasers. *Nature*, 421(6920):241–245, 2003.

[148] V. Schmidt, J. V. Wittemann, and U. Gosele. Growth, thermodynamics, and electrical properties of silicon nanowires. *Chemical Reviews*, 110(1):361–388, 2010.

[149] K. S. Novoselov, A. K. Geim, S. V. Morozov, D. Jiang, Y. Zhang, S. V. Dubonos, I. V. Grigorieva, and A. A. Firsov. Electric field effect in atomically thin carbon films. *Science*, 306(5696):666–669, 2004.

[150] A. K. Geim and K. S. Novoselov. The rise of graphene. *Nature Materials*, 6(3):183–191, Mar 2007.

[151] Y. Zhang, Y.W. Tan, H.L. Stormer, and P. Kim. Experimental observation of the quantum hall effect and berry's phase in graphene. *Nature*, 438(7065):201–204, 2005.

[152] KS Novoselov, D. Jiang, F. Schedin, TJ Booth, VV Khotkevich, SV Morozov, and AK Geim. Two-dimensional atomic crystals. *Proceedings of the National Academy of Sciences of the United States of America*, 102(30):10451, 2005.

[153] Vernica Barone, Oded Hod, and Gustavo E. Scuseria. Electronic structure and stability of semiconducting graphene nanoribbons. *Nano Letters*, 6(12):2748–2754, 2006. PMID: 17163699.

[154] Y.W. Son, M.L. Cohen, and S.G. Louie. Half-metallic graphene nanoribbons. *Nature*, 444(7117):347–349, 2006.

[155] Katsunori Wakabayashi. Electronic transport properties of nanographite ribbon junctions. *Physical Review B*, 64:125428, Sep 2001.

[156] D.V. Kosynkin, A.L. Higginbotham, A. Sinitskii, J.R. Lomeda, A. Dimiev, B.K. Price, and J.M. Tour. Longitudinal unzipping of carbon nanotubes to form graphene nanoribbons. *Nature*, 458(7240):872–876, 2009.

[157] Melinda Y. Han, Barbaros Özyilmaz, Yuanbo Zhang, and Philip Kim. Energy band-gap engineering of graphene nanoribbons. *Physical Review Letters*, 98:206805, May 2007.

[158] Xinran Wang, Yijian Ouyang, Xiaolin Li, Hailiang Wang, Jing Guo, and Hongjie Dai. Room-temperature all-semiconducting sub-10-nm graphene nanoribbon field-effect transistors. *Physical Review Letters*, 100:206803, May 2008.

[159] L. Brey and HA Fertig. Electronic states of graphene nanoribbons studied with the dirac equation. *Physical Review B*, 73(23):235411, 2006.

[160] Qimin Yan, Bing Huang, Jie Yu, Fawei Zheng, Ji Zang, Jian Wu, Bing-Lin Gu, Feng Liu, and Wenhui Duan. Intrinsic currentvoltage characteristics of graphene nanoribbon transistors and effect of edge doping. *Nano Letters*, 7(6):1469–1473, 2007.

[161] Zhenyu and Li, Jinlong Yang, and J. G. Hou. Half-metallicity in edge-modified zigzag graphene nanoribbons. *Journal of the American Chemical Society*, 130(13):4224–4225, 2008.

[162] Jia Li, Zuanyi Li, Gang Zhou, Zhirong Liu, Jian Wu, Bing-Lin Gu, Jisoon Ihm, and Wenhui Duan. Spontaneous edge-defect formation and defect-induced conductance suppression in graphene nanoribbons. *Physical Review B*, 82:115410, Sep 2010.

[163] Youngki Yoon and Jing Guo. Effect of edge roughness in graphene nanoribbon transistors. *Applied Physics Letters*, 91(7):073103, 2007.

[164] E. R. Mucciolo, A. H. Castro Neto, and C. H. Lewenkopf. Conductance quantization and transport gaps in disordered graphene nanoribbons. *Physical Review B*, 79:075407, Feb 2009.

[165] Dongxu Wang, Jianwei Zhao, Shi Hu, Xing Yin, Shuai Liang, Yunhong Liu, and Shengyuan Deng. Where, and how, does a nanowire break? *Nano Letters*, 7(5):1208–1212, 2007.

[166] P.E. Marszalek, W.J. Greenleaf, H. Li, A.F. Oberhauser, and J.M. Fernandez. Atomic force microscopy captures quantized plastic deformation in gold nanowires. *Proceedings of the National Academy of Sciences*, 97(12):6282, 2000.

[167] Qing Pu, Yongsheng Leng, and Peter T. Cummings. Rate-dependent energy release mechanism of gold nanowires under elongation. *Journal of the American Chemical Society*, 130(52):17907–17912, 2008.

[168] F. Tavazza, L. E. Levine, and A. M. Chaka. Elongation and breaking mechanisms of gold nanowires under a wide range of tensile conditions. *Journal of Applied Physics*, 106(4):043522, 2009.

[169] Pablo Z. Coura, Sergio B. Legoas, Anderson S. Moreira, Fernando Sato, Varlei Rodrigues, Scrates O. Dantas, Daniel Ugarte, and Douglas S. Galvo. On the structural and stability features of linear atomic suspended chains formed from gold nanowires stretching. *Nano Letters*, 4(7):1187–1191, 2004.

[170] Adri C. T. van Duin, Siddharth Dasgupta, Francois Lorant, and William A. Goddard. Reaxff: a reactive force field for hydrocarbons. *The Journal of Physical Chemistry A*, 105(41):9396–9409, 2001.

[171] John A. Keith, Donato Fantauzzi, Timo Jacob, and Adri C. T. van Duin. Reactive forcefield for simulating gold surfaces and nanoparticles. *Physical Review B*, 81:235404, Jun 2010.

[172] S. Müllegger, M. Rashidi, T. Lengauer, E. Rauls, W. G. Schmidt, G. Knör, W. Schöfberger, and R. Koch. Asymmetric saddling of single porphyrin molecules on au(111). *Physical Review B*, 83:165416, Apr 2011.

[173] W. Auwärter, K. Seufert, F. Bischoff, D. Ecija, S. Vijayaraghavan, S. Joshi, F. Klappenberger, N. Samudrala, and J.V. Barth. A surface-anchored molecular four-level conductance switch based on single proton transfer. *Nature Nanotechnology*, 7(1):41–46, 2011.

[174] D. Dolphin. *The porphyrins*. Academic Press New York, 1978.

[175] Willi Auwärter, Knud Seufert, Florian Klappenberger, Joachim Reichert, Alexander Weber-Bargioni, Alberto Verdini, Dean Cvetko, Martina Dell'Angela, Luca Floreano, Albano Cossaro, Gregor Bavdek, Alberto Morgante, Ari P. Seitsonen, and Johannes V. Barth. Site-specific electronic and geometric interface structure of co-tetraphenyl-porphyrin layers on ag(111). *Physical Review B*, 81:245403, Jun 2010.

[176] L. Scudiero, Dan E. Barlow, and K. W. Hipps. Physical properties and metal ion specific scanning tunneling microscopy images of metal(ii) tetraphenylporphyrins deposited from vapor onto gold (111). *The Journal of Physical Chemistry B*, 104(50):11899–11905, 2000.

[177] H. Spillmann, A. Kiebele, M. Sthr, T.A. Jung, D. Bonifazi, F. Cheng, and F. Diederich. A two-dimensional porphyrin-based porous network featuring communicating cavities for the templated complexation of fullerenes. *Advanced Materials*, 18(3):275–279, 2006.

[178] David Ecija, Knud Seufert, Daniel Heim, Willi Auwarter, Claudia Aurisicchio, Chiara Fabbro, Davide Bonifazi, and Johannes V. Barth. Hierarchic self-assembly of nanoporous chiral networks with conformationally flexible porphyrins. *ACS Nano*, 4(8):4936–4942, 2010.

[179] Daniel Heim, David Ecija, Knud Seufert, Willi Auwarter, Claudia Aurisicchio, Chiara Fabbro, Davide Bonifazi, and Johannes V. Barth. Self-assembly of flexible one-dimensional coordination polymers on metal surfaces. *Journal of the American Chemical Society*, 132(19):6783–6790, 2010.

[180] M. Wolf and P. Tegeder. Reversible molecular switching at a metal surface: A case study of tetra-tert-butyl-azobenzene on au (1 1 1). *Surface Science*, 603(10-12):1506–1517, 2009.

[181] Peter Liljeroth, Jascha Repp, and Gerhard Meyer. Current-induced hydrogen tautomerization and conductance switching of naphthalocyanine molecules. *Science*, 317(5842):1203–1206, 2007.

[182] Jrg Henzl, Michael Mehlhorn, Heiko Gawronski, Karl-Heinz Rieder, and Karina Morgenstern. Reversible cistrans isomerization of a single azobenzene molecule. *Angewandte Chemie International Edition*, 45(4):603–606, 2006.

[183] DM Eigler, CP Lutz, and WE Rudge. An atomic switch realized with the scanning tunnelling microscope. *Nature*, 1991.

[184] Jascha Repp, Gerhard Meyer, Fredrik E. Olsson, and Mats Persson. Controlling the charge state of individual gold adatoms. *Science*, 305(5683):493–495, 2004.

[185] Z. J. Donhauser, B. A. Mantooth, K. F. Kelly, L. A. Bumm, J. D. Monnell, J. J. Stapleton, D. W. Price, A. M. Rawlett, D. L. Allara, J. M. Tour, and P. S. Weiss. Conductance switching in single molecules through conformational changes. *Science*, 292(5525):2303–2307, 2001.

[186] V. Iancu and S.W. Hla. Realization of a four-step molecular switch in scanning tunneling microscope manipulation of single chlorophyll-a molecules. *Proceedings of the National Academy of Sciences*, 103(37):13718–13721, 2006.

[187] X. D. Cui, A. Primak, X. Zarate, J. Tomfohr, O. F. Sankey, A. L. Moore, T. A. Moore, D. Gust, G. Harris, and S. M. Lindsay. Reproducible measurement of single-molecule conductivity. *Science*, 294(5542):571–574, 2001.

[188] Constant M. Guedon, Hennie Valkenier, Troels Markussen, Kristian S. Thygesen, Jan C. Hummelen, and Sense Jan van der Molen. Observation of quantum interference in molecular charge transport. *Nature Nanotechnology*, 7(5):304–308, MAY 2012.

[189] G. Kresse and J. Hafner. Ab initio molecular dynamics for liquid metals. *Physical Review B*, 47(1):558–561, Jan 1993.

[190] I. Shiraki, F. Tanabe, R. Hobara, T. Nagao, and S. Hasegawa. Independently driven four-tip probes for conductivity measurements in ultrahigh vacuum. *Surface science*, 493(1):633–643, 2001.

[191] X. Lin, X. B. He, T. Z. Yang, W. Guo, D. X. Shi, H.-J. Gao, D. D. D. Ma, S. T. Lee, F. Liu, and X. C. Xie. Intrinsic current-voltage properties of nanowires with four-probe scanning tunneling microscopy: A conductance transition of zno nanowire. *Applied Physics Letters*, 89(4):043103, 2006.

[192] Tsuyoshi Sekitani, Ute Zschieschang, Hagen Klauk, and Takao Someya. Flexible organic transistors and circuits with extreme bending stability. *Nat Mater*, 9(12):1015–1022, Dec 2010.

[193] Hyunwook Song, Youngsang Kim, Yun Hee Jang, Heejun Jeong, Mark A. Reed, and Takhee Lee. Observation of molecular orbital gating. *Nature*, 462(7276):1039–1043, Dec 2009.

[194] R. de Picciotto, H. L. Stormer, L. N. Pfeiffer, K. W. Baldwin, and K. W. West. Four-terminal resistance of a ballistic quantum wire. *Nature*, 411(6833):51–54, May 2001.

[195] M. S. Fuhrer, J. Nygrd, L. Shih, M. Forero, Young-Gui Yoon, M. S. C. Mazzoni, Hyoung Joon Choi, Jisoon Ihm, Steven G. Louie, A. Zettl, and Paul L. McEuen. Crossed nanotube junctions. *Science*, 288(5465):494–497, 2000.

[196] H. Ko, K. Takei, R. Kapadia, S. Chuang, H. Fang, P.W. Leu, K. Ganapathi, E. Plis, H.S. Kim, S.Y. Chen, et al. Ultrathin compound semiconductor on insulator layers for high-performance nanoscale transistors. *Nature*, 468(7321):286–289, 2010.

[197] Nicholas A. Melosh, Akram Boukai, Frederic Diana, Brian Gerardot, Antonio Badolato, Pierre M. Petroff, and James R. Heath. Ultrahigh-density nanowire lattices and circuits. *Science*, 300(5616):112–115, 2003.

[198] Zhaohui Zhong, Deli Wang, Yi Cui, Marc W. Bockrath, and Charles M. Lieber. Nanowire crossbar arrays as address decoders for integrated nanosystems. *Science*, 302(5649):1377–1379, 2003.

[199] Sakulsuk Unarunotai, Justin C. Koepke, Cheng-Lin Tsai, Frank Du, Cesar E. Chialvo, Yuya Murata, Rick Haasch, Ivan Petrov, Nadya Mason, Moonsub Shim, Joseph Lyding, and John A. Rogers. Layer-by-layer transfer of multiple, large area sheets of graphene grown in multilayer stacks on a single sic wafer. *ACS Nano*, 4(10):5591–5598, 2010.

[200] Yoshikazu Homma, Yoshihiro Kobayashi, Toshio Ogino, and Takayuki Yamashita. Growth of suspended carbon nanotube networks on 100-nm-scale silicon pillars. *Applied Physics Letters*, 81(12):2261–2263, 2002.

[201] H. Yan, H.S. Choe, S.W. Nam, Y. Hu, S. Das, J.F. Klemic, J.C. Ellenbogen, and C.M. Lieber. Programmable nanowire circuits for nanoprocessors. *Nature*, 470(7333):240–244, 2011.

[202] Thushari Jayasekera and J W Mintmire. Transport in multiterminal graphene nanodevices. *Nanotechnology*, 18(42):424033, 2007.

[203] C. Ritter, M. Pacheco, P. Orellana, and A. Latge. Electron transport in quantum antidots made of four-terminal graphene ribbons. *Journal of Applied Physics*, 106(10):104303, 2009.

[204] Kamal K. Saha, Wenchang Lu, J. Bernholc, and Vincent Meunier. First-principles methodology for quantum transport in multiterminal junctions. *The Journal of Chemical Physics*, 131(16):164105, 2009.

[205] K. Kazymyrenko and X. Waintal. Knitting algorithm for calculating green functions in quantum systems. *Physical Review B*, 77(11):115119, Mar 2008.

[206] S. Ami and C. Joachim. Intramolecular circuits connected to n electrodes using a scattering matrix approach. *Physical Review B*, 65(15):155419, Apr 2002.

[207] Harold U. Baranger, David P. DiVincenzo, Rodolfo A. Jalabert, and A. Douglas Stone. Classical and quantum ballistic-transport anomalies in microjunctions. *Physical Review B*, 44(19):10637–10675, Nov 1991.

[208] Kamal K. Saha, Wenchang Lu, J. Bernholc, and Vincent Meunier. Electron transport in multiterminal molecular devices: A density functional theory study. *Physical Review B*, 81(12):125420, Mar 2010.

[209] M. Büttiker. Four-terminal phase-coherent conductance. *Physical Review Letters*, 57(14):1761–1764, Oct 1986.

[210] P. Brusheim, D. Csontos, U. Zülicke, and H. Q. Xu. Multiterminal multimode spin-dependent scattering matrix formalism: Electron and hole quantum spin transport in multiterminal junctions. *Physical Review B*, 78(8):085301, Aug 2008.

[211] Santanu K. Maiti. Multi-terminal quantum transport through a single benzene molecule: Evidence of a molecular transistor. *Solid State Communications*, 150(29-30):1269 – 1274, 2010.

[212] David M. Cardamone, Charles A. Stafford, and Sumit Mazumdar. Controlling quantum transport through a single molecule. *Nano Letters*, 6(11):2422–2426, 2006.

[213] K. Varga and S. T. Pantelides. Quantum transport in molecules and nanotube devices. *Physical Review Letters*, 98(7):076804, Feb 2007.

[214] Jing Kong, Erhan Yenilmez, Thomas W. Tombler, Woong Kim, Hongjie Dai, Robert B. Laughlin, Lei Liu, C. S. Jayanthi, and S. Y. Wu. Quantum interference and ballistic transmission in nanotube electron waveguides. *Physical Review Letters*, 87(10):106801, Aug 2001.

[215] David Mann, Ali Javey, Jing Kong, Qian Wang, and Hongjie Dai. Ballistic transport in metallic nanotubes with reliable pd ohmic contacts. *Nano Letters*, 3(11):1541–1544, 2003.

[216] Ali Javey, Jing Guo, Damon B. Farmer, Qian Wang, Dunwei Wang, Roy G. Gordon, Mark Lundstrom, and Hongjie Dai. Carbon nanotube field-effect transistors with integrated ohmic contacts and high- gate dielectrics. *Nano Letters*, 4(3):447–450, 2004.

[217] Sami Rosenblatt, Yuval Yaish, Jiwoong Park, Jeff Gore, Vera Sazonova, and Paul L. McEuen. High performance electrolyte gated carbon nanotube transistors. *Nano Letters*, 2(8):869–872, 2002.

[218] Keun Soo Kim, Yue Zhao, Houk Jang, Sang Yoon Lee, Jong Min Kim, Kwang S. Kim, Jong-Hyun Ahn, Philip Kim, Jae-Young Choi, and Byung Hee Hong. Large-scale pattern growth of graphene films for stretchable transparent electrodes. *Nature*, 457(7230):706–710, Feb 2009.

[219] Sukang Bae, Hyeongkeun Kim, Youngbin Lee, Xiangfan Xu, Jae-Sung Park, Yi Zheng, Jayakumar Balakrishnan, Tian Lei, Hye Ri Kim, Young Il Song, Young-Jin Kim, Kwang S. Kim, Barbaros Ozyilmaz, Jong-Hyun Ahn, Byung Hee Hong, and Sumio Iijima. Roll-to-roll production of 30-inch graphene films for transparent electro des. *Nat Nano*, 5(8):574–578, Aug 2010.

[220] Adrian Bachtold, Peter Hadley, Takeshi Nakanishi, and Cees Dekker. Logic circuits with carbon nanotube transistors. *Science*, 294(5545):1317–1320, 2001.

[221] Nathaniel M. Gabor, Zhaohui Zhong, Ken Bosnick, Jiwoong Park, and Paul L. McEuen. Extremely efficient multiple electron-hole pair generation in carbon nanotube photodiodes. *Science*, 325(5946):1367–1371, 2009.

[222] Xuan Wang, Linjie Zhi, and Klaus Mullen. Transparent, conductive graphene electrodes for dye-sensitized solar cells. *Nano Letters*, 8(1):323–327, 2008.

[223] Junbo Wu, Héctor A. Becerril, Zhenan Bao, Zunfeng Liu, Yongsheng Chen, and Peter Peumans. Organic solar cells with solution-processed graphene transparent electrodes. *Applied Physics Letters*, 92(26):263302, 2008.

[224] Goki Eda, Yun-Yue Lin, Steve Miller, Chun-Wei Chen, Wei-Fang Su, and Manish Chhowalla. Transparent and conducting electrodes for organic electronics from reduced graphene oxide. *Applied Physics Letters*, 92(23):233305, 2008.

[225] Vincent C. Tung, Li-Min Chen, Matthew J. Allen, Jonathan K. Wassei, Kurt Nelson, Richard B. Kaner, and Yang Yang. Low-temperature solution processing of graphenecarbon nanotube hybrid materials for high-performance transparent conductors. *Nano Letters*, 9(5):1949–1955, 2009.

[226] G. Giovannetti, P. A. Khomyakov, G. Brocks, V. M. Karpan, J. van den Brink, and P. J. Kelly. Doping graphene with metal contacts. *Physical Review Letters*, 101:026803, Jul 2008.

[227] Zhihong Chen, Joerg Appenzeller, Joachim Knoch, Yu-ming Lin, and Phaedon Avouris. The role of metalnanotube contact in the performance of carbon nanotube field-effect transistors. *Nano Letters*, 5(7):1497–1502, 2005.

[228] Wenjie Liang, Marc Bockrath, Dolores Bozovic, Jason H. Hafner, M. Tinkham, and Hongkun Park. Fabry - perot interference in a nanotube electron waveguide. *Nature*, 411(6838):665–669, Jun 2001.

[229] Zhiyong Zhang, Xuelei Liang, Sheng Wang, Kun Yao, Youfan Hu, Yuzhen Zhu, Qing Chen, Weiwei Zhou, Yan Li, Yagang Yao, Jin Zhang, and Lian-Mao Peng. Doping-free fabrication of carbon nanotube based ballistic cmos devices and circuits. *Nano Letters*, 7(12):3603–3607, 2007.

[230] S. Heinze, J. Tersoff, R. Martel, V. Derycke, J. Appenzeller, and Ph. Avouris. Carbon nanotubes as schottky barrier transistors. *Physical Review Letters*, 89(10):106801, Aug 2002.

[231] J. Appenzeller, J. Knoch, V. Derycke, R. Martel, S. Wind, and Ph. Avouris. Field-modulated carrier transport in carbon nanotube transistors. *Physical Review Letters*, 89(12):126801, Aug 2002.

[232] Ali Javey, Jing Guo, Qian Wang, Mark Lundstrom, and Hongjie Dai. Ballistic carbon nanotube field-effect transistors. *Nature*, 424(6949):654–657, Aug 2003.

[233] Bin Shan and Kyeongjae Cho. Ab initio study of schottky barriers at metal-nanotube contacts. *Physical Review B*, 70(23):233405, Dec 2004.

[234] Wenguang Zhu and Efthimios Kaxiras. Schottky barrier formation at a carbon nanotube—metal junction. *Applied Physics Letters*, 89(24):243107, 2006.

[235] Yu He, Jinyu Zhang, Shimin Hou, Yan Wang, and Zhiping Yu. Schottky barrier formation at metal electrodes and semiconducting carbon nanotubes. *Applied Physics Letters*, 94(9):093107, 2009.

[236] Yuki Matsuda, Wei-Qiao Deng, and William A. Goddard. Contact resistance for end-contacted metalgraphene and metalnanotube interfaces from quantum mechanics. *The Journal of Physical Chemistry C*, 114(41):17845–17850, 2010.

[237] Franois Lonard and Derek A Stewart. Properties of short channel ballistic carbon nanotube transistors with ohmic contacts. *Nanotechnology*, 17(18):4699, 2006.

[238] Tian Pei, Haitao Xu, Zhiyong Zhang, Zhenxing Wang, Yu Liu, Yan Li, Sheng Wang, and Lian-Mao Peng. Electronic transport in single-walled carbon nanotube/graphene junction. *Applied Physics Letters*, 99(11):113102, 2011.

[239] H. Hibino, H. Kageshima, M. Kotsugi, F. Maeda, F.-Z. Guo, and Y. Watanabe. Dependence of electronic properties of epitaxial few-layer graphene on the number of layers investigated by photoelectron emission microscopy. *Physical Review B*, 79:125437, Mar 2009.

[240] Yang Chai, A. Hazeghi, K. Takei, Hong-Yu Chen, P.C.H. Chan, A. Javey, and H.-S.P. Wong. Low-resistance electrical contact to carbon nanotubes with graphitic interfacial layer. *Electron Devices, IEEE Transactions on*, 59(1):12 –19, jan. 2012.

[241] S. Paulson, A. Helser, M. Buongiorno Nardelli, R. M. Taylor, M. Falvo, R. Superfine, and S. Washburn. Tunable resistance of a carbon nanotube-graphite interface. *Science*, 290(5497):1742–1744, 2000.

[242] RG Dandrea and CB Duke. Calculation of the schottky barrier height at the al/gaas (001) heterojunction: Effect of interfacial atomic relaxations. *Journal of Vacuum Science & Technology A: Vacuum, Surfaces, and Films*, 11(4):848–853, 1993.

[243] W. Tang, E. Sanville, and G. Henkelman. A grid-based bader analysis algorithm without lattice bias. *Journal of Physics: Condensed Matter*, 21:084204, 2009.

[244] W. S. Su, T. C. Leung, and C. T. Chan. Work function of single-walled and multiwalled carbon nanotubes: First-principles study. *Phys. Rev. B*, 76:235413, Dec 2007.

[245] Zhen Yao, Charles L. Kane, and Cees Dekker. High-field electrical transport in single-wall carbon nanotubes. *Physical Review Letters*, 84:2941–2944, Mar 2000.

[246] D. Pacile, J. C. Meyer, C. O. Girit, and A. Zettl. The two-dimensional phase of boron nitride: Few-atomic-layer sheets and suspended membranes. *Applied Physics Letters*, 92(13):133107, 2008.

[247] K. Watanabe, T. Taniguchi, and H. Kanda. Direct-bandgap properties and evidence for ultraviolet lasing of hexagonal boron nitride single crystal. *Nature materials*, 3(6):404–409, 2004.

[248] Gianluca Giovannetti, Petr A. Khomyakov, Geert Brocks, Paul J. Kelly, and Jeroen van den Brink. Substrate-induced band gap in graphene on hexagonal boron nitride: *Ab initio* density functional calculations. *Physical Review B*, 76:073103, Aug 2007.

[249] CR Dean, AF Young, I. Meric, C. Lee, L. Wang, S. Sorgenfrei, K. Watanabe, T. Taniguchi, P. Kim, KL Shepard, et al. Boron nitride substrates for high-quality graphene electronics. *Nature nanotechnology*, 5(10):722–726, 2010.

[250] Kin Fai Mak, Changgu Lee, James Hone, Jie Shan, and Tony F. Heinz. Atomically thin mos_2: A new direct-gap semiconductor. *Physical Review Letters*, 105:136805, Sep 2010.

[251] J. Brivio, D. Alexander, and A. Kis. Ripples and layers in ultrathin mos2 membranes. *Nano letters*, 2011.

[252] A. Castellanos-Gomez, M. Barkelid, S. Goossens, V.E. Calado, H.S.J. van der Zant, and G.A. Steele. Laser-thinning of mos2: on demand generation of a single-layer semiconductor. *Nano Letters*, 2012.

[253] Jonathan N. Coleman, Mustafa Lotya, Arlene ONeill, Shane D. Bergin, Paul J. King, Umar Khan, Karen Young, Alexandre Gaucher, Sukanta De, Ronan J. Smith, Igor V. Shvets, Sunil K. Arora, George Stanton, Hye-Young Kim, Kangho Lee, Gyu Tae Kim, Georg S. Duesberg, Toby Hallam, John J. Boland, Jing Jing Wang, John F. Donegan, Jaime C. Grunlan, Gregory Moriarty, Aleksey Shmeliov, Rebecca J. Nicholls, James M. Perkins, Eleanor M. Grieveson, Koenraad Theuwissen, David W. McComb, Peter D. Nellist, and Valeria Nicolosi. Two-dimensional nanosheets produced by liquid exfoliation of layered materials. *Science*, 331(6017):568–571, 2011.

[254] R.J. Smith, P.J. King, M. Lotya, C. Wirtz, U. Khan, S. De, A. O'Neill, G.S. Duesberg, J.C. Grunlan, G. Moriarty, et al. Large-scale exfoliation of inorganic layered compounds in aqueous surfactant solutions. *Advanced Materials*, 2011.

[255] B. Radisavljevic, A. Radenovic, J. Brivio, V. Giacometti, and A. Kis. Single-layer mos2 transistors. *Nature nanotechnology*, 6(3):147–150, 2011.

[256] K.I. Bolotin, KJ Sikes, Z. Jiang, M. Klima, G. Fudenberg, J. Hone, P. Kim, and HL Stormer. Ultrahigh electron mobility in suspended graphene. *Solid State Communications*, 146(9):351–355, 2008.

[257] Igor Popov, Gotthard Seifert, and David Tománek. Designing electrical contacts to mos_2 monolayers: A computational study. *Phys. Rev. Lett.*, 108:156802, Apr 2012.

[258] Y. Ma, Y. Dai, M. Guo, C. Niu, and B. Huang. Graphene adhesion on mos2 monolayer: An ab initio study. *Nanoscale*, 3(9):3883–3887, 2011.

[259] Y. Li, H. Wang, L. Xie, Y. Liang, G. Hong, and H. Dai. Mos2 nanoparticles grown on graphene: an advanced catalyst for the hydrogen evolution reaction. *Journal of the American Chemical Society*, 2011.

[260] K. Chang and W. Chen. In situ synthesis of mos2/graphene nanosheet composites with extraordinarily high electrochemical performance for lithium ion batteries. *Chemical Communications*, 2011.

[261] J Enkovaara, C Rostgaard, J J Mortensen, J Chen, M Duak, L Ferrighi, J Gavnholt, C Glinsvad, V Haikola, H A Hansen, H H Kristoffersen, M Kuisma, A H Larsen, L Lehtovaara, M Ljungberg, O Lopez-Acevedo, P G Moses, J Ojanen, T Olsen, V Petzold, N A Romero, J Stausholm-Mller, M Strange, G A Tritsaris, M Vanin, M Walter, B Hammer, H Hkkinen, G K H Madsen, R M Nieminen, J K Nrskov, M Puska, T T Rantala, J Schitz, K S Thygesen, and K W Jacobsen. Electronic structure calculations with gpaw: a real-space implementation of the projector augmented-wave method. *Journal of Physics: Condensed Matter*, 22(25):253202, 2010.

[262] J. J. Mortensen, L. B. Hansen, and K. W. Jacobsen. Real-space grid implementation of the projector augmented wave method. *Phys. Rev. B*, 71:035109, Jan 2005.

[263] M. Dion, H. Rydberg, E. Schröder, D. C. Langreth, and B. I. Lundqvist. Van der waals density functional for general geometries. *Phys. Rev. Lett.*, 92:246401, Jun 2004.

[264] Kyuho Lee, Éamonn D. Murray, Lingzhu Kong, Bengt I. Lundqvist, and David C. Langreth. Higher-accuracy van der waals density functional. *Phys. Rev. B*, 82:081101, Aug 2010.

[265] Zongyou Yin, Hai Li, Hong Li, Lin Jiang, Yumeng Shi, Yinghui Sun, Gang Lu, Qing Zhang, Xiaodong Chen, and Hua Zhang. Single-layer mos2 phototransistors. *ACS Nano*, 6(1):74–80, 2012.

[266] J.T. A Rycerz et al. Valley filter and valley valve in graphene. *Nature Physics*, 3(3):172–175, 2007.

[267] Di Xiao, Wang Yao, and Qian Niu. Valley-contrasting physics in graphene: Magnetic moment and topological transport. *Physical Review Letters*, 99:236809, Dec 2007.

[268] Y. P. Shkolnikov, E. P. De Poortere, E. Tutuc, and M. Shayegan. Valley splitting of alas two-dimensional electrons in a perpendicular magnetic field. *Physical Review Letters*, 89:226805, Nov 2002.

[269] Hauling Zeng, Junfeng Dai, Wang Yao, Di Xiao, and Xiaodong Cui. Valley polarization in mos2 monolayers by optical pumping. *Nature Nanotechnology*, 2012.

[270] K.F. Mak, K. He, J. Shan, and T.F. Heinz. Control of valley polarization in monolayer mos2 by optical helicity. *Nature Nanotechnology*, 2012.